DOI:10.15774/PPKE.ITK.2012.003

Low Resolution Infrared Proximity Array Based 3D Object and Force Reconstruction, and Modular Oscillatory Arrays

Ákos Tar

Faculty of Information Technology

Pázmány Péter Catholic University

Scientific adviser:
György Cserey, Ph.D.

A thesis submitted for the degree of

Doctor of Philosophy (Ph.D)

2011

DOI:10.15774/PPKE.ITK.2012.003

DOI:10.15774/PPKE.ITK.2012.003

I would like to dedicate this thesis to my loving family ...

DOI:10.15774/PPKE.ITK.2012.003

DOI:10.15774/PPKE.ITK.2012.003

Acknowledgements

First of all, I would like to thank my supervisor György Cserey for introducing me to scientific work and for his constant support in bringing our ideas into reality and believing in my research activity.

I am thankful for the Pázmány Péter Catholic University Faculty of Information Technology and the Multidisciplinary Doctoral School for providing tools and a caring environment for my work, especially personally for Judit Nyékyné-Gaizler, Tamás Roska and Péter Szolgay.

I would like to thank to my closest colleague József Veres for the long-lasting joint work during these years. The cooperation of my colleagues at the Robotics Laboratory Norbert Sárkány, Miklós Koller, Ádám Rák, Norbert Hóz, Balázs Jákli, Gergely Soós, Gergely Feldhoffer, Alpár Sándor, Ferenc Lombai and Gandhi Gaurav is greatly acknowledged. The work with them greatly contributed to my scientific results.

I would like to thank also my fellow PhD students and friends for their help, especially to Dávid Tisza, Péter Vizi, János Rudan, Zoltán Tuza, Dániel Szolgay, András Kiss, Gábor Tornai, László Füredi, Zoltán Kárász, Andrea Kovács, Vilmos Szabó, Kálmán Tornai, Balázs Varga, Tamás Pilissy, Róbert Tibold, Ádám Balogh and Endre László.

Thanks especially for the discussions and ideas to Gábor Szederkényi, András Oláh, Attila Kis, Gábor Vásárhelyi, Kristóf Iván, Éva Bankó, Béla Weiss, Kristóf Karacs and Attila Tihanyi.

Special credits are also for the endless patience and helpfulness to Mrs Vida, Lívia Adorján, Mrs Haraszti, Mrs Körmendy, Mrs Tihanyi and Mrs Mikesy and the rest of administrative and financial personnel.

Special thanks go to Sarolta Tar, Miklós Gyöngy and Zsófia Cserey who helped a lot in the English revision of the text.

DOI:10.15774/PPKE.ITK.2012.003

The Operational Program for Economic Competitiveness (GVOP KMA), The office of Naval Research (ONR) and the Hiteles Ember Foundation for their support are greatfully acknowledged.

For the outstanding support of bringing the CAD models into reality with 3D printing technology I would like to thank to VARINEX Informatikai Zrt.

The loving support of all my *family* and my wife *Bernadett* helped me through the hardest moments of this period.

DOI:10.15774/PPKE.ITK.2012.003

List of Figures

2.1 A photograph of the sensor array 8
2.2 Schematic diagram of the infrared LED control 9
2.3 Schematic diagram of the photodiode readout circuit 10
2.4 The two experimental setup groups where the sensor array was tested 12
2.5 Distance measurement method, theory of operation 15
2.6 Difference between the real θ and estimated θ' values at different number of iterations 16
2.7 Measurement and simulation result of the sensor array of an object placed 20 cm above, with and without angle of incidence correction 19
2.8 Scanning result of different kind of objects (cube, U-shape and H-shape) 20
2.9 Test case where the previous version of the sensor array was attached on a bipedal robot feet in order to detect obstacles 22
2.10 Scan result of different landmarks. On the top are the pictures of the used landmarks and on the bottom the images created with the sensor array attached on a mobile robot. 23
2.11 Experimental result of a door-step detailed detection with a PowerBot type mobile robot, where the sensor was mounted on the front bumper of the robot and was directed to the ground. 25
2.12 Localization experiment with the PowerBot type mobile robot . . . 26

3.1 Schematic drawing of the tactile sensor 33
3.2 The data acquisition board and a connected tactile sensor prototype. 34
3.3 Shematic drawing of the reflected lighs 35
3.4 Deformation of the semicircle 37
3.5 Experimental setup to measure the tactile sensor pressure profile along an axis 39
3.6 Setups for measuring noise, impact and stroke 40

DOI:10.15774/PPKE.ITK.2012.003

LIST OF FIGURES

3.7 Static load response of the tactile sensor . . . 42
3.8 Maximal load measurement . . . 43
3.9 Sensor output characteristic . . . 44
3.10 Error between the real and calculated force incidence angle . . . 45
3.11 Calibrated tactile sensor output . . . 46
3.12 Force measurement form different directions . . . 46
3.13 Noise, hammer impact, and brush stroke measurement . . . 47
3.14 Pulse shape measurement . . . 48
3.15 Measurement of the realaxation characteristic at different load levels. 49
3.16 Relaxation characterictic after the load was removed. At 0.25 s all signal value dropped at least 86% and after a certain time returned to zero. . . . 49
3.17 The three layered sensor structure. . . . 50
3.18 The moulding process of the elastic cover . . . 53

4.1 Current vs. voltage characteristics of the Chua's diode . . . 57
4.2 Chua's Circuit Schematic . . . 58
4.3 Snapshot of the Chua kit . . . 60
4.4 Snapshot of the second version of the Chua kit . . . 61
4.5 Chua kit with the extension borad . . . 62
4.6 General architecture of programmable logic layer . . . 63
4.7 Coupling grid . . . 64
4.8 The topologies and the weights, which were used in the experiments 65
4.9 Two connected Chua's circuit at 0 Ω and at 10 K Ω . . . 66
4.10 The Chua's circuits moves from de-synchronization to synchronization 66
4.11 SPICE simulation of two connected Chua's circuits at 10 $K\Omega$ . . . 67
4.12 SPICE simulation of two connected Chua's circuits at 1 $K\Omega$ . . . 67
4.13 SPICE simulation of two connected Chua's circuits at 6.5 $K\Omega$ . . . 68
4.14 Simulation of the phase transition . . . 68
4.15 Ten Chua's Circuits were connected in 3D in a cross like topology . 70
4.16 Connecting $3x3$ Chua's circuits . . . 71
4.17 A picture of the experimental setup where eight Chua's circuits were connected . . . 72

DOI:10.15774/PPKE.ITK.2012.003

DOI:10.15774/PPKE.ITK.2012.003

Summary of abbreviations

Abbreviation	Concept
$SLAM$	Simultaneous Localization And Mapping
PSD	Position Sensing Device
US	Ultrasound Sensor
ToF	Time of Flight
LED	Light Emitting Diode
DAC	Digital to Analog Converter
ADC	Analog to Digital Converter
SPI	Serial Peripheral Interface
PC	Personal Computer
$LIPA$	Large Infrared Proximity Array
$MEMS$	Microelectromechanical Systems
FSR	Force Sensing Resistor
DOF	Degree Of Freedom
PCB	Printed Circuit Board
LUT	Look Up Table
MSB	Most Significant Bit
LSB	Least Significant Bit
CAD	Computer Aided Design
EEG	Electroencephalography
CNN	Cellular Neural Network
MUX	Multiplexer
$SPICE$	Simulation Program with Integrated Circuit Emphasis

DOI:10.15774/PPKE.ITK.2012.003

Contents

Acknowledgement i

List of Figures v

Summary of abbreviations viii

Contents ix

1 Introduction 1

1.1 Research Goals . . . 3

2 Infrared Sensor Array 5

2.1 Introduction . . . 5

2.2 General description of the sensor array . . . 8

2.3 Experimental setup . . . 11

2.3.1 Object scanning experiment . . . 11

2.3.2 Mobile robot experiment . . . 13

2.4 Signal post processing . . . 14

2.4.1 Sensor model . . . 14

2.4.2 Edge reconstruction and object outline detection . . . 16

2.5 Experimental results . . . 18

2.5.1 Measuring the angle of incidence . . . 18

2.5.2 Object scanning experiments . . . 18

2.5.2.1 Edge reconstruction and object outline detection . . . 18

2.5.2.2 Surface trace . . . 20

2.5.2.3 Image registration . . . 21

2.5.3 Mobile robot experiments . . . 22

2.5.3.1 Landmark detection . . . 22

2.5.3.2 Door-step detection . . . 24

DOI:10.15774/PPKE.ITK.2012.003

2.5.3.3 Map building (SLAM) 24
2.6 Conclusion 27

3 Complaint 3D Tactile Sensor 29
3.1 Introduction 29
3.2 Design concepts 31
3.3 Sensor description 32
3.3.1 Theory of operation 35
3.4 Experimental setup 38
3.4.1 Static calibration of the sensor 38
3.4.2 Characterization of the sensor 38
3.4.3 Sensor capabilities 40
3.5 Signal post processing 41
3.6 Experimental results 42
3.6.1 Static calibration of the sensor 42
3.6.2 Characterization of the sensor 43
3.6.3 Measuring the force incidence angle 43
3.6.4 Calibrated sensor output 44
3.7 Sensor capabilities 45
3.7.1 Force directions 45
3.7.2 Noise performance 45
3.7.3 Hammer impact 46
3.7.4 Brush stroke 47
3.7.5 Pulse measurement 47
3.7.6 Relaxation time 48
3.8 Layered structure of the elastic cover 50
3.9 Sensor prototyping 52
3.10 Conclusion 54

4 Studying Synchronization Phenomenon in Oscillatory and Chaotic Networks 55
4.1 Introduction 55
4.2 Chua's circuit 56
4.3 Chua's circuit kit 59
4.4 Chua's circuit grid - general architecture 59
4.5 Architecture implementation 61

DOI:10.15774/PPKE.ITK.2012.003

4.5.1 Interconnecting interface 61
4.5.2 Programmable logic 62
4.5.3 Coupling grid 63
4.6 Experimental results 63
4.6.1 Case 1. one dimensional coupled Chua's circuits 65
4.6.2 Case 2. two dimensional coupled Chua's circuits 68
4.6.3 Case 3. three dimensional coupled Chua's circuits 69
4.7 Discussion 73
4.8 Conclusion 74

5 Summary **75**
5.1 Main findings and results 75
5.2 New scientific results 75
5.3 Application of the results 76

Bibliography **81**

DOI:10.15774/PPKE.ITK.2012.003

CONTENTS

DOI:10.15774/PPKE.ITK.2012.003

Chapter 1

Introduction

Emergence is a prevalent phenomenon in nature, when the cooperation in a simple ruled system results the arise of a new feature or a new behavior (e.g.: cells form organs). It is also interesting from an engineer point of view, where the interaction of each element in a system could improve the overall performance (e.g: interpolation) or new features can arise (e.g: robot cooperation). Therefore during my research I aimed to use topologies where the interaction of the cells enhanced the overall system performance.

The two main research fields:

- **Novel sensor technology to improve the environment recognition in robotics**
- **Synchronization in coupled oscillatory networks**

The presence of robotics made the first breakthrough in the industry. Their accuracy, workload capacity, reliability, have allowed high-quality and low cost mass production. Since then, of course, big variety of size, shape and structure robots has been developed. Due to the technological developments and research robots are getting very common. There are plenty of solutions, which have been trying to ease our ordinary life. Their appearance is tending to be more human like as in a man-made word, a humanoid robot can adopt to the human made tools and devices much more easily. For a humanoid robot, it is essential to walk. This is a very interesting and intensively researched field, but we are still far from the robust and stable walking. Although much progress has been made, there are already statically stable walking robots [8, 9, 10] and there are some good examples of dynamic walking [11, 12, 13].

DOI:10.15774/PPKE.ITK.2012.003

1. INTRODUCTION

Despite all this for the widespread use of robots we still have to wait. In a well modeled environment even without sensorial feedback, they can already execute a number of tasks [14], but they cannot adopt to a dynamic environment. The problem is that robots must sense their environment, they must be connected with the surroundings.

Humans during walking preidentify the obstacles ahead, their size, position, orientation with the aid of vision (contactless sensing), and we can immediately modify our walking in order to avoid the obstacles with the lowest energy. Researchers tried to use vision systems to do the same with humanoid robots [15, 16, 17] and also equip with basic reflexes using contact based sensing [18]. However due to the high computation power (object classification, image registration, 3D vision) it is hard to make real time control. Furthermore, today robots cannot divide their visual attention between navigation or detecting interactions from the environment, thus usually separate camera systems are used to each task [8].

This is why it is essential to use such a sensor (sensor systems) that produces reliable and substantial information at low computation power. An other solution cold be to use many sensors as a distributed system. Use separate sensor or sensors (even in a reflex level) for example for obstacle detection that can provoke the visual attention for identification and to make the necessary avoidance manoeuvres. During our MSc studies with my collage József Veres we build a bipedal robot [3]. Our experimental results also demonstrated that in order to achieve stable and robust walking it is crucial to connect the sensed environment into the control (e.g: how the robot is standing respect to the ground).

Hence during my research I tried to create hardware implemented contact base and contactless sensors (than can be used in any field of robotics) wherewith the perception of the environment can be improved at low computation power.

The other interesting research field is the coupled oscillatory arrays whose synchronization is a prevalent phenomenon in nature [19]. Within this the chaotic systems are already well-known for strange patterns in their phase space, which has always attracted the research community [20, 21]. Even more stranger patterns can be observed in case of two or more chaotic system connected in different topologies [22]. Researchers already showed chaotic behavior in the brain using EEG [23, 24]. Experimental results demonstrated formation of chaotic oscillation in some part of the brain before an epileptic shock, where the propagation of the spiking can be blocked with in-depth brain stimulation [25]. The same phenomena

DOI:10.15774/PPKE.ITK.2012.003

was also detected in case of arrhythmia [26]. To understand this kind of patterns and phenomenons it is essential in order to create new cure or medical treatments. However, until now most of the studies are based on only software simulations.

Therefor during my research I investigated an implementation where oscillators (even chaotic oscillators) can be connected with variable weights and topology.

With this tool, the software simulations could be validated or with using different topology and coupling weights new phenomenons may be observed or even the real time behavior of simple (chaotic) oscillatory systems could be modeled.

1.1 Research Goals

The aim of my research was to create sensors (sensor arrays) to improve the today robots' capabilities to sense the environment. It was divided into two parts contactless and a contact based sensing. Contactless sensing is used to detect obstacles, distances, outlines, occupied areas during the robot motion remotely. Contact based information is more connected with the sensed object physical properties where the stiffness, weight (forces), or even force distribution for balancing must be detected.

Another goal was to create such a hardware implemented flexible architecture, where interconnected oscillators behavior can be examined in real time in case of different topology using several types of interconnection elements.

DOI:10.15774/PPKE.ITK.2012.003

1. INTRODUCTION

DOI:10.15774/PPKE.ITK.2012.003

Chapter 2

Infrared Sensor Array

2.1 Introduction

An essential function of mobile robots is to navigate safely around their environment. This function is necessary regardless of their main objective, be it pure obstacle avoidance, object picking and placing, or in a more complex case, simultaneous localization and mapping (SLAM). Since mobile robots are often placed in unknown environments, the use of sensor-based data to achieve object detection, classification and localization is often a challenging problem. The more quickly and precisely the robot can obtain sensorial information about its vicinity, the faster and more reliably it can react. Assuming that contact with unwanted objects should be minimized, all of the above tasks rely on distance measurement sensors.

Robots often need to know how far an object is, what it looks like and what its orientation is. Camera systems are already used for creating 3D images of the environment [27, 28], but mobile robots seldom use the data provided by cameras for low level obstacle avoidance due to high computation power requirements. More often, 2D laser scanners are used with a tilt mechanism to create the 3D scan of the environment [29]. Despite their accuracy, their size and price present a serious drawback. Traditional distance measurement sensors such as ultrasonic and infrared Position Sensing Devices could also be used for creating 3D images of an object [30],[31].

Ultrasonic (US) and offset-based infrared Position Sensing Devices (PSD) are widely used in order to determine the distance of an object. US sensors measure the time of flight (ToF) of the ultrasound signal emitted and reflected to the receiver. A typical single data acquisition time for an object placed 50 cm away from the

DOI:10.15774/PPKE.ITK.2012.003

sensor is 3 ms. The main disadvantage of this kind of sensor is the poor angular resolution. The detected object could be anywhere along the perimeter of the US beam due to the wide (typically 35°) angular sensitivity of the receiver. Because of their relatively large size (of the order of $d = 15$ mm), dense arrays cannot be constructed.

Offset-based infrared technology uses much narrower beams, both in the case of measuring amplitude response and the offset of the reflected light. The most common offset-type infrared sensors are the *Sharp GP* series. They are very compact (with a surface area of 44 mm × 13 mm), and have a low cost (∼10 US dollars). These analog sensors are available in various measurement ranges, the shortest sensing distance being 4 cm (Model *GP2D120*, range 4 – 30 cm), and the maximum being 5.5 m (Model *GP2Y0A700K*, range 1 – 5.5 m). In some applications, even these compact dimensions and measurement ranges are not adequate. To further complicate matters, the sensor has a maximum readout speed of 26 Hz (38 ms) and the output signal varies nonlinearly with distance. Researchers already proved it to be useful for object detection [32] and for creating surface-traces of various objects [30], and for localization purposes [33, 34], but because of the sensor speed, real time operation cannot be achieved in many applications.

In this chapter a new reflective type infrared LED and photodiode based distance measurement array is demonstrated as well as its potential usage for tracing object outlines, surfaces and SLAM. The advantage of using a sensor array in the detection of the angle of the reflected light and in increasing the pixel resolution will also be demonstrated.

Although using the amount of reflected infrared light to measure distance is a well-established method, its current applications are mainly restricted to object avoidance, object detection and docking guidance [35]. In these applications, only one LED-photodiode pair is used. The reconstruction of object outlines or surfaces with many LED-photodiode pairs has not been studied yet. The main reasons for this lack of research are the limitations of such detectors, namely the nonlinear output characteristic and the high dependence of the received light on the reflective properties of the object.

Despite the above limitations, the inherent high spatiotemporal resolution and compact dimensions of infrared LED-photodiode pairs make them an important competitor to other distance measurement methods. In contrast to other previously mentioned methods such as ultrasound, the readout speed can be of the order of MHz, and the analogue nature of the signal guarantees a high spatial resolution,

DOI:10.15774/PPKE.ITK.2012.003

with the readout circuitry and analog-to-digital conversion being the main limiting factors. Indeed, it has been shown that LED-photodiode pairs are a viable way to measure distances in the submicron [36] as well as decimeter [37] range.

There are some outstanding articles that utilize infrared sensors for distance estimation ([36, 38, 39, 40]) and for localization purposes ([41, 42, 43]). The key is if a prior assumptions about the given object distance (based on a US, PSD sensor) or reflective properties of the object is given then the reflective type infrared sensors can be used responsibly, or another good method is to try to find the maximum energy of the reflective light [44]. However, with such knowledge distance cannot be measured accurately since the sensor gives the same result if the sensed object is close or it is white. It should also be noted that in the articles mentioned previously, typically only a few infrared sensors are used on the robots (1 or 2 on each side), each sensor is independent, and the infrared LED control is an on-off type. In [45] infrared sensors are used for creating analogue bumpers for a mobile robot and for detecting whether an object is within range or not. As a precursor to the method applied here, two infrared transceivers were used in [46] to detect object orientation. Here, a more accurate iterative method will be shown to calculate the object orientation. Pavlov et al. [47] showed how cylindrical object location, trajectory and velocity of motion can be determined with 3 pairs of highly directional infrared LED and photodiodes.

Building on our previous work Á. Tar et al. [4], a better sensor model and an iterative method is given to calculate the angle of incidence, thus achieving a more precise distance measurements with improved electronics.

DOI:10.15774/PPKE.ITK.2012.003

2.2 General description of the sensor array

Reflective type infrared sensors that have a coupled optical pair mounted in a reflective configuration are readily available (e.g. Model TCRT1000, Vishay Ltd, US). These compact sensors only have one separator (between the infrared LED and receiver) which could cause crosstalk in the array. In order to maintain maximal flexibility in the design and in order to be able to equally space the emitters and the detectors in the array, the current work uses individual infrared LEDs and photodiodes.

The infrared sensor array considered in this work consists of 8 infrared LEDs and 8 photodiodes equally spaced in a 120 mm wide row, giving an 8 mm separation distance (see Fig. 2.1). The infrared LEDs (Model TSHF5210, Vishay Ltd, US, 5 mm wide) was chosen to be highly directional with a narrow $\pm 10^\circ$ angle of half intensity. Its peak wavelength is 890 nm, with a typical operating current of 100 mA producing a radiant intensity of 180 mW/sr. By using only short 100 μs pulses, a current of 1 A may be used, which provides an intensity of 1800 mW/sr.

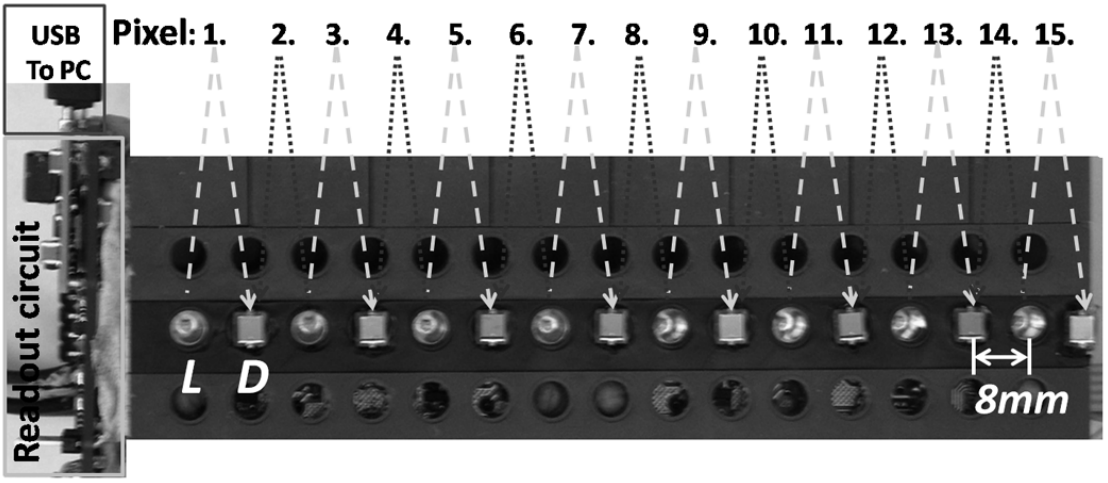

Figure 2.1: A photograph of the sensor array. The infrared LEDs (L) and photodiodes (D) are mounted on a regular grid of 8 mm cells. The middle black part acts as a separator between the infrared LEDs and photodiodes. On the top, the number of the measured pixels (measured distance) are indicated and the way they are measured is shown. Data is gathered from photodiodes on either side of each LED, so the first pixel is measured with the first photodiode while the first infrared LED is on, the second pixel is measured with the first photodiode but using the second infrared LED illumination and so on. The array layout and this measurement method will also help to determine the angle of incidence.

Each infrared LED in the row is switched independently with a PMOS tran-

DOI:10.15774/PPKE.ITK.2012.003

sistor and only one LED state is on at a time. A dynamic current control is also implemented, using another PMOS transistor the gate of which is driven by a 16-bit resolution Digital Analog Converter (DAC). As the DAC output voltage is decreased the transistor drain-source resistance (R_{ds}) also decreases. Hence, the current that flows through the LED can be controlled precisely. The schematic diagram of the LED control is shown in Fig. 2.2.

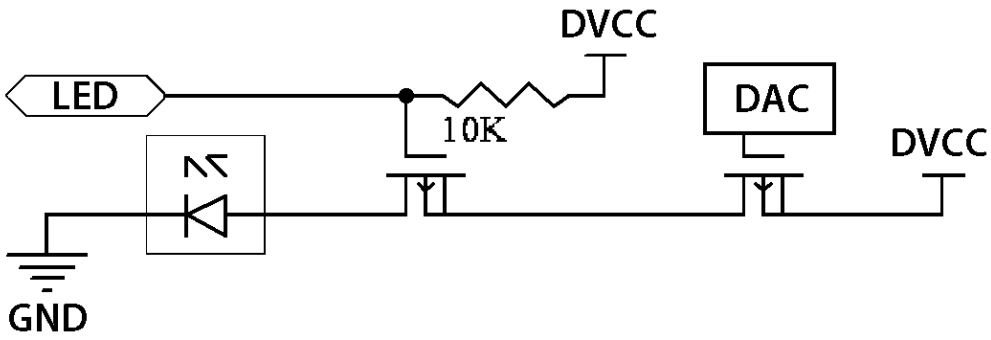

Figure 2.2: Schematic diagram of the infrared LED control. The infrared LED is switched ON if 0 voltage is applied on the PMOS transistor gate labeled with LED. The second transistor limits the maximal forward current. Its resistance (R_{ds}) is proportional to the voltage applied on its gate with a 16-bit resolution Digital Analog Converter (DAC).

The light received by the photodiode generates a photo-electric current that is converted and amplified with a rail-to-rail amplifier. The output changes from 0 V (no reflection) to 5 V (saturation). In our experimental setup, this creates an effective distance measurement range of 30 cm at 250 mA. The circuit schematic is shown in Fig. 2.3. The anode of the photodiode (Model BPW34, Vishay Ltd, US, 5.4 mm long, 4.3 mm wide) is connected to -5 V. This improves the sensor's transient behavior. Although the photodiode packaging is different from the infrared LED, this is because the photodiodes in the 5 mm diameter packaging have a much smaller radiant sensitive area. This version has a 2.65 $\times$ 2.65 mm radiant sensitive area with a 0.65 A/W spectral sensitivity at 850 nm.

Each sensor output is directly connected to a 24-bit resolution ADC (Model ADS1258, Texas Instruments, US). The ADC has a built-in 16 channel analog multiplexer and an 8-bit general purpose I/O register. The ADC sampling rate with auto scan (through the 16 channels) is 23.7 kSPS per channel. This module is configured via Serial Peripheral Interface (SPI) and its general purpose I/O port is also accessed in this way. The 8-bit general purpose I/O port is used to

DOI:10.15774/PPKE.ITK.2012.003

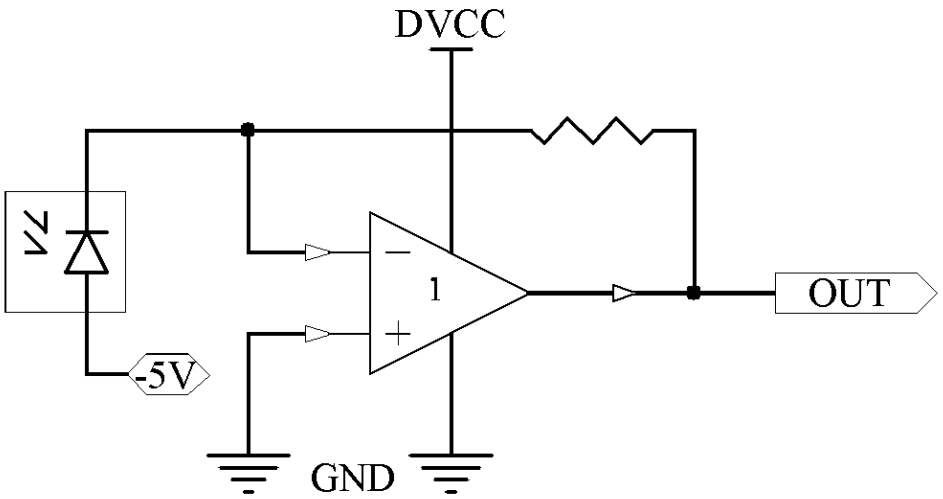

Figure 2.3: Schematic diagram of the photodiode readout circuit. The photoelectric current generated by the reflected amount of light is converted to voltage and amplified with a precise amplifier.

control the infrared LED on/off state in the row. The DAC shares the same SPI port with the ADC that is driven by a microcontroller running on 64 MHz (Model dsPIC30F4013, Microchip, US). It is also responsible for the communication to the PC via a USB port. In the test environment a PC was used to process the sensor data as the aim was to demonstrate the capabilities of the sensor array in general and not limited by the computation power. Nevertheless, efforts had been made to use those methods that can also be implemented on a microcontroller. It should also be noted that the ADC and DAC devices have higher accuracies than were needed in the experiments, so the infrared LED current was quantized to 10 mA steps and only 16-bit sampling was used at the sensor readout.

DOI:10.15774/PPKE.ITK.2012.003

2.3 Experimental setup

The capabilities of the infrared sensor array were tested in two different setups. In the first setup the movement of the production line or mobile robot (including sensor guided wheelchairs) was simulated, where the motion in x, y, z direction could be measured based on sensorial data (e.g odometry) and straight line movements were expected. In the second setup a PowerBot type mobile robot [48] was used.

2.3.1 Object scanning experiment

In this setup (Fig. 2.4/I.) a wooden cube, U-shape and a LEGO H-shape was measured (Fig. 2.4/a,b,c). These objects were chosen as their dimensions are comparable with the sensor array resolution. The sensor array was placed on the z axis of an x, y, z table that was capable of moving with 10 μm precision. The sensor array was moved only in the y direction and no movement was made in the x and z axes. Since an 8×8 sensor array was tried to be modeled, the incrementation step in the y direction was set to 8 mm. The angle of incidence was only approximated in the x direction based on the measured pixels values in the array. In the scanning procedure 3 different resolutions could be distinguished. The resolution in:

- x - the distance between the infrared LEDs and photodiodes in the array (pixel resolution)
- y - the incrementation step that the table was moved (array resolution)
- z - the used measurement range and the used data converter (in depth-resolution)

The scanning process was as follows:

1. The x, y, z table was moved to the starting position
2. Measurements were taken with the sensor array, which included offset and ambient light cancellation
3. The table was moved 8 mm in the y direction
4. The measured data was sent to the PC
5. The binary output of the sensors was converted to distance on the PC

DOI:10.15774/PPKE.ITK.2012.003

2. INFRARED SENSOR ARRAY

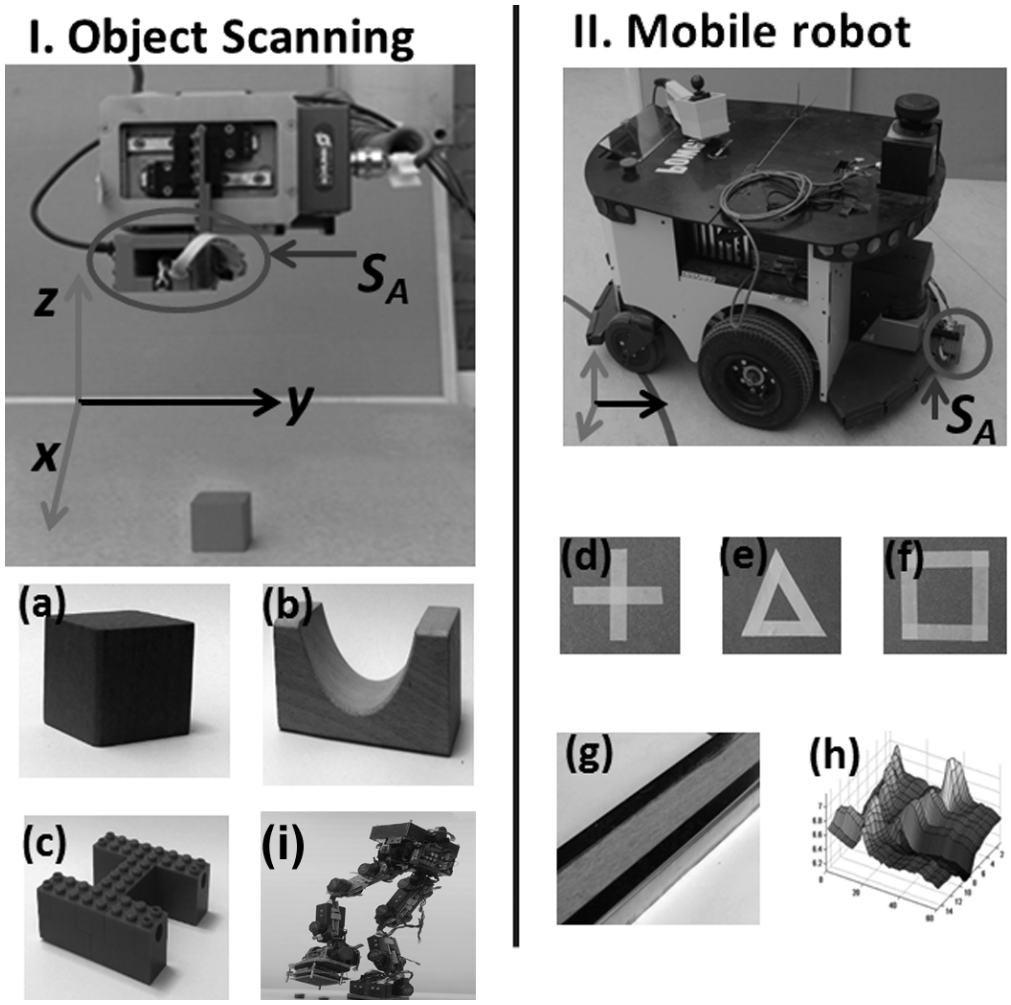

Figure 2.4: Two experimental setup was made. In the first the sensor array was attached on the z axis of an x, y, z table that was capable of moving with a10 μm precision. The sensor array (S_A) was moved only in the y direction, and each scanned object (a,b,c) was placed on the xy plane. Simulating a bipedal robot motion (i) an obstacle detection experiment was made with the previous version of the sensor array [4]. In the second setup the sensor array was attached onto the rear bumper of a PowerBot type mobile robot. The robot was driven with a constant speed of 0.2 m/s on a smooth flat surface. The sensor array was at a distance of 65 mm from the ground and looking down to the floor. The sensor array was tested for detecting on-road landmarks for localization purposes (d,e,f), door-step detection (g) and also a potential usage as supplementary sensor for SLAM was tested (h).

DOI:10.15774/PPKE.ITK.2012.003

An additional experiment (Fig. 2.4/i) with the previous version of the sensor array [4] was made. A case were the LIPA (Large Infrared Proximity Array)was mounted on a bipedal robot feet was tried to be modeled. During the robot motion the feet position of the swing phase leg can be calculated thus the appropriate sensor output at each position can be registered and a higher resolution image can be generated. To validate this theory this sensor array was also mounted on the plotter table in the same configuration but it was also moved in the x direction.

2.3.2 Mobile robot experiment

The sensor array was attached onto the rear bumper of a PowerBot type mobile robot. The robot was driven with a constant speed of 0.2 m/s on a flat surface. The sensor array was at a distance of 65 mm from the ground and looking down to the floor (Fig. 2.4/II.). As the robot was moving, several measurements were taken with the sensor array: the sensor array was tested for on-road landmark detection for localization purposes (Fig. 2.4/d,e,f), door-step detection (Fig. 2.4/g) and also a potential usage as a supplementary sensor for SLAM (Fig. 2.4/h).

DOI:10.15774/PPKE.ITK.2012.003

2.4 Signal post processing

2.4.1 Sensor model

A general description of the sensor model will now be given, including a method to obtain the angle of incidence. As has been mentioned, the current work uses a linear array of 8 LED and photodiode pairs. The central idea of this section is that by combining emitters and receivers across pairs, a resolution greater than the spacing between LED and photodiode pairs can be achieved. The method of building up an image pixel by pixel is now described. Data is gathered from photodiodes on either side of each LED. The value of the first image pixel is generated by measuring with the first photodiode during the first infrared LED emitting, the second pixel is obtained with the first photodiode and the second infrared LED and so on. This method results in 15 pixels in the array as can be seen in Fig. 2.1. The array layout and the described pixel measurement method will also help to determine the angle of incidence. A pioneering work by G. Benet *et al.* [36] introduced the concept of using the inverse square law to determine the distance of an object instead of the Phong illumination model. In keeping with this law, Eq. (2.1) describes the dependence of the sensor output $y(x, \theta)$, on x and θ, where x is the distance of the object and θ is the angle of incidence.

$$y(x, \theta) = \frac{\alpha_i \cdot \alpha_0 \cdot cos\theta}{x^2} + \beta \tag{2.1}$$

where α_i is the reflective properties of the sensed object at the viewing area, α_0 is constant (accounting for the radiant intensity of the used infrared LED, spectral sensitivity of the photodiode, and the amplification), and β accounts for the level of ambient light and the offset voltage of the amplifier. Because the photodiodes do not have daylight filter attached, a measurement is taken without infrared emission to obtain β due to ambient light and the offset voltage of the amplifier.

The α_i parameter is usually obtained by using other distance calibration with another distance measurement method such as US [49] (a distance measurement is made with US and using Eq. 2.1 α_i can be calculated).

An iterative solution to estimating the angle θ is presented. From Fig. 2.5, it can be seen that

DOI:10.15774/PPKE.ITK.2012.003

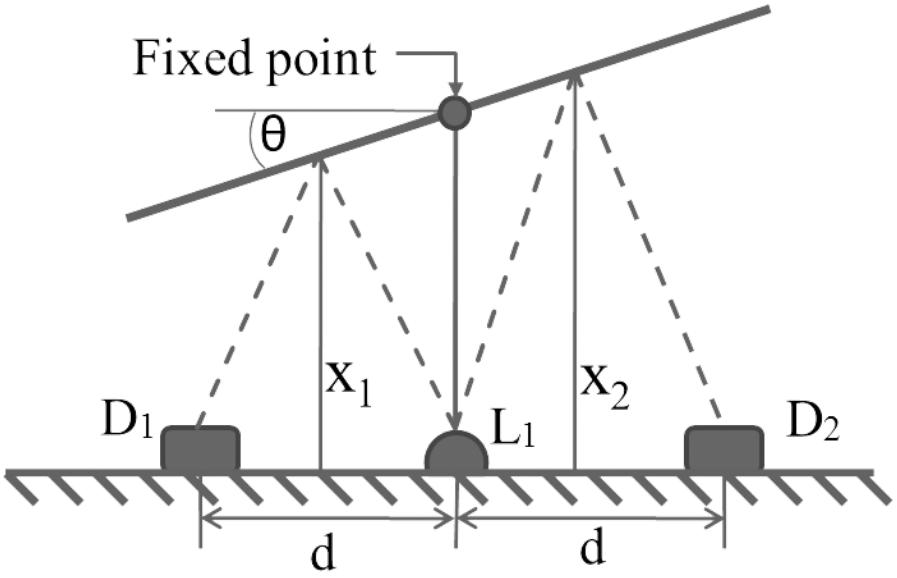

Figure 2.5: This figure shows part of the sensor array, two photodiodes (D_1, D_2) and between them an infrared LED (L_1). The infrared LED illuminates the target surface, which reflects the light to photodiodes with the angle of incidence θ. The distance based on the first sensor reading is x_1, and x_2 for the second sensor. The d parameter indicates the distance between the infrared LED and the photodiode.

$$\theta = \arctan(\frac{x_2 - x_1}{d}) \tag{2.2}$$

where x_1 and x_2 are the perpendicular distances of object points (see Fig. 2.5) and d is the spacing distance between photodiodes and LEDs on the sensor board. Using estimates θ', x_1', x_2' of the true values the following simple iterative steps are taken:

1. Initialize θ' to $0°$
2. Calculate x_1', x_2' using (1)
3. Calculate θ' using (2)
4. Go back to (2) until convergence

The process is deemed to converge when the difference between two consecutive estimates of θ becomes lower than a given threshold, in this case $1°$. Fig. 2.6 shows the measurement errors at 0, 1 and 2 iterations for a number of angles in the $-45°$ to $45°$ range. It can be seen that at every iteration step, the error decreases by

DOI:10.15774/PPKE.ITK.2012.003

about 25%. With only two iterations, the maximum error is already less than 0.3°, meaning only about ±6 μm uncertainty in the measurement when the angle of incidence is around 45°. This iterative process can be done without requiring new sensorial data so it is implemented very fast, even on a microcontroller. With this method the iteration number can be dynamically varied based on the requested precision or on the current value of the angle of incidence.

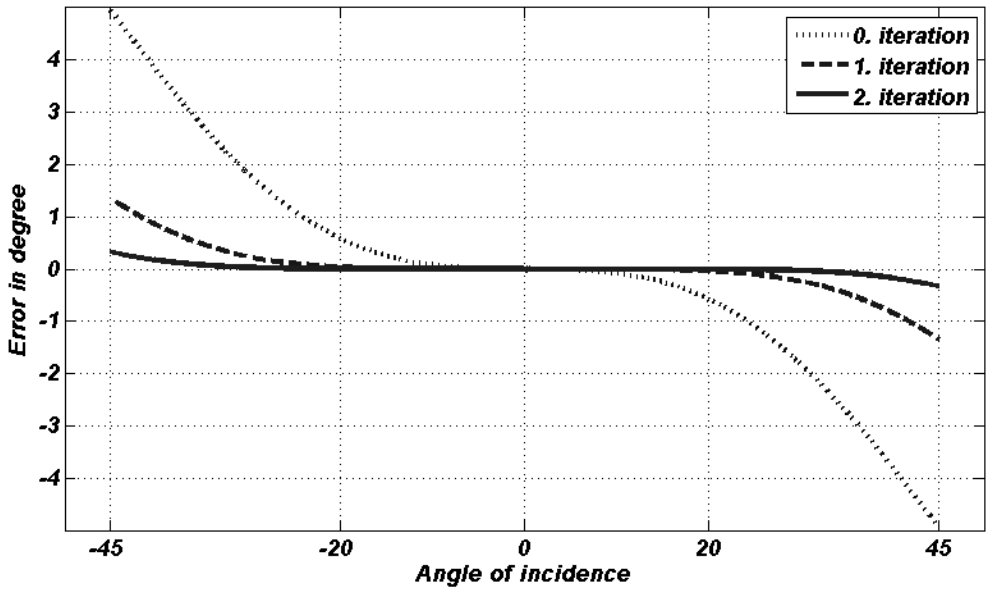

Figure 2.6: Difference between the real θ and estimated θ' values obtained with Eq. 2.2, with different number of iteration used. It can be seen that the error level after the second iteration process is smaller than 0.3° at the angle of incidence 45°. This corresponds to a ±6 μm uncertainty in the measurement.

2.4.2 Edge reconstruction and object outline detection

Even though the infrared LEDs are highly directional, some light does get reflected off the sides of the scanned object, causing blurring along the scanning direction. To counter this effect, a fourth order polynomial fit is made in the scanning direction and normalized into a 0-1 range. The image is then scaled using the normalized polynomial fit. This operation preserves the face of the object while sharpening the edges. It is emphasized that in the case of a 2D sensor array, the need for mechanical scanning – and hence the need to deblur – arises less often.

The outline of the object has to be known in order to have safe navigation or to make interaction. For example, a robotic manipulator has to know the occupied

DOI:10.15774/PPKE.ITK.2012.003

areas in its working space at a given height for avoidance or for picking or placing objects. As the infrared sensor array supplies single view 3D back projection images of the object by creating a surface cut at a certain threshold, the resulting images will indicate the occupied areas at the height of the cut. To determine this threshold one solution could be to make the cut near to the detected ground. Alternatively the threshold could be determined according to a specific task: for example, in the case of the robot manipulator, the height of the cut could be the same height where the end effector is, or in the case of a mobile robot it could be the height of the maximum object which the robot can drive through without a problem.

DOI:10.15774/PPKE.ITK.2012.003

2.5 Experimental results

The capabilities of the sensor array were tested by measuring the angle of incidence with the proposed method in Section IV. The results of the object scanning (Fig. 2.4/I.) and mobile robot experiment (Fig. 2.4/II.) are presented.

2.5.1 Measuring the angle of incidence

To validate the proposed method, an experimental setup similar to Fig. 2.5 was devised. A flat object was placed 20 cm above the sensor array. Only the angle of incidence was changed between $-45°$ to $45°$ and the object distance was fixed. Fig. 2.7 shows the simulated and the measured distances. It can be seen that without giving assumption for the angle of incidence, the distance measurement can have a relatively high error ($\sim$15%).

After using the iterative process described above, the error was substantially decreased after only three iterations, both in the case of the simulation and measurement. In the case of the real array, a 3 mm error could still be obtained after three iterations (object 20 cm away, at $45°$). This was caused by the measurement noise; however, the measurement error was decreased by about one order of magnitude.

2.5.2 Object scanning experiments

2.5.2.1 Edge reconstruction and object outline detection

In the case of the scanning experimental setup (Fig. 2.4/I.) the data was processed as follows: first the sensor raw output was compensated for offset and ambient light and converted to distance and labeled as 'original image', then the angle of incidence correction method was used, and finally, the image is then scaled using the normalized polynomial fit to create the 'result image'. After the scanning process, the outline and the surface of the detected objects was tried to be recreated. The first measured object was a red wooden block cube (Fig. 2.8/a). On the original image the effect of the smoothing in the scanning direction can be well distinguished that was much lower in case of the result image. The top view of the original and result images also can be observed on Fig. 2.8/a where the threshold function was set to 2 cm and the result is marked with white lines. In case of the original image it marked a 6×4 pixel sized area and in case of the result image it marked a 4×4 pixel array, where each pixel size was 8 mm (both in the

DOI:10.15774/PPKE.ITK.2012.003

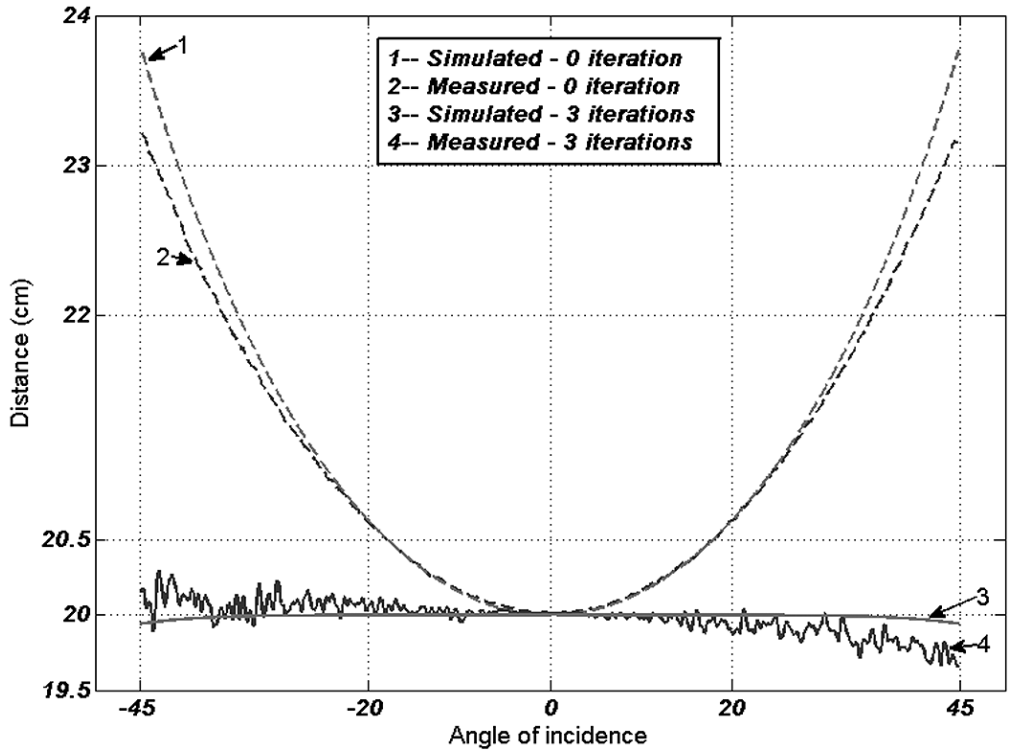

Figure 2.7: Measurement and simulation result of the sensor array of an object (placed 20 cm above) at different angles of incidence, with the assumption that the angle of incidence is 0° (in Eq. (2.1) $\cos\theta$ was equal to 1). This could be corrected with an iterative method where an assumption for the angle of incidence could be given. As the third and fourth line show the simulated and measured distance after 3 iterations using this method highly improves the distance measurement.

x, y direction) suggesting that the scanned object dimensions were $W = 32$ mm, $L = 32$ mm.

The second scanned object was a solid wooden U-shaped block (Fig. 2.8/b). The edges of the U-shape were smoothed because the object was not well aligned with the sensor grid. The middle curve was measured to be 5 mm smaller than the actual distance because of the deflection from the inner curve of the U-shape. On the top view the side edges and the size of the object are visible. To outline the object, the surface cut was made near the ground at 1 cm. The outline of the object was marked successfully, as can be seen on the top view in Fig. 2.8/b. The outline suggests that the dimensions of the object were $W = 32$ mm and $L = 96$ mm.

DOI:10.15774/PPKE.ITK.2012.003

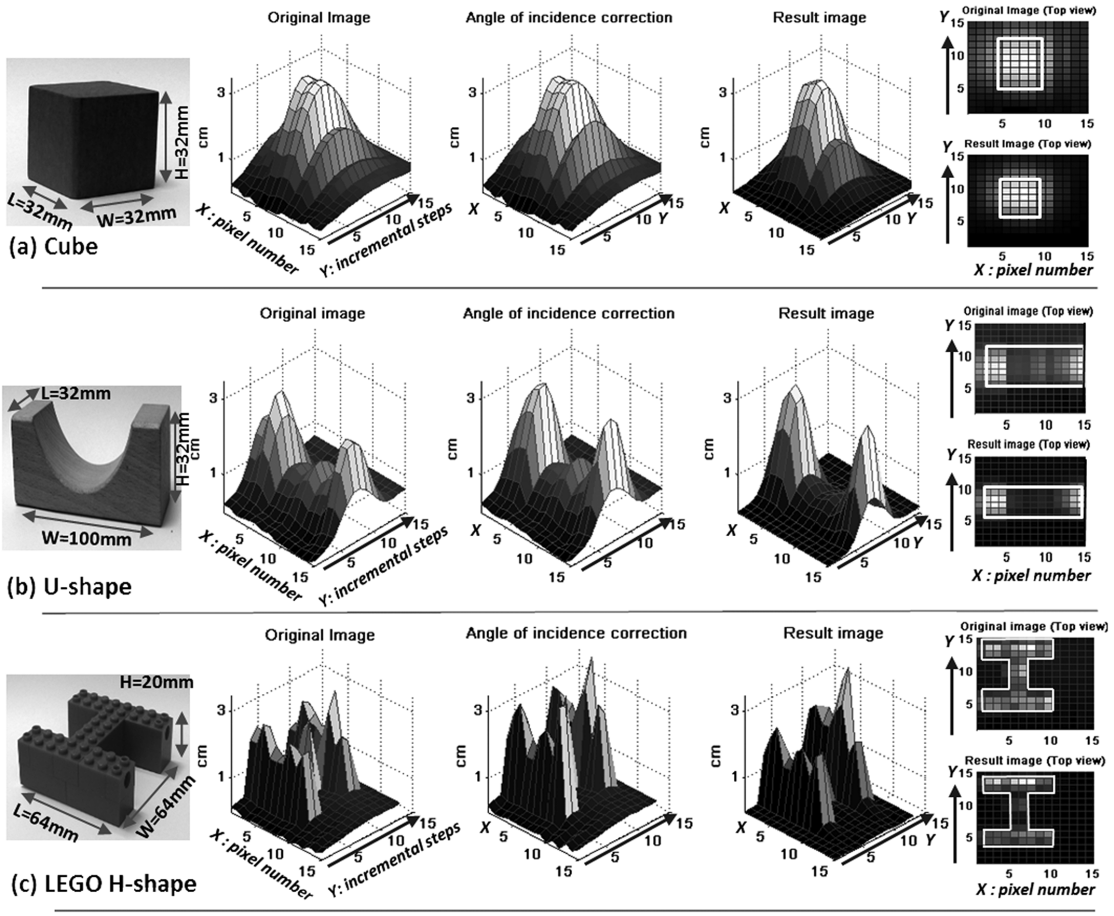

Figure 2.8: Results of the experimental setup I. (Fig. 2.4/I.), where the (a),(b),(c), objects were placed under a x, y, z plotter table. The x axis indicates the number of the pixels, y is the scanning direction (also marked with an arrow) and the z axis shows the distance in cm. The original image is made from the sensor row output after ambient light and offset compensation and conversion to distance. The result of the angle of incidence correction is presented. During the scanning process, as the sensor array moved closer to the measured object,light is also reflected from the side of the object causing false distance estimation and blurring the edges in the scanning direction. To sharpen these edges the images were scaled by their normalized polynomial fit creating the result image. The top view of each object shows the size of the object in case of the original image and result image where a threshold function was applied and the result is marked with white lines.

2.5.2.2 Surface trace

The sensor array capabilities for object surface-trace reconstruction were also tested using a shiny object (Fig. 2.4/c). As can be seen in Fig. 2.8/a where a cube was measured the object flat surface was successfully recreated except near the edges. Also in Fig. 2.8/b, the real object can be recognized but the edges were blurred.

DOI:10.15774/PPKE.ITK.2012.003

As a conclusion this sensor array was capable of creating surface-trace of objects but only in a limited way. To demonstrate these problems, an H shaped structure from red LEGO blocks was formed. The result of the scanning process can be seen in Fig. 2.8/c. Since the surface of the LEGO was shiny, and the small joining parts on the top were scattering thus false peaks in the distance measurement appear. Hence, the angle of incidence correction cannot be used as in this case the false peaks were even more increased. The main problems of the procedure were with the edges as there were deflection and scattering. As a consequence detailed objects were hard to capture. Also the surface of the object should be diffuse otherwise the effect of the scattering was higher. However, the outline of the object could still be recognized as the top view of the original image demonstrated.

2.5.2.3 Image registration

Three coin batteries (d = 20 mm, h = 5 mm) were placed under the sensor array, two on each other and one next to those 2.9/(a). If a camera had been mounted to the robot feet an ideal output image would be 2.9/(b) (note that, from such a small distance, special fish-eye lenses and correction algorithms would be needed to produce such an image), where there are no additional information about the object high. The sensor low resolution image ($8x8$) can be seen in 2.9/(c). From such an image hard to make reliable decisions about any of the object's properties.

By only making eight additional image (during the robot leg in motion) with the sensor array in each direction a higher resolution image can be created 2.9/(d), where the object form, hight and width can be more clearly depicted. If a higher resolution is needed it can be achieved by using more sensors in the array or making smaller incrementation steps in each direction. Thus the time (how long it takes to create a registered image) and the number of sensors can be optimised.

With this method by using a low resolution sensor array obstacle detection can be made. The number of the registered and jointed images can be dynamically set based on the resolution needed, or it can be based on visual attention (if an object is detected than the number of images can be increased).

DOI:10.15774/PPKE.ITK.2012.003

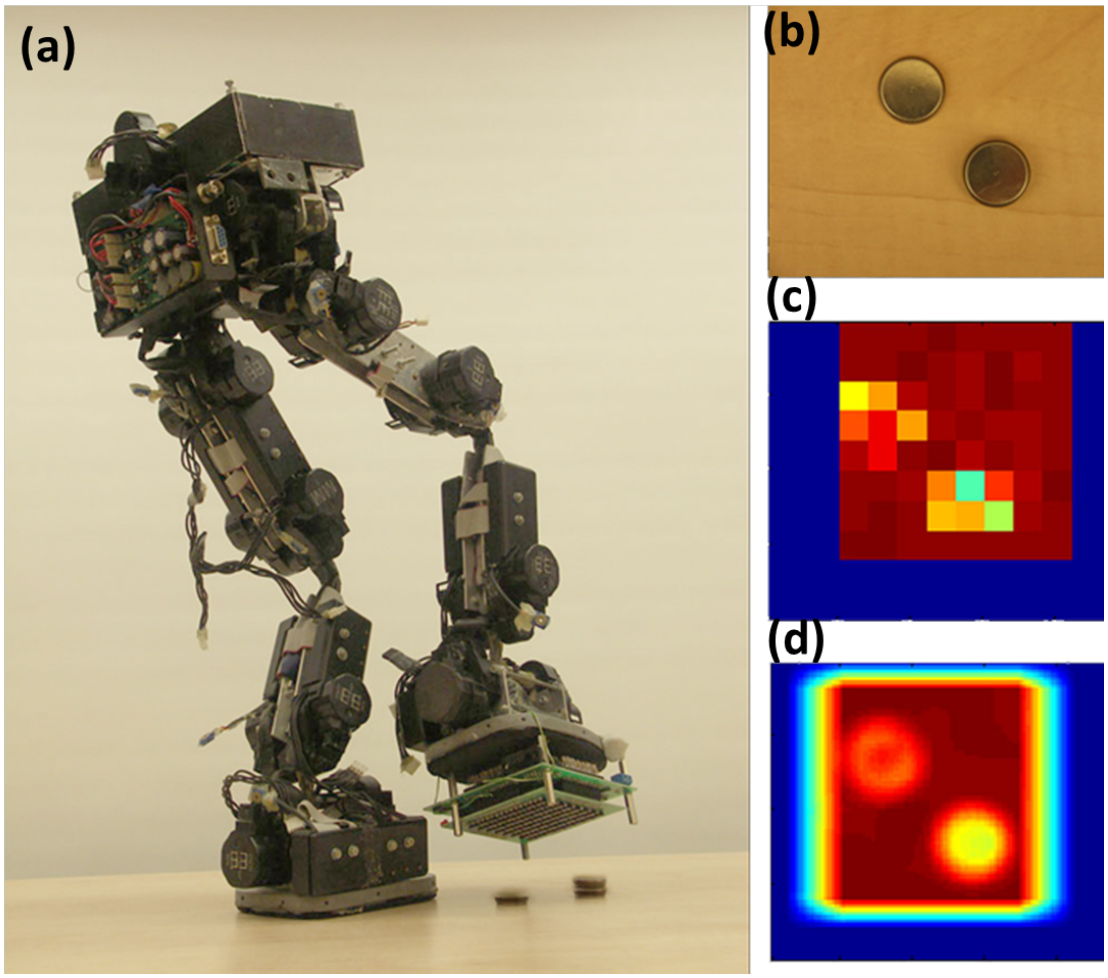

Figure 2.9: The previous version of the sensor array (describen in [4]) was attached to a bipedal robot [3] in order to detect obstacles under the robot feet (a). (b) shows an ideal case when a camera was attached to the robot feet and image was captured (note that, from such a small distance special fish-eye lenses and correction algorithms would be needed to produce such an image) (c) is the low resolution output of the $8x8$ sensor array. Simulating the robot feet motion with the plotter table during its motion an extra 8 sensor measurement was made in each direction, and these were registered and joint together to produce a higher resolution image (d) where the object outline and the fact that the second object was higher can be depicted. [1]

2.5.3 Mobile robot experiments

2.5.3.1 Landmark detection

Materials at the same distance but with different reflection properties could be used to mark objects or to code information, for example different kinds of shapes

DOI:10.15774/PPKE.ITK.2012.003

can be drawn on the surface and could be used as landmarks for navigation.

A plus, a triangle, and a square shape were formed on the floor using 1.5 cm wide and 10 cm long white strips of masking tape. The robot was driven over each shape and the measurement result can be seen on Fig. 2.10. In case of the plus shape (Fig. 2.10/a) the edges were blurred but recognizable. The result could be improved by using wider strips, or by using a color that provides higher contrast to the background (floor). Fig. 2.10/b shows a triangle; the middle of the triangle was hardly captured because of the reflection from the side strips. The vertices of the triangle were missed as they were smaller than the pixel resolution. In the case of the square (Fig. 2.10/c) the corners gave higher responses than the straight parts. This was because the used white strip was somewhat transparent and the more layer were covering the more light was reflected. Thus at the corners where two strips are overlapping the given landmark reflects more light. This can also be observed with the other shapes as well.

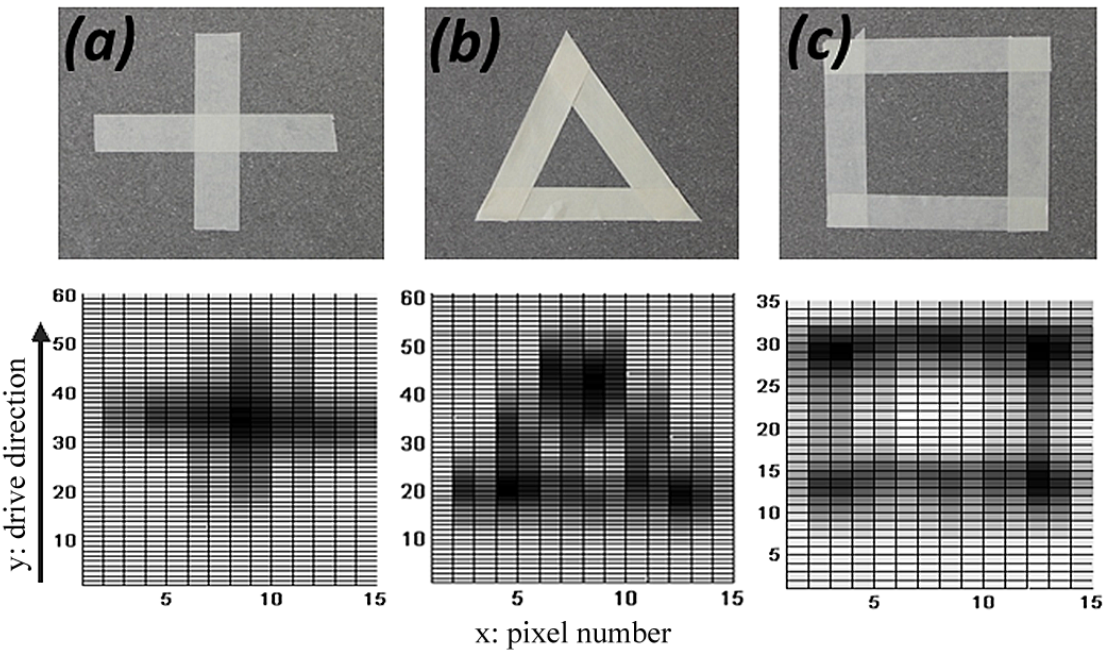

Figure 2.10: Scan result of different landmarks. On the top are the pictures of the used landmarks and on the bottom the images created with the sensor array attached on a mobile robot.

[1]Image used with permission of Miklós Koller, the image was created as a part of his M.Sc degree under my supervision

DOI:10.15774/PPKE.ITK.2012.003

2.5.3.2 Door-step detection

The PowerBot was driven over on a door step (phase $S1 - S2$ in Fig. 2.11/c). The two high responses visible in Fig. 2.11/a,b near to $S2$ were the highly reflective metal protectors on the edges, a wooden surface in between.

A longer scanning result (∼4 second) of a drive through process is shown in Fig. 2.11/b (each main phase is indicated in Fig. 2.11/c).

After the robot started to move the doorstep was detected before the front wheel reached it. As the front wheels got on the door step the distance between the ground and the sensor was increased thus less light was reflected to the sensor. A straight motion was recorded until the rear wheels arrived to the door step and pushed the robot front down thus the distance between the ground and the sensor was decreased and more light was reflected to the sensor.

With this method the doorstep (or any obstacle) and each phase of a drive through process can be detected before the robot reaches, and based on the measured sensor output it can be decided to stop the mobile robot or increase the speed to be able to go through the obstacle. It should be noted that precise (material independent) measurement could be done by using supplementary distance measurement sensor (for instance, ultrasound).

2.5.3.3 Map building (SLAM)

In a proof of the concept localization experiment, the PowerBot robot was driven on the linoleum floor of the laboratory. The measured data (part of a map) can be seen in Fig. 2.12/a. Shorter straight motion was also made in the same region; the sensor output is shown in Fig. 2.12/b. It could be easily depicted, with commonly used SLAM techniques, which part of the previously made motion was repeated and in this way the location of the robot could be estimated.

It should be noted that seeing the experimental results, the proposed measurement technique might give a possible solution for the problem of low cost SLAM at home or in industrial robotics. However, creating SLAM with a one row sensor array pattern matching would be too difficult without knowing the exact speed and orientation of the robot. This problem probably could be solved by extending the sensor array into 2D (8×8 or more), but this claim has to be supported by further experiments in the future.

DOI:10.15774/PPKE.ITK.2012.003

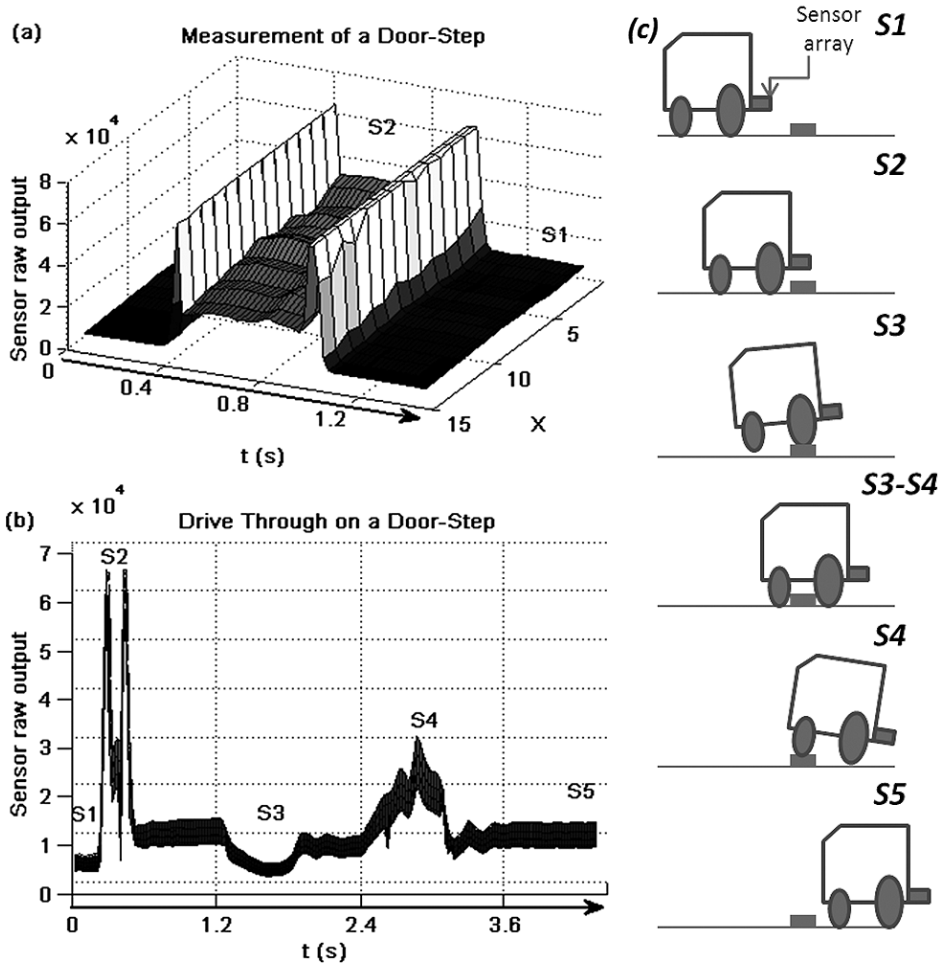

Figure 2.11: The sensor array was mounted on a PowerBot type mobile robot front bumper and was directed to the ground, measurements were taken while the robot was moving. (a) shows the sensor output of a door-step while the PowerBot is driven over with a constant speed (phase $S1 - S2$ in (c)). The high peaks in the measurements are caused by the metal protectors on the door-step edges, and in between the wooden surface can be seen. (b) shows a drive through process where each phase of the drive through process can be recognized (the cross-section for each sensor value have been plotted on top of each other) and (c) indicates each phase. The robot started to move after $S1$, the edge of the door-step is detected at $S2$. After the sensor array got through the door-step there was a straight motion (between $S2, S3$) indicating higher sensor responses as the floor material was different in this room. At $S3$ the distance of the sensor array was increasing from the ground as the first wheels got on the door-step and lifted the front side of the mobile robot. $S4$ indicates when the back wheels reached the door-step and pushed the robot front down and after a straight motion in the new room could be observed $S5$.

DOI:10.15774/PPKE.ITK.2012.003

2. INFRARED SENSOR ARRAY

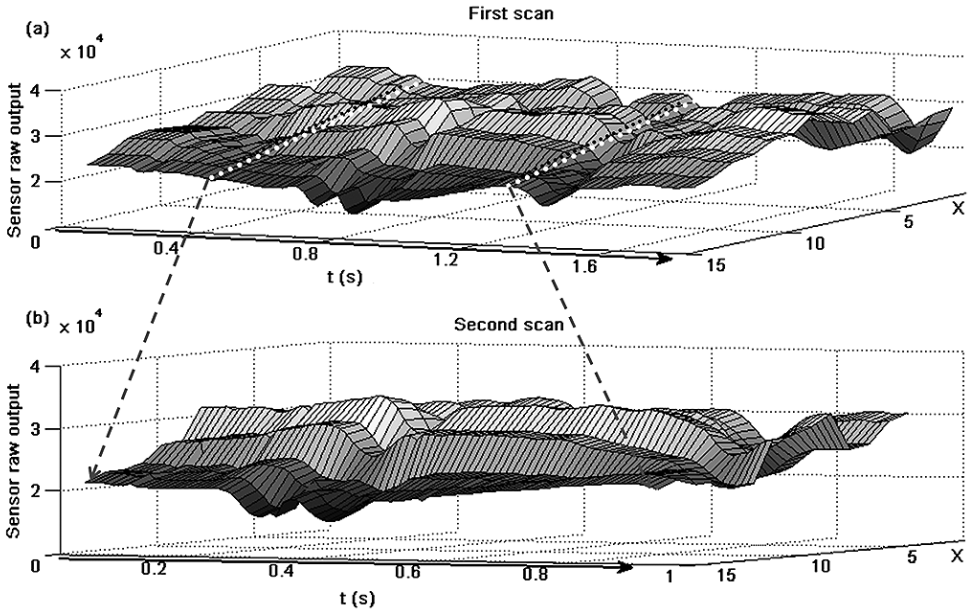

Figure 2.12: (a) shows a scan result of part of a laboratory (covered with linoleum). The changes in the raw output is caused by the color/contrast change in the material.(b) shows the result of a second scanning process on part of the same area. By comparing the two images it can be identified which part of the motion was repeated (marked with white dotted line on (a)). This sensorial data could be used as supplementary data for creating SLAM.

DOI:10.15774/PPKE.ITK.2012.003

2.6 Conclusion

In this chapter a novel infrared LED and photodiode based distance measurement array has been presented. The two main advantages of the system are the fast readout speed and high resolution in the distance measurement. Additionally, the array structure helps to improve the pixel resolution and also helps in the calculation of the angle of incidence. The sensor array capabilities were examined for outline and surface-trace detection of various objects. The device has proved useful but with some limitations. One problem is the deflection that smooths the edges. Furthermore, the reflected amount of light highly depends on the brightness of the object, but this could be improved by using a supplementary distance measurement sensor (e.g. US). Measurement results with a mobile robot were also presented. A door-step was successfully measured and each phase of the drive through process could be well distinguished. It was also shown that the developed sensor array was capable of detecting ground landmarks for navigation purposes. The measurement accuracy could be improved by using higher resolution sensor array (smaller distance between the infrared LED and photodiode) and more directional light source.

Although the presented solution may not be as accurate as for example laser scanners or camera systems are, normally low resolution data is enough for object detection, avoidance and classification tasks. Also in those environments where the operation speed is crucial and computation power has to be small a compromise has to be made between resolution and speed. This sensor array could be useful in many applications, for example in production lines for object classification or orientation detection, or in robot navigation (landmark detection), obstacle avoidance and detection and for SLAM in consumer and industrial robotics. The summary of the contributions are the following:

- a new solution has been given for object outline and surface trace detection with 8×1 LED-photodiode pair based sensor array
- resolution greater than the spacing between infrared LED and photodiode pairs has been achieved
- an iterative method has been described to calculate the angle of incidence for achieving more precise distance measurement
- mobile robot applications (landmark, doorstep (obstacle) detection) has been examined for localization purposes

DOI:10.15774/PPKE.ITK.2012.003

2. INFRARED SENSOR ARRAY

As conclusion the following thesis points can be stated:

Thesis I.:

Object outline and surface trace detection using 3D imaging based a low resolution proximity array containing infra LEDs - photodiodes.

A: I have designed and implemented a low resolution infra LED - photodiode based proximity array. Using several photodiodes to detect the reflected light from each infra LED, an iterative method was developed to calculate the angle of incidence in case of flat objects with known α_i parameters, to achieve more precise distance measurement.

B: A new method has been given to decrease the smoothing effect at object edges during the sensor array motion.

C: *I have demonstrated in mobile robot experiments that the sensor array is capable of detecting on road localization landmarks and obstacles before crossing.*

Published in: [1]

DOI:10.15774/PPKE.ITK.2012.003

Chapter 3

Complaint 3D Tactile Sensor

3.1 Introduction

Robots today are already able to perform various tasks such as walking or dancing. In a well modeled environment even without external sensorial feedback, they can already execute a number of tasks [14]. In an unstructured environment however, they must sense their surroundings and make contact with various objects. Equip today's humanoid robots with an advanced grasp and manipulation capabilities are the ultimate goal. In order to create complicated manipulation tasks, tactile information is essential. The robot hand equipped with tactile sensors should be capable of detecting when contact occurred and should be able to identify shapes, object texture, forces and slippage. There are only a few tactile sensors available on the market and most of these sensors have a rigid structure. A typical single sensor type is the Force Sensing Resistor (FSR) available in many shapes and sizes (d=5 - 50mm). Larger matrix based sensor arrays are available from e.g. Tekscan. Both of these are only capable of measuring normal forces.

The basic problem with these kind of sensors, as demonstrated by *Russell* [50], is that rigid tactile sensors provide little information for all but very flat and hard objects.

Compliant tactile sensors would allow the sensor surface to deform on the gripped object thus the contact area increased and the stability of the precision grip. And in case of power grasping the compliant surface would also help to share the forces on a bigger area. In many researches a soft material is placed on these rigid sensors to meet this need [51] but this solution makes the tactile inversion problem even harder.

DOI:10.15774/PPKE.ITK.2012.003

3. COMPLAINT 3D TACTILE SENSOR

A few articles describes compliant tactile sensors which are suitable to use on a robotic hand. One interesting fingertip tactile sensor is presented by *Choi et al.* [52] using polyvinylidene fluoride (PVDF), and pressure variable resistor ink to detect normal forces as well as slip. *Hellard et al.* [53] shows a sensor array utilizes the properties of optical dispersion and mechanical compliance of urethane foam. As a force is applied onto the urethane foam due to the compression the intensity of scattered radiation is increased and the photodetector output will change accordingly. The greatest advantages of this sensor are the easy manufacturing process, durability, scalability, low cost and having good sensitivity. However, covering a larger area with a dense sensor array (e.g 25 sensing points per square cm) on a robot hand is very hard to achieve. One reason for this is that the data produced by such an array is hard to process. The physical implementation of the wiring is even more challenging. Researchers try to create wireless solutions [54] or use optical methods to decrease the number of the wires [55]. Most of the optical tactile sensors utilize a CCD or CMOS camera to capture the deformation of a surface caused by external force [56] they are multitouch but their size and computation power makes it difficult to use on a robot hand yet. Another very clever solution is to place a six DOF force/torque sensor inside the fingertip [57, 58]. The applied force can be measured and the point of contact can be calculated on the whole surface of the fingertip [59].

Tactile sensors placed on a robot hand should not just sense the normal forces, but should also be able to detect the force incidence angle. Most of 3D sensors are MEMS based [60] and have already proven to be useful in detecting and identifying slippage and twisting motion [61]. However covering larger areas would be too difficult.

In this chapter, an easily scalable (fingertip or palm sized) 3D optical tactile sensor covered with a compliant surface is presented. The silicone rubber cover makes it prone to contact and will increase the grasp stability. A layer structured silicone cover is also presented to increase the noise performance and reduce the size. The presented sensor prototype is 35 mm in diameter and 30 mm high, and the point of contact, direction and magnitude of the applied force can be measured on the whole surface. The sensor output is analog and request only a minimal number of electrical component to connect to a microcontroller or to a PC. It has a robust structure with a respectable overload capability, high sensitivity (threshold 2g), high static load range ($\geq$2000:1), and high speed operation (in KHz range).

DOI:10.15774/PPKE.ITK.2012.003

3.2 Design concepts

The elastic deformation of a material is proportional to the applied force. If the compression of the material is measured and its Young modulus is known than the applied force can be calculated. In this way, the force measurement problem can be turned into a distance measurement problem.

To measure distance in a non contact way the traditional methods are the ultrasonic and optical solutions. The US sensor measures the time of flight (ToF) of the ultrasound signal emitted and reflected to the receiver. Today's ultrasonic sensors have an average diameter of 15 mm and the minimal sensing distance of a few centimeters (3 cm). The most common offset-based Position Sensing Devices (PSD) such as *Sharp GP* series are a size of 44 mm x 13 mm with a minimal sensing distance of 4 cm (Model GP2D120, range 4-30 cm).

Unfortunately using these sensors would make the tactile sensor too large due to their dimensions and minimal sensing range. A possible solution could be to use infrared LED and photodiode pairs, arranged in a reflective configuration. The reason why this method is not frequently used for accurate distance measurements is that the reflected amount of light highly depends on the reflective properties of the sensed object surface thus material independent distance measurement is difficult to achieve. However, in this case, where the used elastic material properties are constant it can be used responsibly.

The tactile sensor surface should be prone to contact with any kind of object at any kind of angle. For this reason, the shape of its surface was chosen to be a hemisphere like. The sensor should also have a reliable overload capacity before permanent damage is caused. The dynamic range should be in KHz range in order to be able to detect vibration. The composed material should be durable and in-expensive with a repeatable sensor response with no (or minimal) hysteresis.

DOI:10.15774/PPKE.ITK.2012.003

3.3 Sensor description

The base of the tactile sensor is composed of three photodiodes and an infrared LED. The photodiodes are placed around a circle at every 120° and an infrared LED is in the middle (Fig. 3.1/a). This is covered with a hollow elastic dome as a spherical interface, made form silicone rubber (RTV-2 type), that is fixed to the PCB (Fig. 3.1/b). The thickness of the dome will determine the range of measurement: the thinner it is, the more it will deform for a given load. The number of the used components and their size makes the sensor size easily scalable. The sensor capabilities highly depend on the photodiodes amplification value, the photodiode sensitivity, infra LED power and the material of the cover to obtain an optimal solution their relation should be analyzed.

The optical measurement method helps to achieve a high dynamic range both, in the distance, and in the time domain. The sensor read out speed could be even in the MHz range, and as the output signal is analog the achieved resolution only depends on the used Analog to Digital Converter (ADC). The sensor structure is very durable, if the external force is greater than the maximum desired force applied onto the elastic dome, it can be deformed until it reaches the PCB level resulting in a respectable overload capacity. As the silicone cover material has elastic and viscoelastic properties after the force was released a relaxation period could be observed, which was proportional with the applied force, however to modell this phenomena is part of the future researches.

The basic mechanism of the 3D tactile sensor is that the amount of force measured with the three separated photodiode are used to estimate tridirectional forces imposed on the sensor. The measurement principle is as follows: the infrared LED lights illuminate the inner structure of the dome. At no force, the reflected amount of light to each photodiode is equal. A force applied on the surface will result in deformation, on this region the surface of the dome will be closer to a given photodiode thus more light will be reflected to that sensor (Fig. 3.1/b).

For practical purposes, only three photo diodes were used in the first prototype. As a result, the equations (Eq. 3.3) are only approximations as in this case the origin of the calculated axis is not in the center (on the infra LED), thus to measure the independent x,y force component, this offset must be taken into account. However, by using four photo diodes, each axis can be calculated as the difference of the two opposite photodiodes on one axis and in this case the origin will be in the middle of the infra LED without having an offset.

DOI:10.15774/PPKE.ITK.2012.003

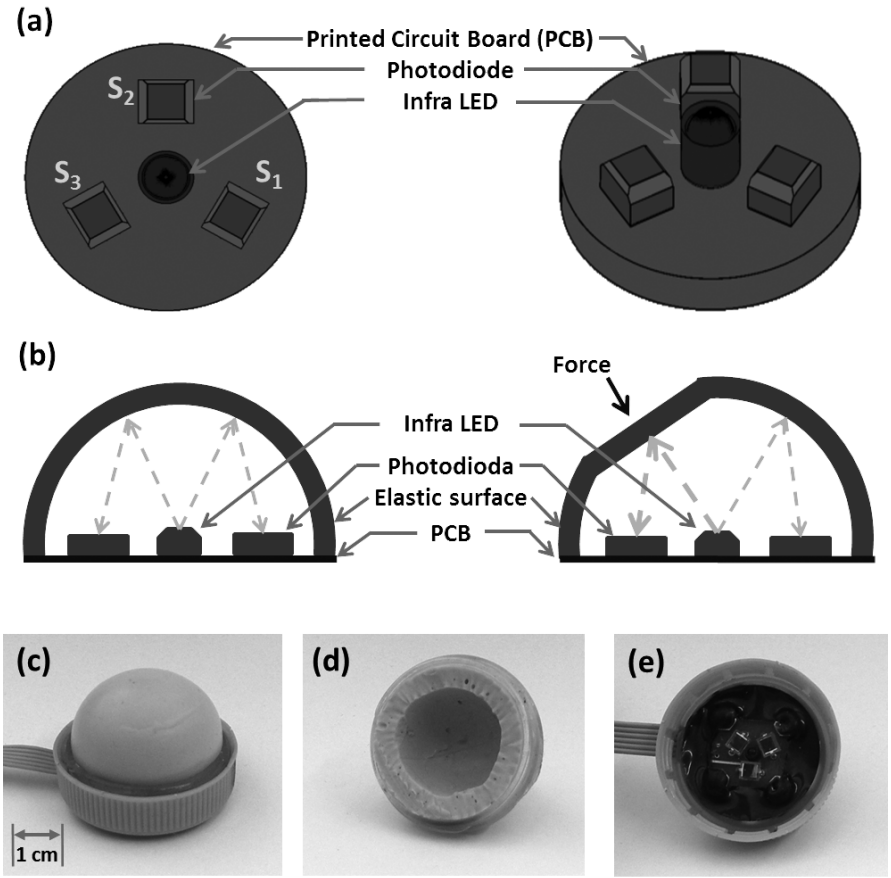

Figure 3.1: Schematic drawing of the tactile sensor, the three photodiodes are placed around on a circle at every 120° and an infrared LED is in the middle mounted on a PCB board (a). It is covered with an elastic hollow dome. A force applied on the elastic cover will result deformation (b). This deformation is proportional to the reflected light to the appropriate photodiode thus the applied force can be measured. The basic mechanism of the 3D tactile sensor is that the amount of force measured on the three separated pressure are used to estimate tridirectional forces imposed on the sensor. The proof of the concept version of the sensor is presented on (c), with the hollow elastic silicone cover (d) and the PCB (e).

The measurement of the three photodiodes (S_1,S_2,S_3) could be used to estimate the normal (F_z) and the tangential force components (F_x,F_y) using the following equations:

$$F_x = k(\frac{(S_2 - \beta_2) + (S_3 - \beta_3)}{2} - (S_1 - \beta_1)) \tag{3.1}$$

$$F_y = k(S_2 - \beta_2) - (S_3 - \beta_3)) \tag{3.2}$$

DOI:10.15774/PPKE.ITK.2012.003

3. COMPLAINT 3D TACTILE SENSOR

$$F_z = k(\frac{\sum_3^{i=1}(S_i - \beta_i)}{3}) \tag{3.3}$$

where β_i is composed of two values namely the sensor output without infrared light emission (sensor offset) and the sensor output with infrared light emission at no force applied (calibration value) and k is the spring constant (now it is taken to be one).

The used infrared LED (Model TSHF5210, Vishay Ltd, US) is driven by a microcontroller (Model PIC24HJ32GP204, Microchip, US). While the infrared LED is on the photodiodes (Model BPW34, Vishay Ltd, US) outputs after amplification are converted to digital with a 24 bit ADC (Model ADS1258, TI, US) (but only 18 bit resolution is used where the two highest MSB is negligate thus the output representation is 16bit) and are sent to the PC via a USB port (Fig. 3.2).

The photodiode characteristic is non-linear, to be closer to the linear output in the measurement range the infrared LED current is set based on its output characteristic. Thus the photodiode output characteristic will have the highest change at the range where no load or maximal load applied. As the measuring method is optical the infra light illumination must be very stable. Although the infra LED is current controlled, illumination change during the system initialization could be observed, this was because of the temperature changing inside the LED caused by the current flow. Even so, as soon as the LED crystal reached its working temperature (∼1 min) the output signal became stable.

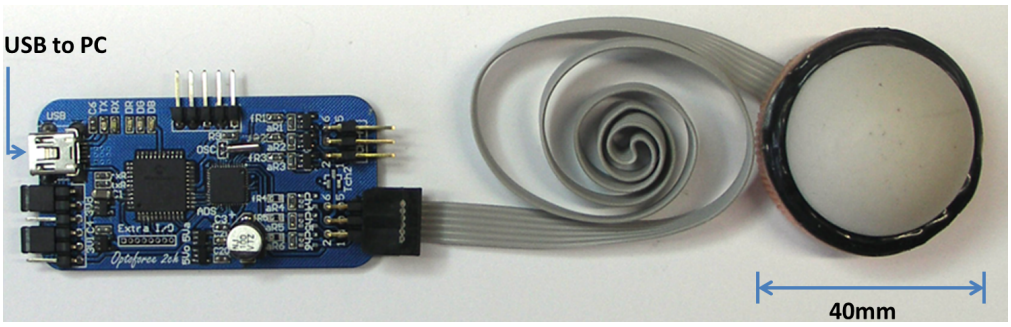

Figure 3.2: The data acquisition board and a connected tactile sensor prototype. The board is capable of processing the signals of two sensors and it sends to the PC through USB port.

DOI:10.15774/PPKE.ITK.2012.003

3.3.1 Theory of operation

In this section a short description will be given about the sensor simplified operation in 2D case. The inside of the semicircle is illuminated with a point light source (infra led) with an intensity of L from its middle point (origin), and the reflected amount of light is measured in two points (photo diodes) equally placed from the origin with a distance of D_S (Fig. 3.4).

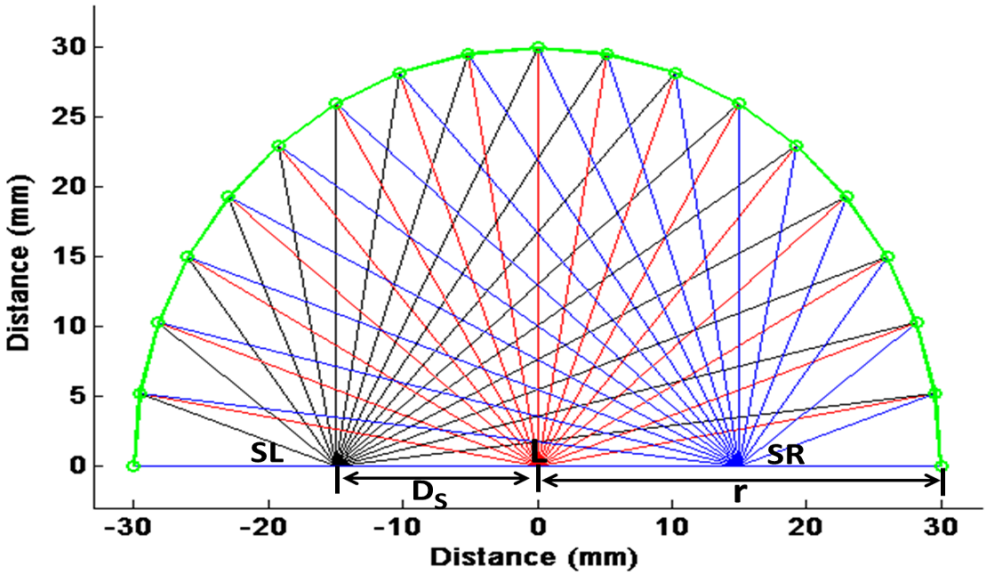

Figure 3.3: Schematic drawing of the semicircle where in the origin is the point source (infra LED) and on two sides are the detectors SL, SR (photo diodes). The red lines represent the light rays from the point source, and with blue and black lines the reflected ray to the detectors are marked, r is the radius of the semicircle and D_S is the detector distance of the origin.

Based on the inverse square law the light intensity at each point of the semicircle can be calculated:

$$L_C(r) = \frac{L}{\pi r} \tag{3.4}$$

where r is the radius of the semicircle, C is the circumference and s is the length of the arc. Each point on the semicircle is taken as a new light source so to calculate the reflected amount of light to each photo diode (SL: photo diode left, SR: photo diode right). The inverse square low is used as well. The distance between the

DOI:10.15774/PPKE.ITK.2012.003

photo diode and semicircle points can be expressed as:

$$D_{SR}(\alpha) = \sqrt{(r\cos(\alpha) - D_S)^2 + (r\sin(\alpha))^2}, \alpha \in [0, \pi] \tag{3.5}$$

$$D_{SL}(\alpha) = \sqrt{(r\cos(\alpha) + D_S)^2 + (r\sin(\alpha))^2}, \alpha \in [0, \pi], \tag{3.6}$$

where α is calculated in radian and can be expressed based on the length of the arc:

$$\alpha = \frac{s}{r} \tag{3.7}$$

Thus by using the inverse square low the intensity at each photo diode can be calculated using the following equations:

$$L_{SR} = \int_0^{\frac{C}{2}} \frac{L}{\pi r} \frac{1}{\pi\sqrt{(r\cos(\frac{s}{r}) - D_S)^2 + (r\sin(\frac{s}{r}))^2}} ds \tag{3.8}$$

$$L_{SL} = \int_0^{\frac{C}{2}} \frac{L}{\pi r} \frac{1}{\pi\sqrt{(r\cos(\frac{s}{r}) + D_S)^2 + (r\sin(\frac{s}{r}))^2}} ds. \tag{3.9}$$

To simulate this model the equations were solved using numeric approximation in Matlab. The semicircle radius was set to r=30 mm and the light intensity to L=10W/sr with N number of rays. The number of rays were set to 18000 as in this case the simulation error settled at a reasonable level of 0.006%, so in the simulation α_i goes from 0 to π with an increment of π/N but for practical reasons on the figures only 18 rays are plotted. The deformation was added to the model by overwriting the semicircle equation between two arbitrary angles. For example, by setting it from 60° to 120°, the $y(\alpha_i) = y(\alpha_i - 1)$ (where $\alpha_i \in [0, \pi]$) the semicircle top will be flat as it can be seen in Fig. 3.4/b. This method results that the original length of the semicircle arc will be changed, thus Eq. 3.7 is no longer true. In case of deformation, the circumference can be calculated by summing the length of the arcs using the following equation:

$$C = \sum_{i=1}^{\pi} \sqrt{(x(\alpha_i + 1) + x(\alpha_i))^2 + (y(\alpha_i + 1) + y(\alpha_i))^2} \tag{3.10}$$

Using a different deformation factor the light intensity was measured at point SL and SR as it can be seen in Fig. 3.4/a. Without deformation both intensities

DOI:10.15774/PPKE.ITK.2012.003

(L_{SL},L_{SR}) are the same. If there is a deformation parallel with the ground (x axis), then the intensity will be increased equally both in SL and SR. In case of side deformation the light intensity increases on the same side as the deformation was, thus it can be stated that the degree and direction of deformation is proportional with the measured light intensity at point SL and SR.

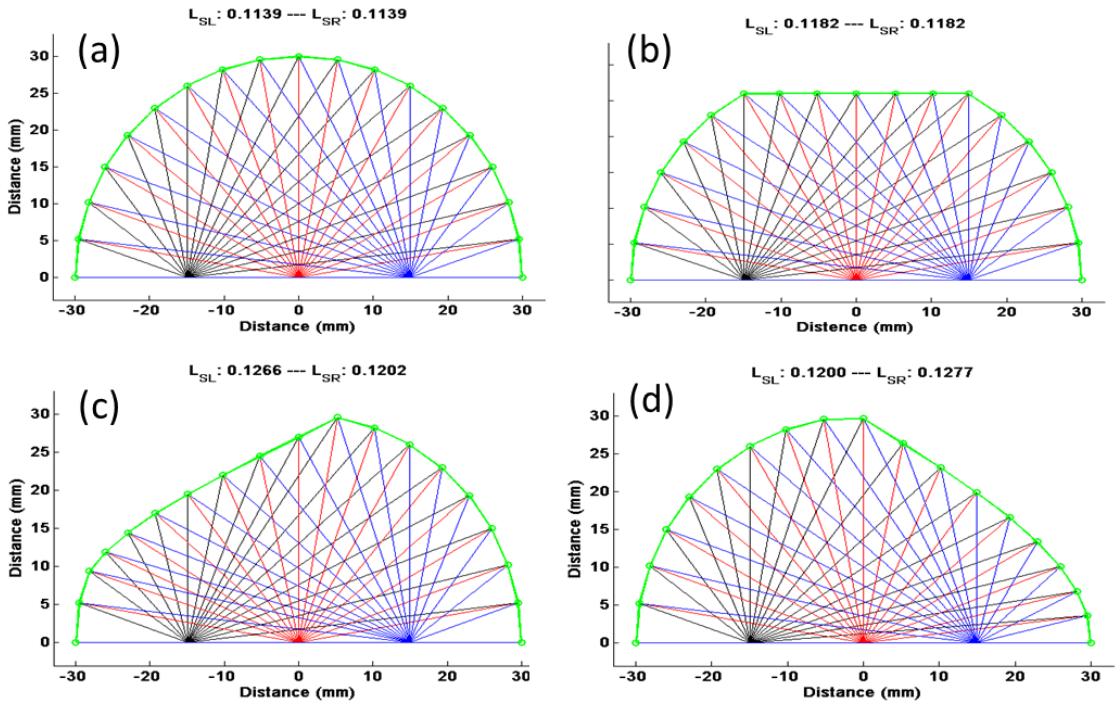

Figure 3.4: Deformation level of the semicircle at different direction of forces. On the top of each figure, the measured intensity L_{SL}, L_{SR} is shown. (a) shows the initial state without deformation where L_{SL} and L_{SR} is equal. In (b) the deformation is parallel with the x axis and both L_{SL} and L_{SR} measures the highest intensity. (c) and (d) show the deformation from left and from right where the measured light intensity is higher at the deformation side.

DOI:10.15774/PPKE.ITK.2012.003

3.4 Experimental setup

To measure the characteristic of the developed sensor, three experimental setups were made. In the first instance (Static Calibration of the Sensor), different loads were applied onto the sensor surface to measure the linearity. In the second setup (Characterization of the Sensor) the sensor output was examined at a given load at different angles. Finally (Sensor Capabilities) the noise and force measurement capabilities were tested.

3.4.1 Static calibration of the sensor

The sensor was fixed on a scale (1 g precision, maximum load 5 kg) and static load was applied on to the center point of the sensor's surface ($\sim$1 cm^2 area). The load was increased with 10 g precision from 0 g up to 4 kg and the sensor output and the appropriate scale value were recorded to the PC.

To determinate the maximal load where the sensor output saturates a household scale was used. The sensor was placed on the scale and was pressed with a plotter table z axis at a small constant speed (2 mm/s). In this way a linear increasing tendency in the applied weight can be achieved. The maximal applied load was limited to 20 kg (limitation of the plotter table).

3.4.2 Characterization of the sensor

Due to the manufacturing process, the silicone dome can have some asymmetric qualities and even a small misalignment on the PCB can lead to errors in the measurement results. In order to validate the proposed sensor force measuring capabilities at different force incidence angle an experimental setup was made (Fig. 3.5/a). The sensor was mounted on rotary joint (Fig. 3.5/b) that is capable of moving from 0° to 360° in the x axes with the precision of 0.001°. This rotary joint was mounted on the z axes of a x, y, z plotter table that is capable of moving with 10 μm precision. An Andilog precision calibration tool (Fig. 3.5/c) was used (Model ANDILOG Centor, Fr) to measure the force applied to the sensor surface. It was placed under the sensor and fixed to the ground (Fig. 3.5/d) and was equipped with a pointed tip (Fig. 3.5/e with an end diameter of 2 mm).

The calibration process is as follows:

1. The rotary joint was set to the start angel (-60°)

DOI:10.15774/PPKE.ITK.2012.003

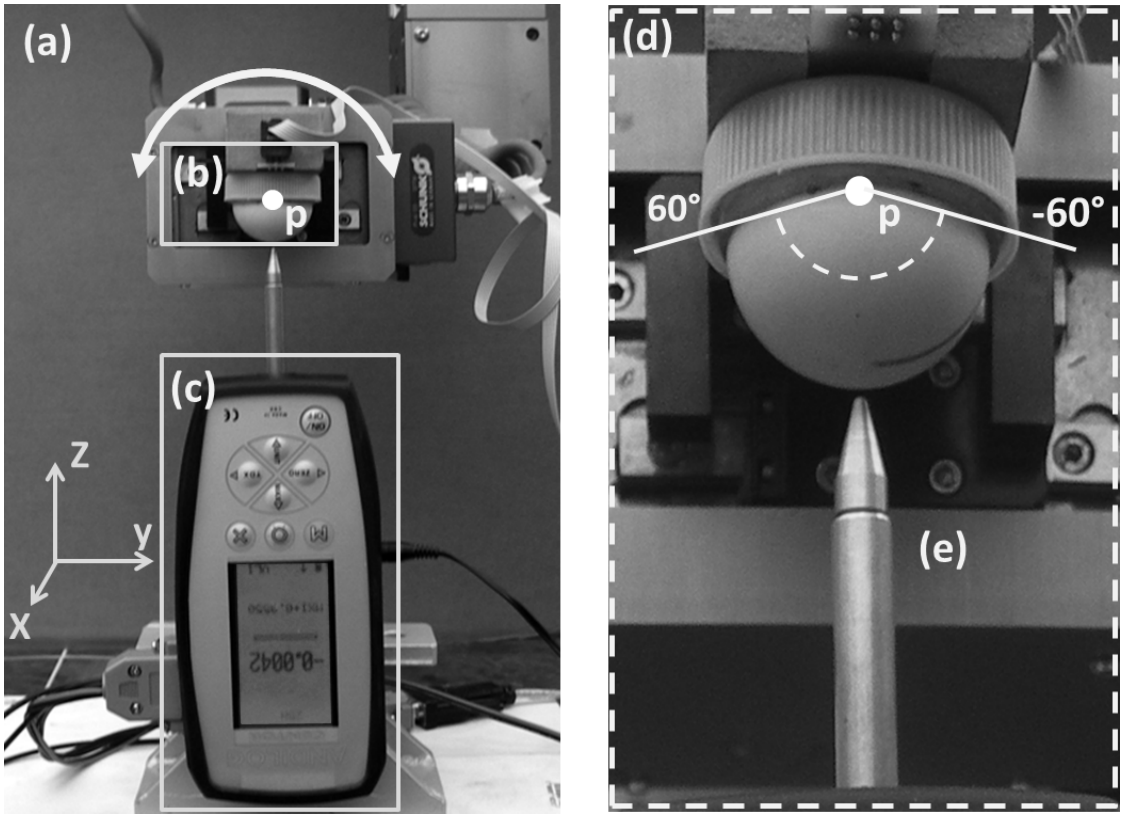

Figure 3.5: In the experimental setup the tactile sensor was placed on a rotary joint which was connected to a x, y, z plotter table (a). The sensor (b) was rotated around its middle point (p) from -60° to 60° (d). Under the sensor a calibration tool (c) was placed (Model ANDILOG Centor, Fr) to measure the force applied on the sensor surface. The sensor was moved in the z direction with 20 μm steps and its output and the Andilog output was recorded on a computer.

2. The sensor was moved closer to the Andilog with 20 μm steps in the z axis until a contact condition measured (applied force grater than 0.02N)

3. The sensor and the Andilog output saved on the computer than the distance was decreased with 20 μm steps until a threshold value reached (3N)

4. The rotary joint angle increased with five degree

5. If the joint angle was less than 60° than go back to (2)

In this way the sensor pressure profile can be measured along an axis.

DOI:10.15774/PPKE.ITK.2012.003

3.4.3 Sensor capabilities

The tactile sensor capabilities are demonstrated in four experiment regarding to different quantities:

- force directions
- noise performance
- hammer impact
- brush stroke
- pulse measurement
- relaxation time

In the first test the sensor was pressed from each side to demonstrate its capabilities to measure different force directions. Then the sensor noise performance was tested without any external force applied (3.6/a). The sensor sampling rate was set to a nominal 100 Hz. The end of a hammer (260 g and 25 cm long) was fixed to a rotational joint and was dropped on the sensor surface (3.6/b). After the test with the hammer the sensor surface was firmly stroked with a painting brush (3.6/c) to proof the wide force sensitivity. The sensor was also challenged to measure the pulse shape and the heart rate by pushing the sensor to the arteria carotis (3.6/d). In the last test, the sensor relaxation time was examined at different loads.

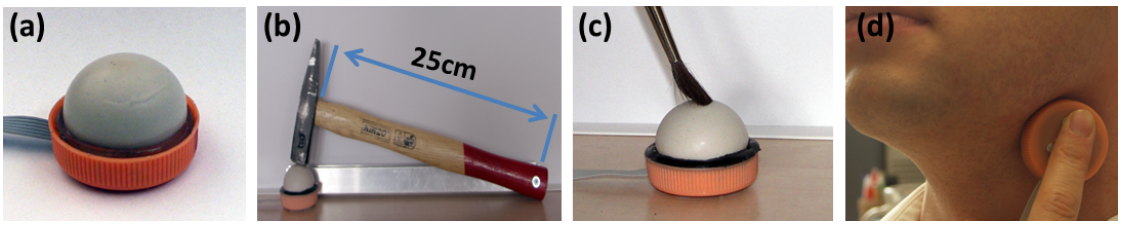

Figure 3.6: In case of experimental setup (a) the sensor was left untouched in order to obtain noise, in (b) the sensor was hit with a hammer and than was firmly stroked with a painting brush (c), in (d) the sensor was pressed to the arteria charotis to measure pulse.

DOI:10.15774/PPKE.ITK.2012.003

3.5 Signal post processing

To calibrate the tactile sensor the Andilog calibration tool output was used as reference. In case of experimental setup (Characterization of the Sensor) the measurement procedure was repeated 10 times. The maximum deviation in the load measured, both in case of the Andilog and sensor output, was around ± 10 g. The mean values of the measurements were used for calculating the error rate between the Andilog and the sensor output. These values were saved into a load Look Up Table ($\mathrm{LUT}_{load}(\alpha)$) and stored in the local memory, where α is the force incidence angle. At the next sensor readout, the appropriate value from the $\mathrm{LUT}_{load}(\alpha)$ (for the given angle) was used as a scaling factor to compensate the sensor output. To calculate the force incidence angle in the x direction the following equations can be used:

$$\alpha = \arctan(x_2/x_3) \tag{3.11}$$

where x_i is distance based on the S_i-th sensor output.

To calculate the force incidence angle (α) the x_1, x_2, x_3 values are needed thus the definition is recursive, but an iteration process can be used. Using the measured force vectors, the force incidence angle can be approximated with Eq. 3.11. The $\mathrm{LUT}_{load}(\alpha)$ value can be used on the force vectors to correct the approximated α. With this approximated α the force vector can be corrected thus a more accurate α can be calculated.

Another method for calculating the force incidence angle is to characterize the error of the force incidence angle measurement and save into a $\mathrm{LUT}_{angle}(\alpha')$.

The calibrated sensor output was constructed in three steps:

1. Based on the sensor raw output (S_1, S_2, S_2) approximation for (x_1, x_2, x_2) was made and α (α') was calculated
2. The $\mathrm{LUT}_{angle}(\alpha')$ was used to correct the approximation for α
3. The x_1, x_2, x_2 values were corrected with the $\mathrm{LUT}_{load}(\alpha)$ value

DOI:10.15774/PPKE.ITK.2012.003

3.6 Experimental results

3.6.1 Static calibration of the sensor

At the 4 kg load, the sensor surface deformation was ∼6 mm. This would indicate a deformation of approximately 2.2 μ at 1 g. The correlation between the sensor output and the applied load can be examined in Fig. 3.7. The sensor output (mean value of the photodiodes) was highly linear with an average deviation of ±35 g and with the maximum difference of 80 g (2 %).

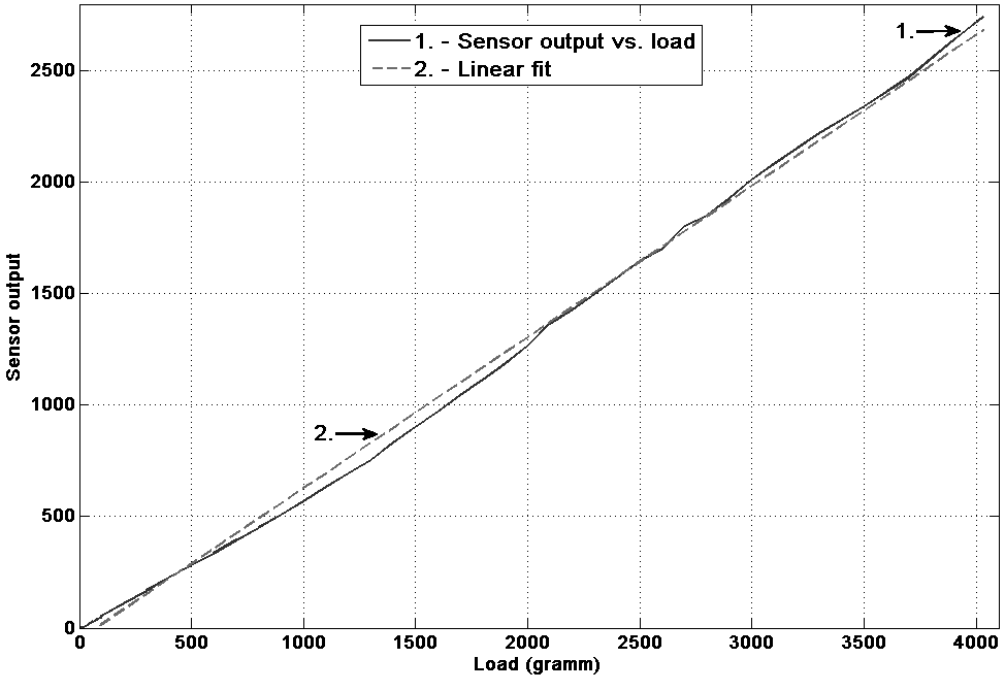

Figure 3.7: Static load response of the tactile sensor. The solid line shows the sensor output as different weights were placed on the tactile sensor surface from 0 g to 4 kg in 10 g incrementation steps. The dashed line shows a linear fit on the sensor output.

To determinate the maximal load where the sensor output saturates an experimental setup Fig. 3.8/b was made. Because of the limitation of the plotter table, the maximal measured weight was around 20 kg, by further increasing the applied weight by stepping on the sensor its output saturated at around 23 kg.

As it can be seen in Fig. 3.8/a in the higher load range the sensor output shows nonlinear characteristic versus the linear interpolation value of the applied load. The high load capacity makes the sensor ideal to use not just in the robotic hand but also in the feet of a bipedal robot to measure the force distribution or in mobile

DOI:10.15774/PPKE.ITK.2012.003

robotic as analog bumpers, etc.

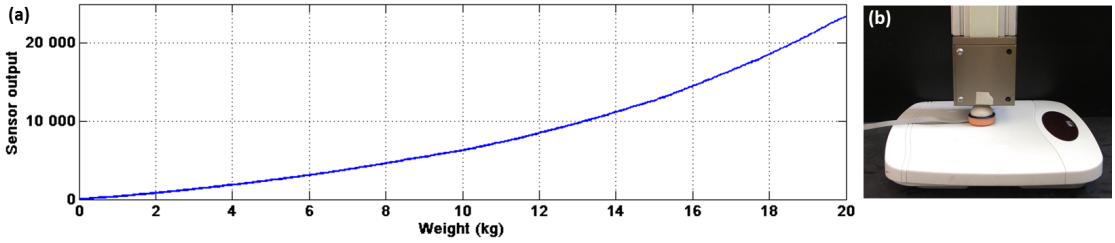

Figure 3.8: Maximal load measurement. (b) shows the experimental setup, where the sensor was placed on a household scale and was pressed with the z axis of the plotter table. The maximal applied load was increased in 6 s from 0 to around 20 kg a linear interpolation of the measured weight versus the sensor output can be seen in (a).

3.6.2 Characterization of the sensor

The sensor load characteristic was measured at every angle as explained in section IV. The threshold load was set to 2 g and the maximal applied load was 300 g. The measurement started at -60° to 60° with the incremental steps of 5°. During the measurement process the distance between the sensor surface and the Andilog was set in 20 μm steps. The Andilog and the sensor output were saved at every iteration. Because the controlled parameter in the measurement was the position (distance) of the sensor over shoots at the stop condition occur (due to the incremental steps). The values which were closer to the stop condition were used as the reference load. The Andilog output and the sensor output value at every rotation angle can be seen in Fig. 3.9.

The sensor output was non-linear in the angle range and the non-symmetrical to the 0°. The non-linearity was caused by that the light distribution was not homogeneous in the dome due to the small angle of half intensity (±10°) of the infrared LED used. The non-symmetricity of the characteristic was due to the misaligned and asymmetric dome.

3.6.3 Measuring the force incidence angle

To calibrate the tactile sensor output the force incidence angle has to be known in order to use the appropriate ($\mathrm{LUT}_{load}(\alpha)$) correction value. In the measurement setup (Fig. 3.5/a) as the sensor was rotated around its middle point the force

DOI:10.15774/PPKE.ITK.2012.003

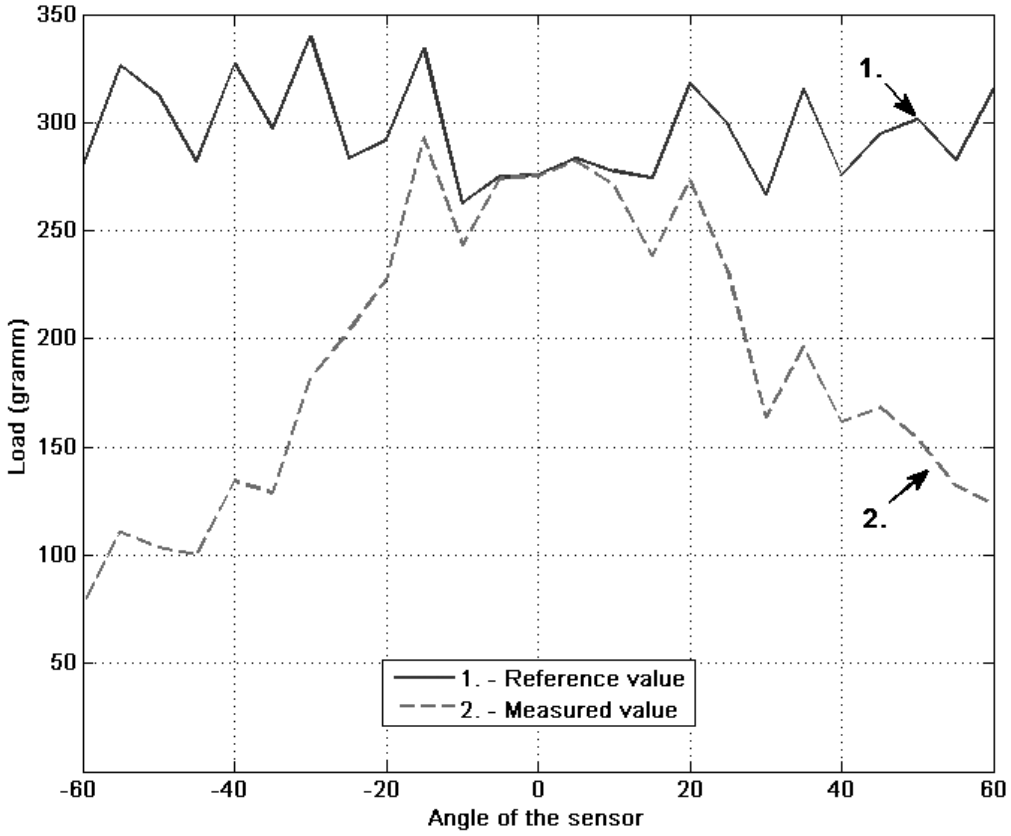

Figure 3.9: The Andilog reference value at different sensor rotation angle and the measured sensor output value can be seen. The sensor output was non-linear in the angle range and the non-symmetricity to the 0° was caused by the non symmetric and misaligned dome.

incidence angle equals to the sensor rotation angle. The calculated force incidence angle using Eq. 3.11 and the sensor angle (based on the encoder of the rotation joint) can be seen in Fig. 3.10 where the error is saved into the $\mathrm{LUT}_{angle}(\alpha)$.

3.6.4 Calibrated sensor output

The calibrated sensor output can be seen in Fig. 3.11 at different loads (100 g, 200 g, 300 g). As the Static Calibration of the Sensor experiment showed, the sensor characteristic was close to linear in the load range, thus the error rate values stored in $\mathrm{LUT}_{load}(\alpha)$ was obtained at a given load at a given force incidence angle of α. After the calibration steps the sensor and the Andilog output has an average error rate of 5 g and the maximum deviation of 25 g.

DOI:10.15774/PPKE.ITK.2012.003

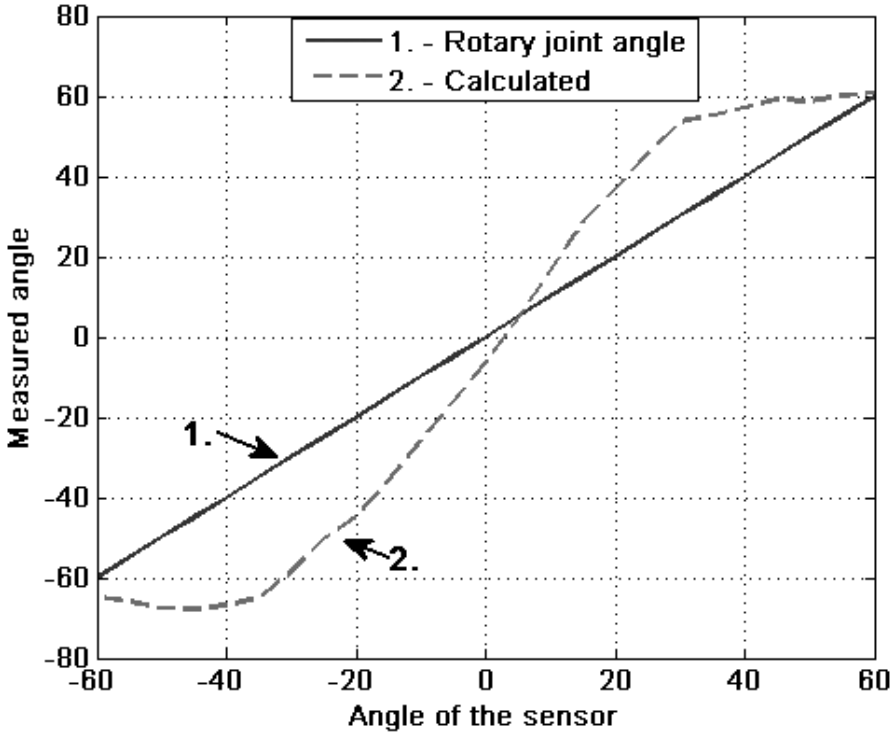

Figure 3.10: The real and the calculated force incidence angle (α) using Eq. 3.11. As in the measurement the sensor was rotated around its middle point the force incidence angle was equal to the angle measured by the encoder in the rotary joint.

3.7 Sensor capabilities

3.7.1 Force directions

As force was applied on the sensor surface from four different directions the force vector changed accordingly as it can be seen in Fig. 3.12, thus during the force measurement the x, y, z force components showed independent behavior.

3.7.2 Noise performance

The sensor was left (untouched) on the table, and the (offset compensated) output was measured. Each sensing element (photodiode) output can be seen in Fig. 3.13. The sensor noise was around $\pm$ 3 LSB (Least Significant Bit) where the overall range is 16 bits $\rightarrow$ 65536 LSB meaning a 1/10000 % error in the measurement.

DOI:10.15774/PPKE.ITK.2012.003

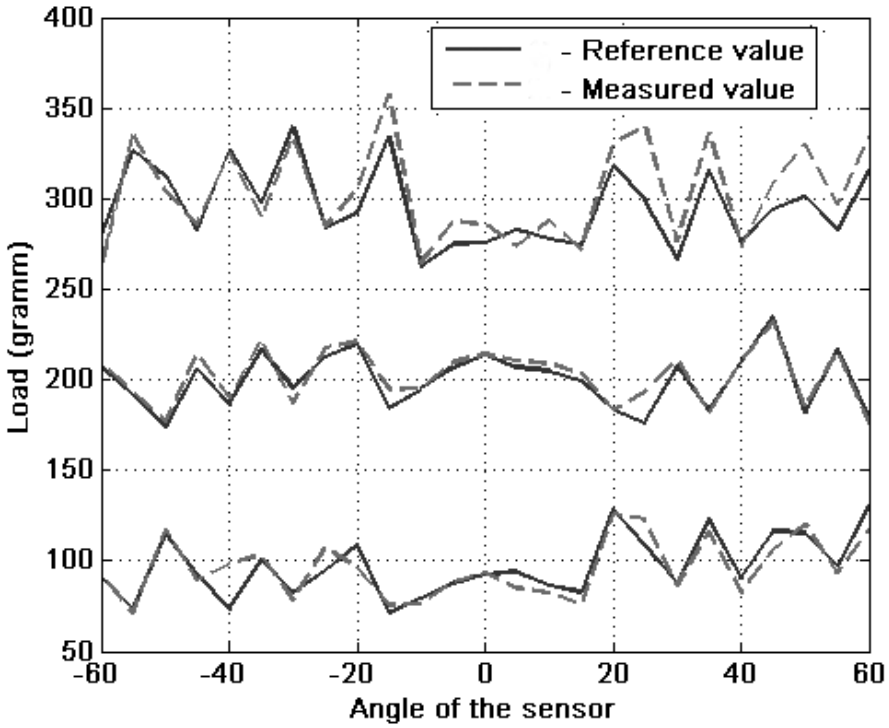

Figure 3.11: The solid line shows the reference load, measured by the Andilog, and the dashed line shows the calibrated sensor output at different load and rotation angle. After the calibration steps the average error was 5 g and the maximum deviation was 25 g.

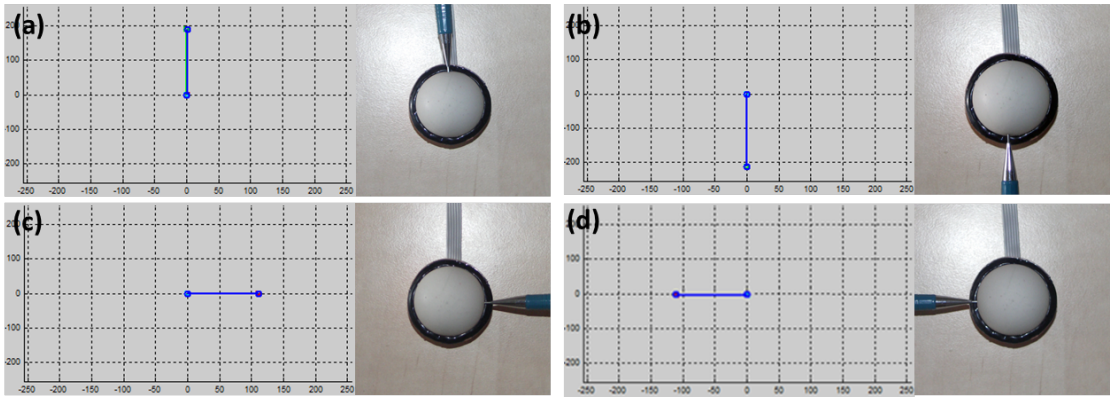

Figure 3.12: Force was applied an the sensor surface from four directions ((a)-north, (b)-south, (c)-west, (d)-east) and the measured force vectors can be seen accordingly

3.7.3 Hammer impact

The sensor surface was hit with a hammer (260 g and 25 cm long). The high impacts ($\sim$50 N) and its damped oscillation can be seen in Fig. 3.13. This experiment

DOI:10.15774/PPKE.ITK.2012.003

demonstrates that the sensor output can follow even the gradient of a high impact and settles fast enough to detect the next impact. The output after the oscillation did not returned to the zero level as the the hammer was resting on the surface thus the sensor was measuring the hammer weight.

3.7.4 Brush stroke

After the test with the hammer, the sensor surface was firmly stroked (∼0.03 N) with a painting brush, the output of each sensing element can be seen in Fig. 3.13, this test demonstrates the wide force sensitivity of the proposed sensor.

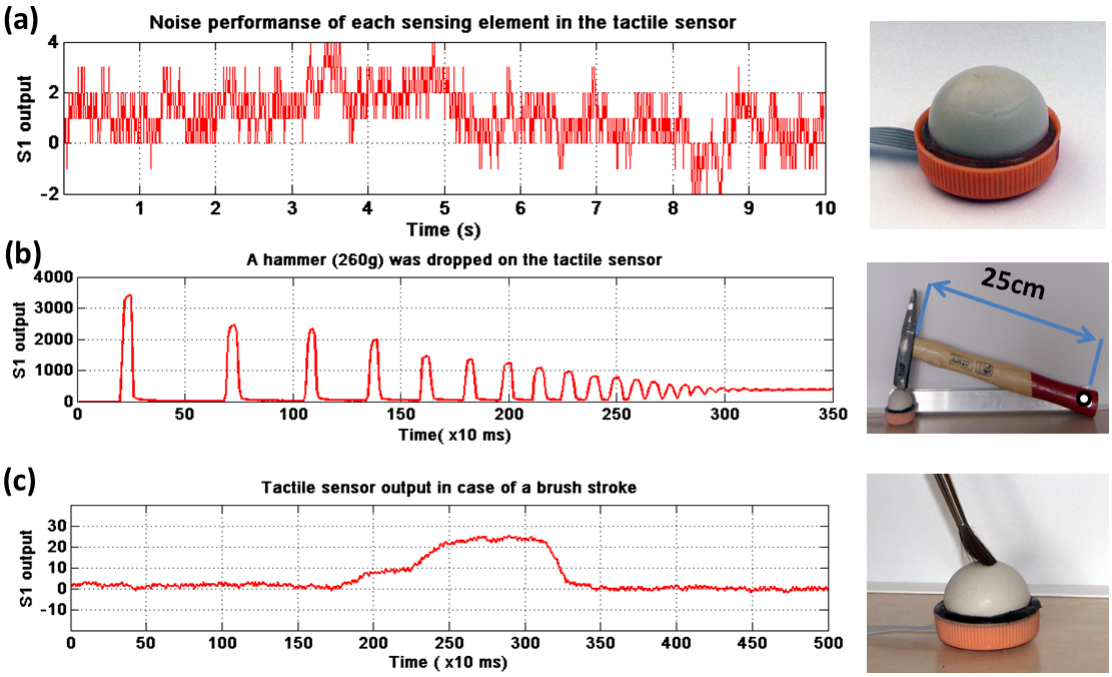

Figure 3.13: (a) the sensor noise performance, (b) impact measurement of a hammer, (c) firmly stroked by a painting brush

3.7.5 Pulse measurement

In this test, the sensor was pushed to the arteria carotis external on the neck. From the measurement output the shape of the pulse can be seen in Fig. 3.14. The heart rate could be calculated by using a peak detection on the derivated signal (Fig. 3.14/ $(dS3)/dt$). Here I would like to note that as the sensor was handhold some disturbance in the measurement can be obtained, but the typical characteristic of the pulse shape can be well recognized.

DOI:10.15774/PPKE.ITK.2012.003

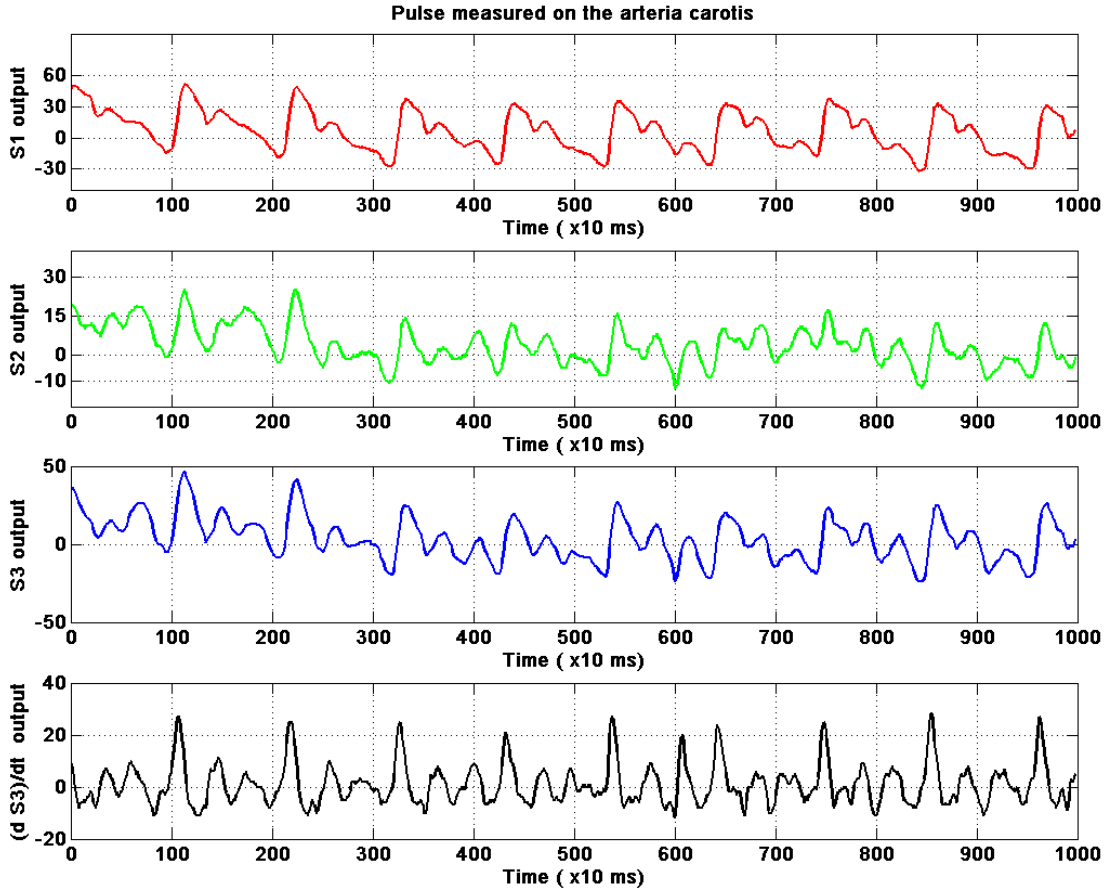

Figure 3.14: Measuring the pulse shape and the heart rate on the arteria carotis external, where each sensor output (S1,S2,S3) and the derivation of the S3 signal is presented.

3.7.6 Relaxation time

Due to the viscoelastic property of the used silicone rubber a load dependent relaxation can be observed. Different loads (194 g, 873 g, 1405 g) were placed on the top of the sensor (Fig. 3.15). After the output settled, the load was suddenly removed, and the output was recorded in order to measure relaxation time (Fig. 3.16).

This viscoelastic property can be improved by using better silicone rubber or by modelling this effect.

DOI:10.15774/PPKE.ITK.2012.003

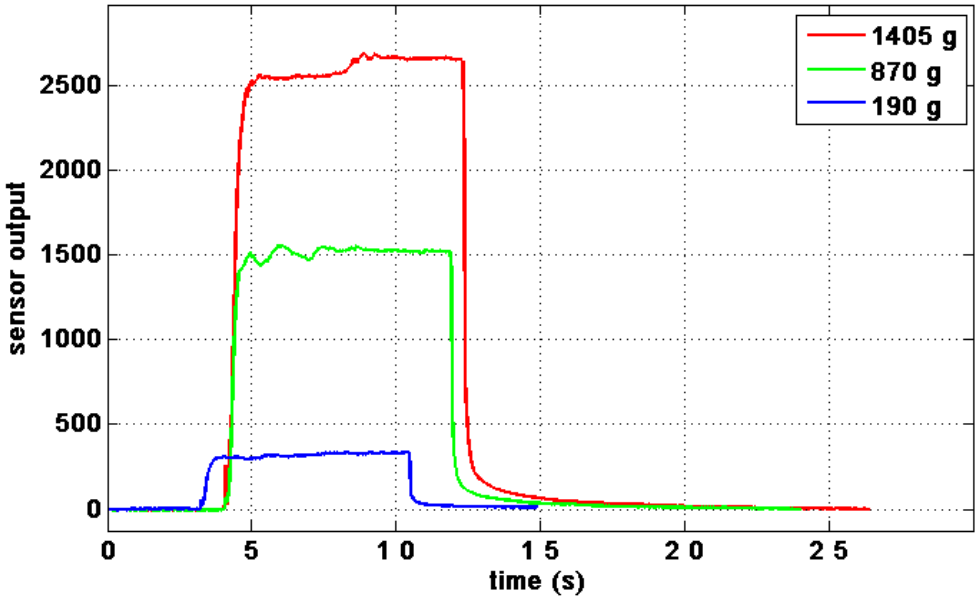

Figure 3.15: Measurement of the realaxation characteristic at different load levels. It can be seen as the load level increases the relaxation time also increases.

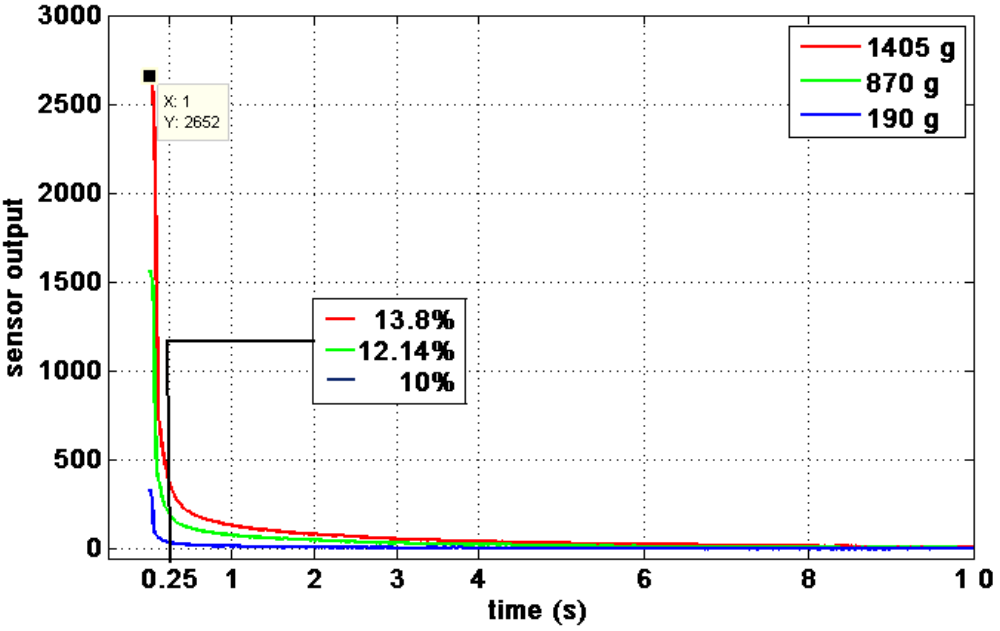

Figure 3.16: Relaxation characterictic after the load was removed. At 0.25 s all signal value dropped at least 86% and after a certain time returned to zero.

DOI:10.15774/PPKE.ITK.2012.003

3.8 Layered structure of the elastic cover

In the first sensor prototype a light green colored $Triszil\ RTV-2$ type silicone rubber was used. Even though the silicone cover thickness was around 1 cm (inner dome diameter 1.5 cm) the infra light component of the daylight caused some disturbance in the measurement.

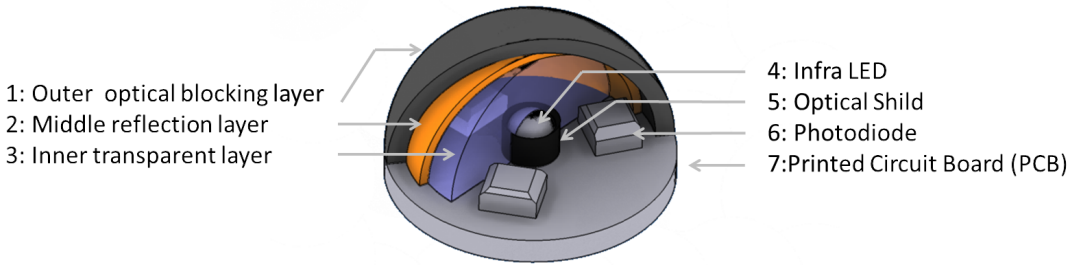

Figure 3.17: The three layered sensor structure. Where the "Outer optical blocking layer" (1) filters the ambient light, the "Middle reflective layer" (2) reflects the infra light rays to the photodiodes and the "Inner transparent layer" (3) increases the sensor structural stiffness.

Thus a better cover was needed to be designed. The new version has a three layered structure (3.17) where each layer has its own well defined purposes:

1. **Outer optical blocking layer:** To increase the noise free resolution of the sensor extra attention has to be made to prevent the outer light getting into the photodiodes. One way of the elimination is to make an extra measurement without infra light emission thus the ambient light can be compensated. As a back draw this would result in a 1/2 reduction in the speed performance. The thickness of the cover could be increased but the size of the sensor would be also increased. Another way is to use a colored silicone rubber (e.g: black) that blocks the incoming light rays 3.17/1. The layer thickness is defined by the used material light absorbance properties.

2. **Middle reflective layer:** As the outer colored layer blocks the incoming light it also blocks the inner infra light rays. So an additional thin layer is required which reflects the infra light rays to the photodiodes. This layer (3.17/2) should be diffuse and highly reflective (e.g: white).

3. **Inner transparent layer** A hallow inner structure during deformation forces the air to be compressed in the cavity, or as it is hard to perfectly

DOI:10.15774/PPKE.ITK.2012.003

seal after the force released a vacuum effect would be created thus the relaxation of the covering material is increased. To fill the cavity with an optically fully transparent silicone (3.17/3) would solve this problem. Furthermore, a filled cover is harder to compress thus to achieve the same measurable force range a smaller sensor could be constructed. If the optical layer transparent material and the photodiode cover material is different (has different scattering factor) after the molding process a lens may be formed so as a plus feature it may also increase the sensibility.

Over time (months) the silicone rubber's elastic properties will slightly change (the silicone will be hardened), depending on the used temperature, applied force and force duration. Such a wear out parameter is hard to predict so a periodic calibration test (with e.g. 100g) is recommended to obtain the wear out level.

As design considerations the used materials should meet some specific need:

- the surface material should be smooth, prone to contact and no sticking
- homogeneous and isotropic structure
- durable, low wear out, robust and no permanent deformation caused by stretching
- fast settling time after force released and minimal viscoelastic effect
- no temperature dependence (or at least not significant in the measurement range)
- must have high adherence to the sensor board

DOI:10.15774/PPKE.ITK.2012.003

3.9 Sensor prototyping

In order to create a robust and reliable sensor a moulding procedure was carried out. On the sensor board 5 *mm* sized square shaped photodiodes and a 3 *mm* diameter infra LED were used (3.18/c). The 3D design of the moulding form can be seen in 3.18/a, it has two parts the bottom where the silicone is poured and the top which keeps the sensor in place (3.18/b).
The moulding process starts with the innermost layer. The transparent silicone is poured into the form (3.18/e) and with the top part with the sensor board inside (3.18/b) it is squeezed together with a clap (3.18/n). The result can be seen in 3.18/f and the inner layer detailed mechanical properties in (3.18(d)). During the inner layer moulding bobbles can appear thus special attention must be made to avoid it, as it would dissolve the light beams.
The next step is similar but the moulding form is slightly larger (3.18/g) and filled with the reflective silicone, in this case it is light green. Like the previous part (3.18/f) it is squeezed into the moulding form where the reflective silicone evenly dissolves on the surface forming the reflective layer (3.18/i).
After creating the final optical blocking layer the sensor has its final look (3.18/(l,o)). To ensure that light does not go through the bottom of the sensor it is also covered with a 1 *mm* thick silicone layer (3.18/m).

These moulding forms were made by 3D rapid prototyping using ABS plastic building up from 32 μm thick layers and were designed in a CAD software called Autodesk Inventor.

DOI:10.15774/PPKE.ITK.2012.003

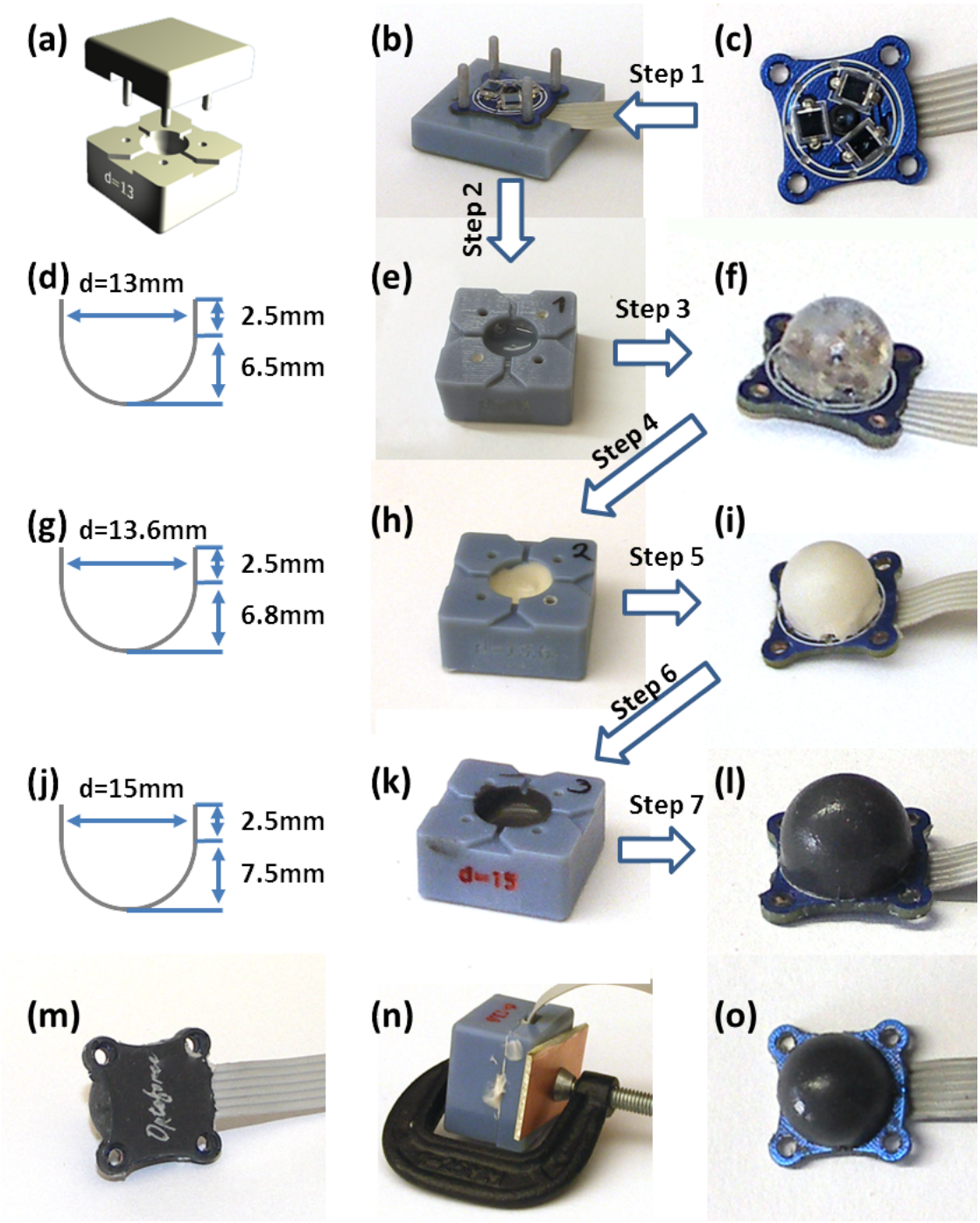

Figure 3.18: The moulding process of the elastic cover. (a) shows the moulding form 3D design, (b) is the top form that keeps the sensor board (c) in place. Each layer has its separate moulding form (e - inner transparent layer, h -middle reflective layer, k - outer optical blocking layer) with different mechanical properties (d,g,j). Each moulding step output is shown in (f,i,l). In the final step a 1 *mm* thick silicone layer is added to the sensor board bottom to prevent the incoming light.

DOI:10.15774/PPKE.ITK.2012.003

3.10 Conclusion

In this chapter a novel three photodiode, one infrared LED and an elastic hollow dome based low-cost, compliant, light weight and durable 3D tactile sensor was presented. The sensor size and measurement range can be easily varied based on the application requirements. Also new layer structured cover has been presented, wherewith the sensor noise and size can be decreased.

The results of the verification experiments indicate that the sensor can measure the triaxial force components.

In the static load test different weights were placed on the sensor surface form 0 g up to 4 kg in 10 g incremental steps where the output of the sensor showed close to linear behavior, but at higher weight levels (up to 20 kg) it is non-linear. Furthermore, the sensor showed high force dynamic range from measuring a pulse shape up to an impact of a hammer. A precise calibration tool (Model ANDILOG Centor, Fr) was used to measure reference loads. The sensor was mounted onto a rotational joint in order to measure the sensor pressure profile at different force incidence angle. The sensor output showed non-linear behavior in the force incidence angle range because of the used infra LED illumination characteristic.

After the calibration process, the sensor has an average error rate of 5 g and the maximum deviation of 25 g at different load measurement in case of small loads.

As conclusion the following thesis points can be stated:

Thesis II.:

Design of a low cost 3D optical compliant tactile sensor that is capable of measuring three-axial directional force components and the location of the contact point.

A: I have designed a robust layered structured elastic cover which supports the realization of small sized sensors (<1cm).

B: I have designed a calibration process to measure the sensor characteristics. I have shown a method to measure the location point position on the sensor surface.

Published in: [5], [4]

DOI:10.15774/PPKE.ITK.2012.003

Chapter 4

Studying Synchronization Phenomenon in Oscillatory and Chaotic Networks

4.1 Introduction

Chaos theory describes the behavior of certain dynamical systems that may exhibit dynamics that are highly sensitive to initial conditions. Small variations of the initial condition of a dynamical system may produce large variations in the long term behavior of the system. As a result of this sensitivity, which manifests itself as an exponential growth of perturbations in the initial conditions, the behavior of chaotic systems appears to be random. This happens even though these systems are deterministic, meaning that their future dynamics are fully defined by their initial conditions, with no random elements involved. This behavior is known as deterministic chaos, or simply chaos.

Chaotic systems are well-known for strange patterns in their phase space, which has always attracted the research community [20, 21]. More bizarre is the behavior when two chaotic systems are connected together in a specified fashion [62].

Synchronization of oscillator networks is a prevalent phenomenon in nature [19]. Despite its widespread presence, synchronization is used only in a few specific fields of engineering, e.g. communication with chaotic lasers [63, 64]. Two or more interconnected chaotic systems have also been shown to produce effects like synchronization, pattern generation or hyperchaos [65, 66].

DOI:10.15774/PPKE.ITK.2012.003

Many extensive studies have been performed in understanding the underlying behavior of several interconnected chaotic systems [67, 68, 69]. One interesting case study is to understand the behavior of interconnected chaotic systems connected to their nearest neighbors dictated by the architecture of a regular autonomous Cellular Nonlinear Network. Thus an interesting case study may include chaotic circuits interconnected with each other in one, two or three dimensions [70].

However, so far most of these studies are restricted to either development of mathematical concepts or software-based studies. One reason that can be attributed to the lack of hardware results lies in the non-availability of a robust chaotic circuit.

The aim was to designe a 3-dimensional CNN architecture based test bed with neighbors interconnected to each other by a programmable digital resistor [6]. This makes it a special case of generalized CNN (defined in [71, 72, 73]) as a programmable resistive grid based CNN. Even though each cell can be an independent circuit (discussed later), chaotic Chua's circuit [74] were the CNN cells.

4.2 Chua's circuit

As a CNN cell we used a simple electronic circuit developed by Leon Chua [75, 76]. The reason for this is in the easy experimental implementation and the highly robust quality of the circuit.

Since it only consists of four linear elements (two grounded capacitors, one grounded inductor and one linear resistor), and one non-linear resistor it makes the electronic realization very simple. The system is described by the following set of differential equations:

$$C_1 \frac{dv_1}{dt} = G(v_2 - v_1) - f(v_1) \tag{4.1}$$

$$C_2 \frac{dv_2}{dt} = G(v_1 - v_2) + i_3 \tag{4.2}$$

$$L \frac{di_3}{dt} = -v_2 \tag{4.3}$$

DOI:10.15774/PPKE.ITK.2012.003

Where v_1, v_2 and i_3 denote the voltage across capacitor C_1, voltage across C_2 and current across inductor L, respectively and

$$i_R = f(v_R) = G_b v_R + 0.5(G_a - G_b)(|v_R + B_p| - |v_R - B_p|) \tag{4.4}$$

denotes a 3 segment odd- symmetric voltage current characteristics of a non-linear resistor, also called *Chua's diode*. Here G_a and G_b are the slopes of the segments and B_p denotes the breakpoint as it is shown on Fig. 4.1.

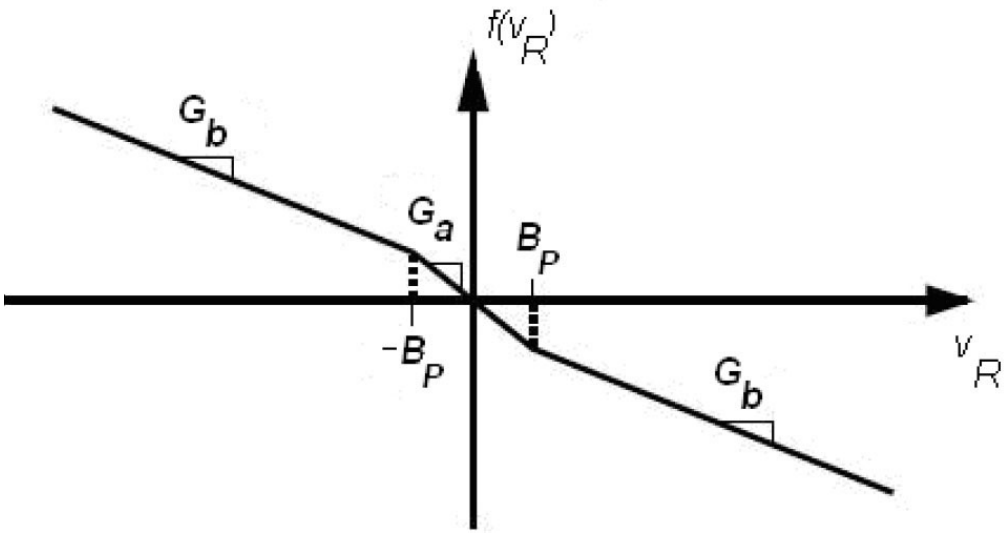

Figure 4.1: Current vs. voltage characteristics of the Chua's diode

Fig. 4.2 shows the circuit diagram of the *Chua's circuit*, which is an autonomous dynamical system i.e. even in the absence of any external input the system evolves through its natural dynamics.

By substituting

$$x = \frac{v_1}{B_p}, y = \frac{v_2}{B_p}, z = i_3(\frac{R}{B_p}) \tag{4.5}$$

$$\alpha = \frac{C_2}{C_1} \tag{4.6}$$

$$\beta = \frac{R^2 C_2}{L} \tag{4.7}$$

$$k = sgn(RC_2) \tag{4.8}$$

$$a = RG_a, b = RG_b \tag{4.9}$$

DOI:10.15774/PPKE.ITK.2012.003

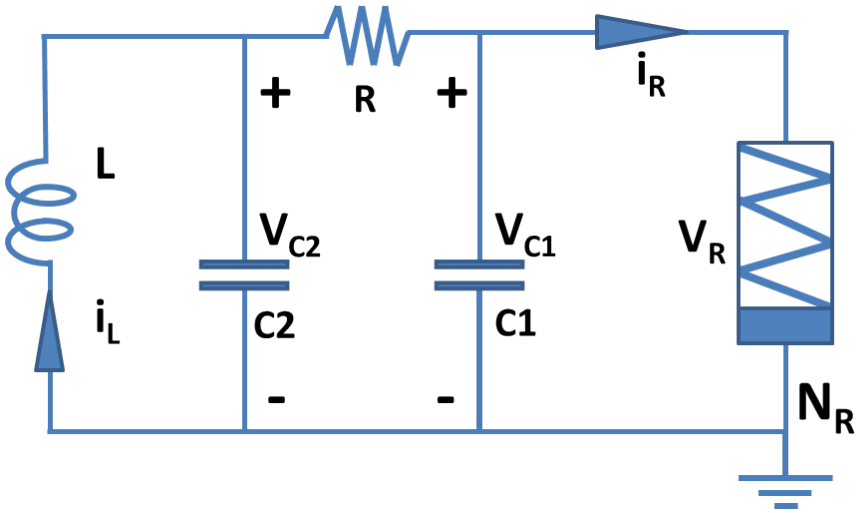

Figure 4.2: Chua's Circuit Schematic

$$\tau = \frac{t}{|RC_2|}) \tag{4.10}$$

$$G_k = \frac{1}{R_k} \tag{4.11}$$

the equations in dimensionless form can be written as

$$\frac{dx}{d\tau} = k\alpha(y - x - f(x)) \tag{4.12}$$

$$\frac{dy}{d\tau} = k(x - y + z) \tag{4.13}$$

$$\frac{dz}{d\tau} = -k\beta y \tag{4.14}$$

$$f(x) = bx + 0.5(a - b)(|x + 1| - |x - 1|) \tag{4.15}$$

Here $sgn(x)$ is a standard sign function [77]. Parameter k, which can take value 1 or -1, specifies the direction of *Chua's circuit* dynamics.

These equations, also called *Chua's equations*, can be studied either through computer simulation [78] or by different physical electronic implementations [79], [80].

DOI:10.15774/PPKE.ITK.2012.003

4.3 Chua's circuit kit

As a realization of the Chua's chaotic circuit an easy to use and compact kit was built , [74]. This kit also can help amateurs in building Chua's circuit in a few minutes and can observe chaotic behavior on their personal computer through the sound card line in port. Being highly robust, this kit was used as a cell for the CNN grid.

The kit provides four different outputs from the Chua's circuit as shown in Fig. 4.3. Here output A and B correspond to the non-grounded node of the two capacitors of Chua's circuit while MA and MB correspond to its buffered value. These four different nodes henceforth referred as A, B, MA and MB respectively are used as the node for connecting the Chua's circuit as a cell to the CNN grid. It is the inherent architecture of both the kit as well as the grid that helps in studying simple as well as master-slave topologies of interconnected Chua's circuits.

The image of the assembled Chua's kit is shown in Fig. 4.3 and the second version where the amplifiers are hidden Fig. 4.4. The values of the few components used in the kit are as follows: C1 = 100 nF, C2 = 10 nF, R1 = 2.2KΩ, R2 = 220Ω, R3 = 220Ω, R4 = 3.3KΩ, R5 = 22KΩ, R6 = 22KΩ and the inductor is 18 mH. The exact values are also indicated on the PCB board, and connections are made to be plug-and-play thus the component can be easily changed to explore different behavior.

4.4 Chua's circuit grid - general architecture

The designed architecture is aimed for experimental purposes, so efforts were made to ensure maximal flexibility in the design of the topologies and the joining of the elements. Topologies are not strictly bound, in a given $n \times n \times n$ 3D matrix, the elements can be coupled to each other by the rule of 4-neighborhood (i.e. North, South, East and West). The architecture allows the possibility to disconnect the coupling between cells as well, thereby providing the flexibility to explore several architectures of interconnected chaotic Chua's circuits. The design can be treated as a 5 neighborhood anisotropic CNN with autonomous cells. The current designed system supports a $4 \times 4 \times n$ size 3D matrix.

DOI:10.15774/PPKE.ITK.2012.003

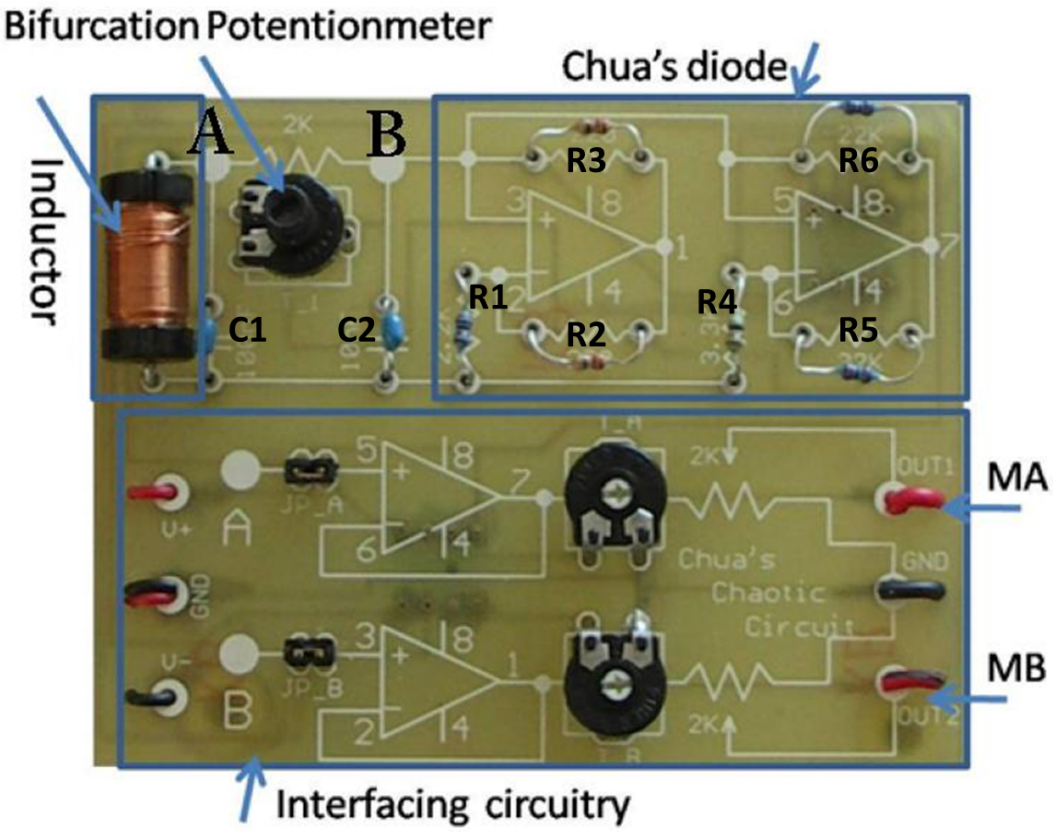

Figure 4.3: Snapshot of the kit [74]. Between the inductor and Chua's diode we can find the bifurcation variable resistor. The components values are as follows: C1 = 100 nF, C2 = 10 nF, R1 = 2.2KΩ, R2 = 220Ω, R3 = 220Ω, R4 = 3.3KΩ, R5 = 22KΩ, R6 = 22KΩ and the inductor is 18 mH. The bottom part contains the interface circuitry. Outputs: A, B, MA, MB are marked on the panel.

Variable resistors were used as the coupling between the neighboring cells. Note that since it is a generalized architecture, the hardware is prepared to plug any capacitive or inductive coupling or a combination of any two-port passive components easily. However, that is the task for an extended study.

The core scheme for the entire system can be divided in the following different modules:

- Interconnecting Interface: Building a plug-and-play standalone robust Chua's circuit with an analog variable resistor (acting as a bifurcation parameter). This Chua's circuit gives two pairs of different yet similar outputs namely A,B and their buffered versions MA and MB.

DOI:10.15774/PPKE.ITK.2012.003

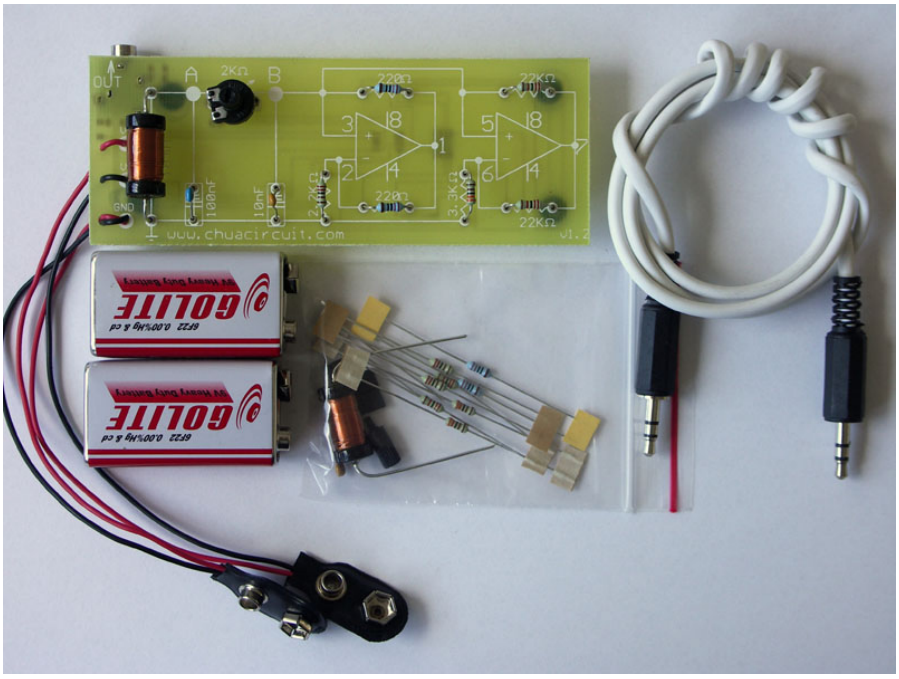

Figure 4.4: Snapshot of the second version of the Chua kit with the additional components in a bag, extension cable for connecting the kit to the PC sound card Line-in port and the two 9V batteries.

- Programmable Logic: An interface circuitry to choose one output from the four of the Chua's circuit designed in the previous step. This chosen node will then be connected to another Chua's circuit through a coupling resistor.

- Coupling Grid: Here the different coupling components are placed and can be selected for connection via an appropriate program. As explained, in the current experiment the coupling component is a programmable/tunable resistor, though it can be any other two-port passive component.

4.5 Architecture implementation

4.5.1 Interconnecting interface

Since the above designed kit is a standalone kit for Chua's circuit study and the current aim is to understand coupled Chua's circuits, an interconnecting interface was designed which helps in achieving common power supply to all connected Chua's circuits at the same time transferring all four outputs of the Chua's circuit to the coupling grid through a single bus.

DOI:10.15774/PPKE.ITK.2012.003

Fig. 4.5 shows the interconnecting interface connected to Chua's circuit kit to make it suitable for autonomous 3D-CNN.

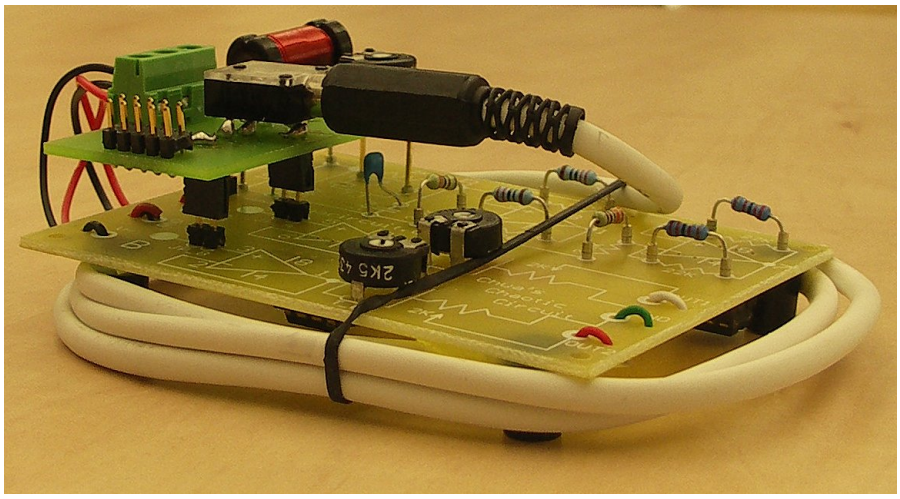

Figure 4.5: The board, as the tally of the Chua's panel is joined with the help of needles to the developed connectors of the Chua's kit.

4.5.2 Programmable logic

The designed kit acts as a single cell to the core CNN architecture. However, since there are four different possible channel outputs from the Chua's circuit, an interface circuitry is required to select the desired channel. This task is achieved by efficient usage of analog multiplexers.

A dedicated programmable logic is developed for selecting different signals from different Chua's circuits to be coupled to each other. This is done to achieve maximum flexibility in exploring different possible architectures of interconnecting Chua's circuits.

The general architecture for connecting several such layers having a similar programmable logic is as shown in Fig. 4.6. Herein each MUX receives 4 different signals (A, B, MA and MB) from a respective Chua's circuit design and select one out of them to be put on the general bus as one of the signal to be interconnected. The output (in the present case of 4×4 so the maximum of 16 independent oscillatiors) is then transferred to a coupling grid, which performs different possible desired couplings between different cells.

DOI:10.15774/PPKE.ITK.2012.003

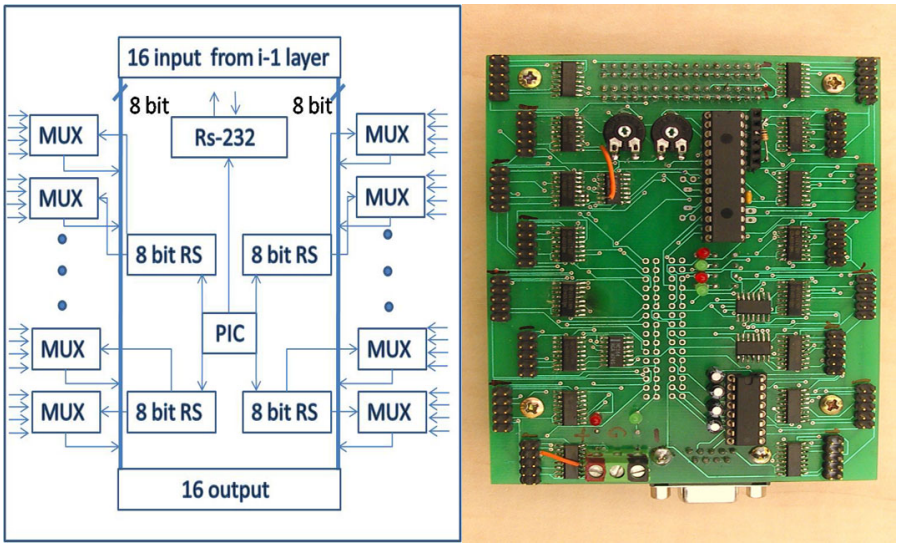

Figure 4.6: On the left, the general architecture for Programmable Logic can be seen. Herein each MUX receives 4 different signals (A, B, MA and MB) from the respective Chua's circuit design and selects one out of them to be put on the general bus as one of the signals to be interconnected. The output (in present case of 4×4) is then transferred to a coupling grid, which performs different possible desired couplings between different cells. On the right is a snapshot of the programmable logic board.

4.5.3 Coupling grid

The output from the connection matrix board is then fed to the coupling grid that has the possibility to manually add different passive two-port coupling components to the design. This provides an interesting opportunity for testing several cases with different coupling components between different cells of 3D-CNN. These components can be different not only in their component values but also their type, thereby making it suitable for studying different test cases. Fig. 4.7 shows one such coupling grid with few interconnected variable resistors. A programmable logic along with a coupling grid constitutes a single layer of autonomous CNN.

4.6 Experimental results

Several experiments with different architectural topologies were performed. One of the prime tasks was to observe and study the behavior of the coupled chaotic system at the edge of synchronization to de-synchronization. The cells are connected

DOI:10.15774/PPKE.ITK.2012.003

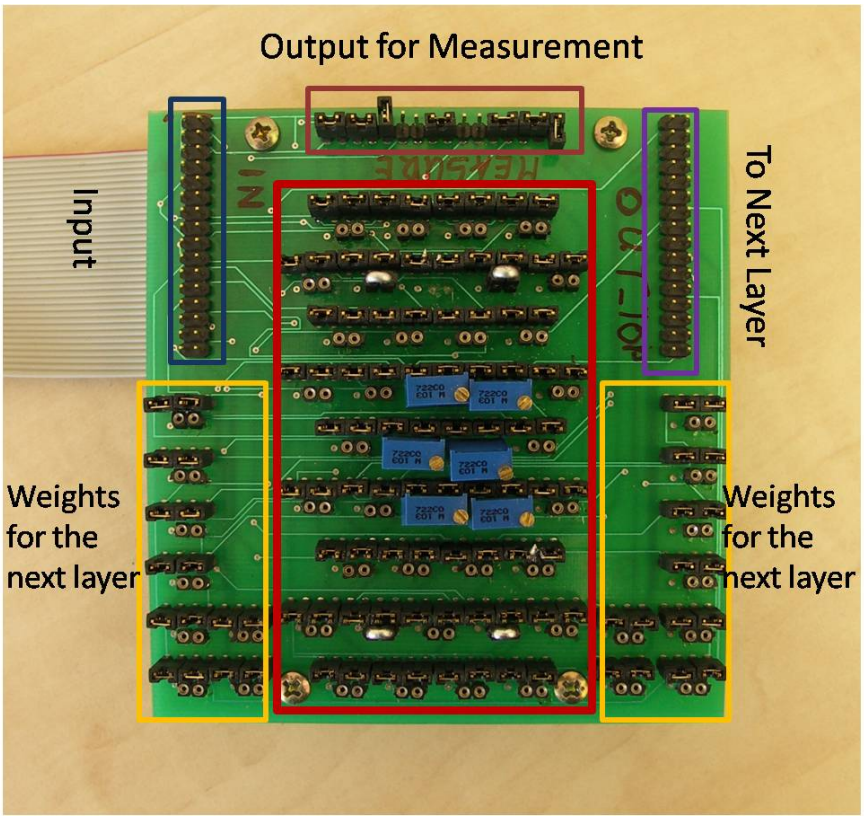

Figure 4.7: Snapshot of the coupling grid. The input and output parts are marked. In the middle of the panel different passive two-port coupling components can be connected. A programmable logic along with a coupling grid constitutes a single layer of autonomous CNN.

to their nearest neighbors with a coupling weight. Chua's circuits were set to be in double scroll chaotic mode (double scroll is one of the attractors that shows two lobes just like butterfly's wing in phase space. This is the most commonly known state of chaos and is observed in Chua's circuit and Lorentz system). They were coupled to neighbors at terminal A (i.e. non-grounded inductor node). Up to ten Chua's circuits in 1, 2 and 3 dimensions were connected. In each topology the values of the resistors were varied from $10K$ to 0 i.e. from less coupled to more coupled system. These topologies are as shown in the following Fig. 4.8/A.

DOI:10.15774/PPKE.ITK.2012.003

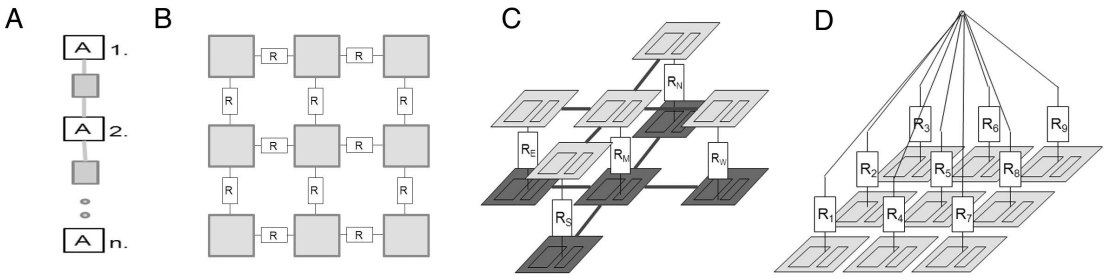

Figure 4.8: The topologies and the weights, which were used in the experiments, can be seen here. 'A' is 1D in line, 'B' is 2D, 'C' is 3D in cross format, 'D' where 9 elements connected to a common point.

4.6.1 Case 1. one dimensional coupled Chua's circuits

In the present case, two Chua's circuits were connected together in the fashion as shown in Fig. 4.8/A. The equations that govern this dynamics are given by:

$$\dot{x_1} = \alpha_1(y_1 - f_1(x_1)) + \frac{k}{R}(x_2 - x_1) \tag{4.16}$$

$$\dot{y_1} = x_1 - y_1 + z_1 \tag{4.17}$$

$$\dot{z_1} = -\beta_1 y_1 \tag{4.18}$$

$$\dot{x_2} = \alpha_2(y_2 - f_2(x_2)) + \frac{k}{R}(x_1 - x_2) \tag{4.19}$$

$$\dot{y_2} = x_2 - y_2 + z_2 \tag{4.20}$$

$$\dot{z_2} = -\beta_2 y_2 \tag{4.21}$$

It was observed that as the value of coupling resistance between Chua's circuits was changed from 10 $K\Omega$ to 0 Ω, the two moved from de-synchronization to synchronization. The two cases are as shown in Fig. 4.9.

An interesting observation was also made wherein it was found that as the system moves from de-synchronization to synchronization, there is a value of coupling coefficient, where the two Chua's circuits are in phase lag with each other. During this time, neither of the chaotic circuits remain chaotic. The oscilloscope tracing of such phenomenon is as shown if Fig. 4.10. By further decreasing the coupling resistors, the system showed chaotic oscillation again and at 0 Ω they got synchronized.

DOI:10.15774/PPKE.ITK.2012.003

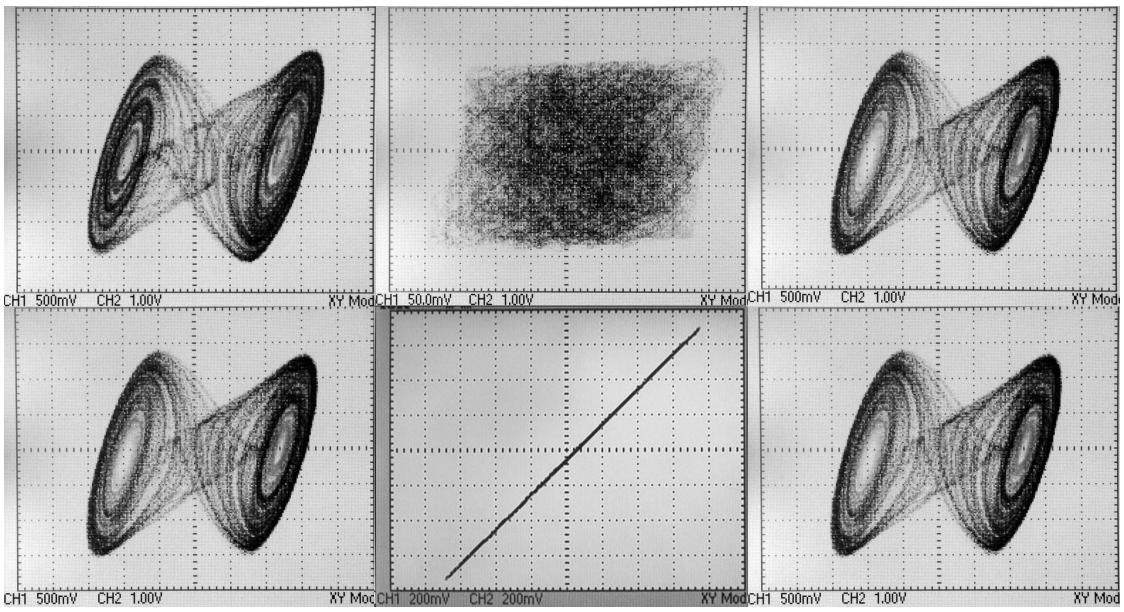

Figure 4.9: On the left and right of the picture two states of Chua's circuit can be observed. Between them, their correlation is shown. On the top at 10 $K\ \Omega$ coupling value the system shows de-synchronized behavior, on the bottom at 0 Ω they are synchronized.

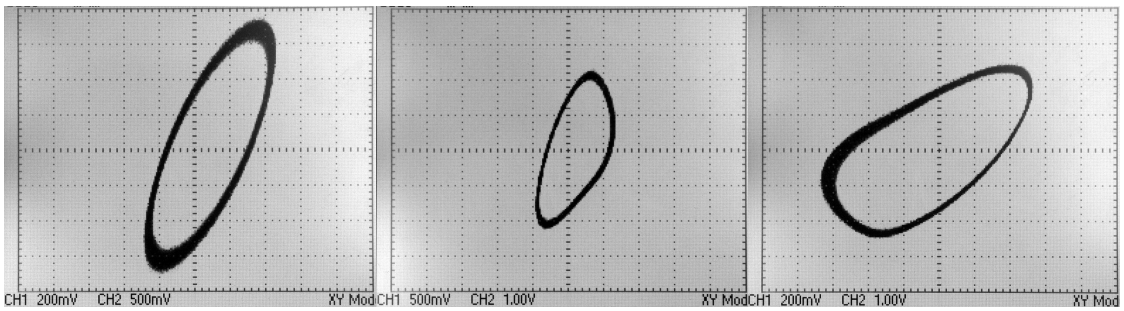

Figure 4.10: The left and right oscilloscopes show the phase portrait of two Chua's circuits, in the middle the coupling behavior can be observed (the correlation between the two circuits connected through terminal A). The system moves from de-synchronization to synchronization. There is a value of coupling coefficient where the two Chua's circuits are in phase lag with each other. During this time neither of the chaotic circuits remains chaotic.

DOI:10.15774/PPKE.ITK.2012.003

These experimenter result were confirmed using SPICE simulation of two connected Chua's circuit. The following figures shows the SPICE simulation results for the observed synchronization phenomenon. Figure 4.11 shows the SPICE simulation results for the condition when two Chua's circuits were connected by 10 $K\Omega$ resistor with other values remaining the same as mentioned earlier.

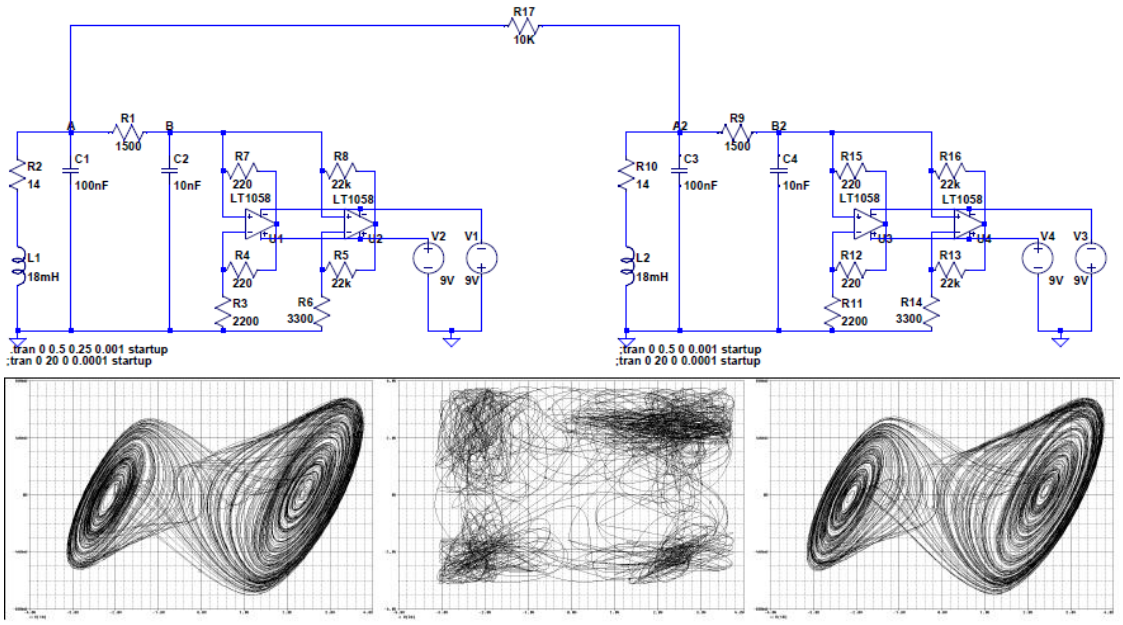

Figure 4.11: This figure shows the SPICE realization and simulation results for the condition when two Chua's circuits were connected by 10 $K\Omega$ resistor.

Fig. 4.12 shows the SPICE simulation results for the condition when two Chua's circuits were connected by 1 $K\Omega$ resistor.

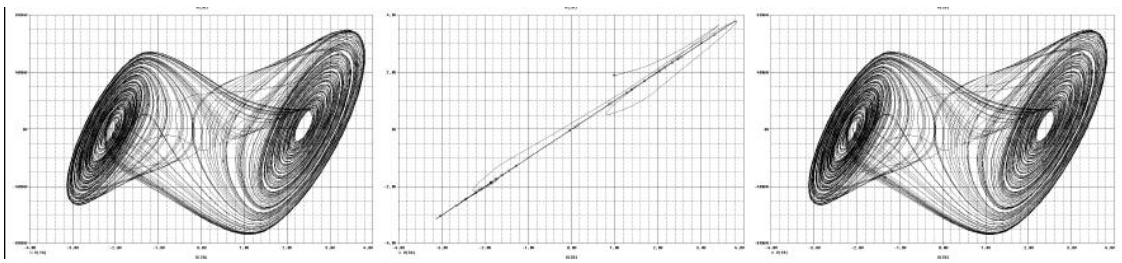

Figure 4.12: This figure shows the SPICE simulation results for the condition when two Chua's circuits were connected by 1 $K\Omega$ resistor.

Fig. 4.13 shows the SPICE simulation results for the condition when two Chua's circuits were connected by 6.5 $K\Omega$ resistor.

DOI:10.15774/PPKE.ITK.2012.003

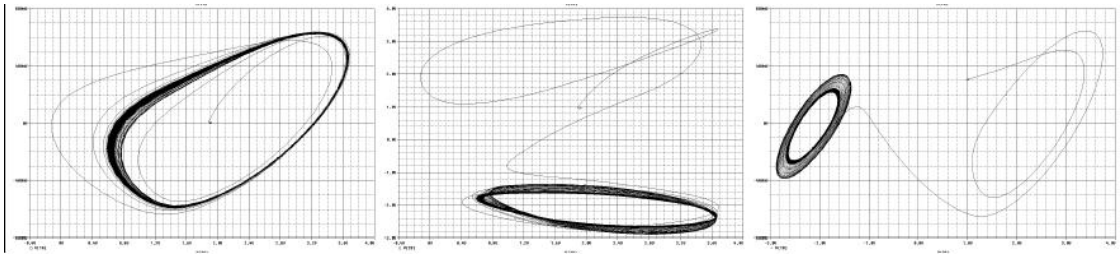

Figure 4.13: This figure shows the SPICE simulation results for the condition when two Chua's circuits were connected by 6.5 $K\Omega$ resistor

At the begining of the simulation both Chua's circuits were in chaotic oscillation and only after 56 ms their output suddenly synchronized with a phase shift, the transient can be seen in Fig. 4.1

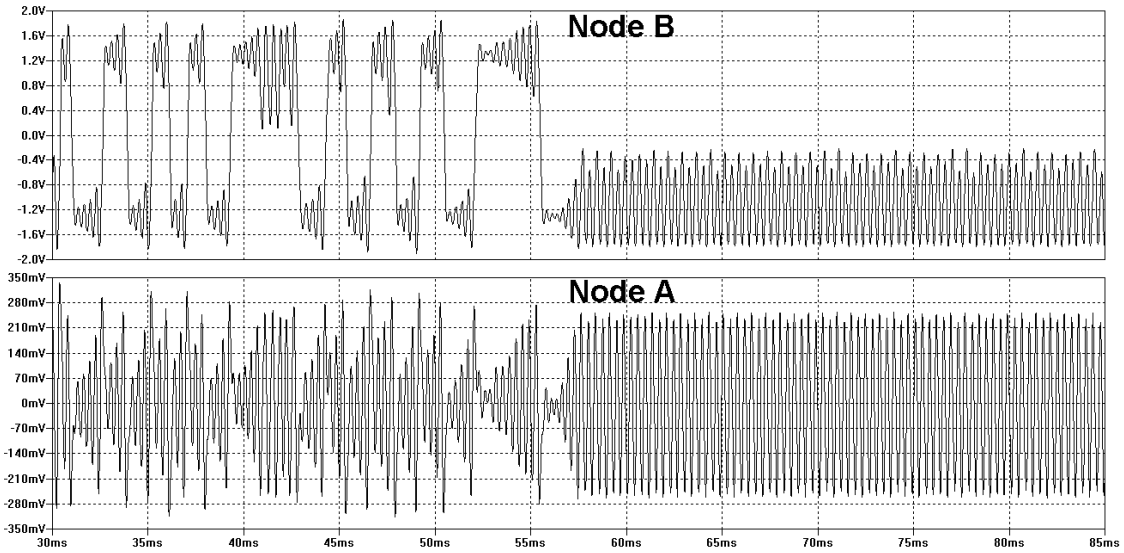

Figure 4.14: Simulation resut of two Chua's circuits where the transient behaviour can be observed. Both circuit were in chaotic oscillation at the begining and they output get syncronised with a phase shift at 56 ms.

Thus it is evident from the figures that the coupling of Chua's circuit undergoes a fast phase transition while moving from complete synchronization to de-synchronization.

4.6.2 Case 2. two dimensional coupled Chua's circuits

The 1D case was extended by coupling more Chua's circuit and similar phenomenon was observed at different coupling resistance. These values for different size of 1D

DOI:10.15774/PPKE.ITK.2012.003

CNN are listed in Table 4.1.

Table 4.1: Copuling ranges where connected Chua's circuits are in phase lag with each other for different topologies.

Connected	Chua's	circuits						
Size 1D	2	3	4	5	6	7	8	9
Resistor ($K\Omega$)	9.2-4.2	5.6-1.3	5.2-3.6	6.1-3.9	5.3-3.5	1.2-0.7	4.7-3	4.7-3.6
Size 2D	2x2	2x3	3x3					
Resistor ($K\Omega$)	7.15-5.2 6.2-4.1	5.6-1.3	8.7-5 5.5-0.280					
Size 3D	3x3							
Resistor ($K\Omega$)	7.2-4.2							

In the 2D case, the used topology can be seen in Fig. 4.8/B. Different numbers of Chua's circuits were connected and the similar phenomenon also appeared here. In some cases there were two different coupling regions where a similar phenomenon appeared. These values for different size of 2D CNN are listed in Table 4.1.

4.6.3 Case 3. three dimensional coupled Chua's circuits

A specific case of 3D coupled chaotic system, coupled by the scheme as shown in Fig. 4.8/C, was performed. All the resistors on one layer were kept at zero in order to keep all Chua's circuits on a specific layer in synchronized state, whereas the interconnecting resistors were varied. The phase portrait between the middle cells of both layers is as shown in Fig. 4.15.

As another experiment, a $3x3$ array of Chua's circuits was built. Each cell was connected to a common point through its own weight. Therefore the system has only 9 coupling weights. The connecting topology can be seen on Fig. 4.8/D.

It was observed that when some of the resistors were varied, a specific set of cells got synchronized while others did not. The results are in line with a similar work published earlier [22]. Whereas the previous studies were primarily software simulations, the present case is a hardware implementation of a similar case.

Note that software simulations did not take into account several non-idealities of the system whereas the test bed is a real-time system. Table 4.2 summarizes

DOI:10.15774/PPKE.ITK.2012.003

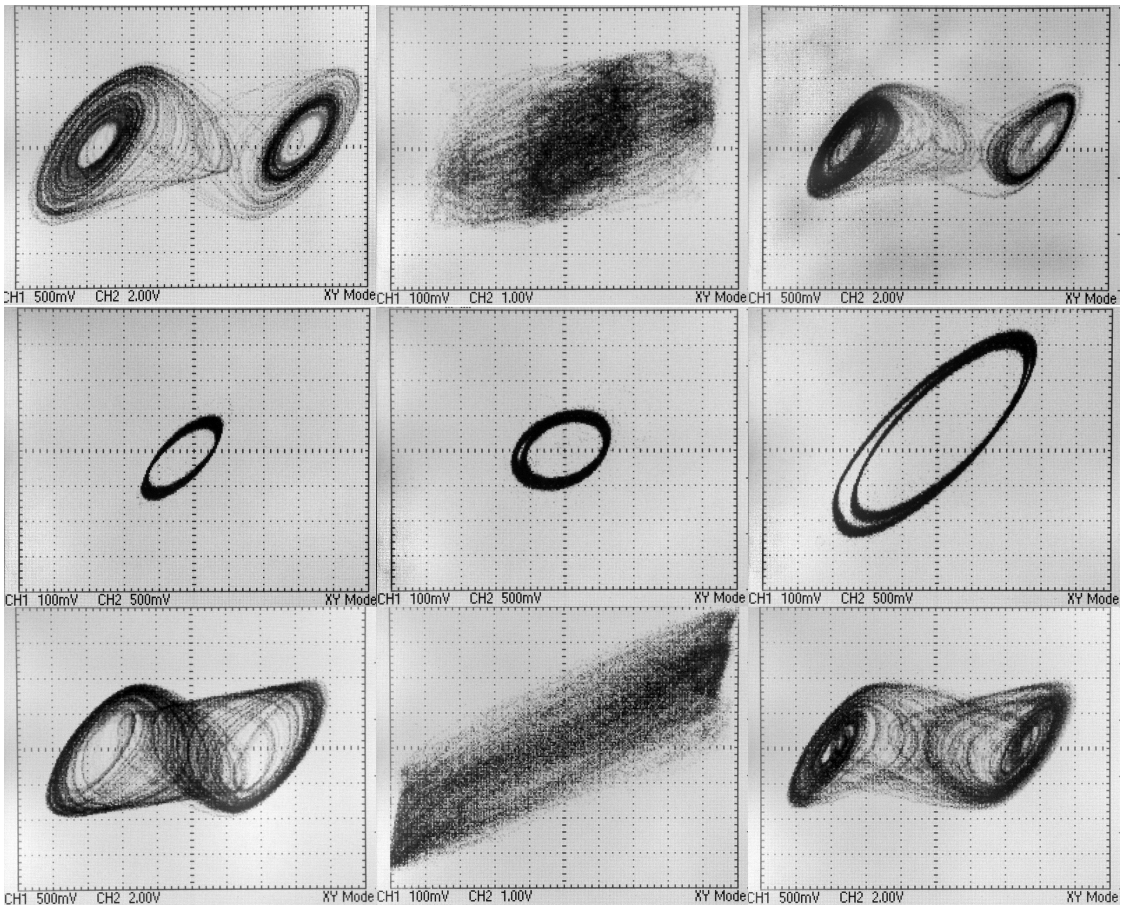

Figure 4.15: Ten Chua's Circuits were connected in 3D in a cross like topology (five-five pieces in each layer, each in double scroll). The coupling weight in the layers were 0Ω. On the left and right pictures, the two middle cells can be seen when the coupling was 10 $K\Omega$ meaning no synchronization. In the middle column of the picture, the correlation can be seen between the layers in each coupling case. Besides, the middle cells showed circles at 7.2 $K\Omega$ (left,right) but this also represents the state of the same layer's other cells because of the 0Ω coupling. On the bottom of the picture, the system shows chaotic behavior again at 4.2 $K\Omega$.

DOI:10.15774/PPKE.ITK.2012.003

Table 4.2: Synchronization pattern weights [22] and the corresponding resistor values for $3x3$ array.

Cell in the 3x3 array	(1,1)	(1,2)	(1,3)	(2,1)	(2,2)	(2,3)	(3,1)	(3,2)	(3,3)
Simulated values	0.31	5.31	0.11	8.77	0.54	25.52	18.35	4.71	6.04
Measured values ($K\Omega$)	0.12	2.08	0.04	3.44	0.21	10	7.19	1.85	2.37
Simulated values	0.34	26.30	20.68	22.05	17.59	12.79	22.35	19.16	0.16
Measured values ($K\Omega$)	0.13	10	7.86	8.38	6.69	4.86	8.5	7.29	0.06
Simulated values	11.24	21.84	12.78	0.09	18.48	0.03	24.48	12.30	17.80
Measured values ($K\Omega$)	4.59	8.92	5.22	0.04	7.55	0.01	10	5.02	7.27

the values of resistances that were taken for performing the present experiment.

The experimental result and the oscillation pattern can be observed in Fig. 4.16. This in turn proves the usability of the present test bed (Fig. 4.17) as it can help us visualize the synchronization schemes in real time environment.

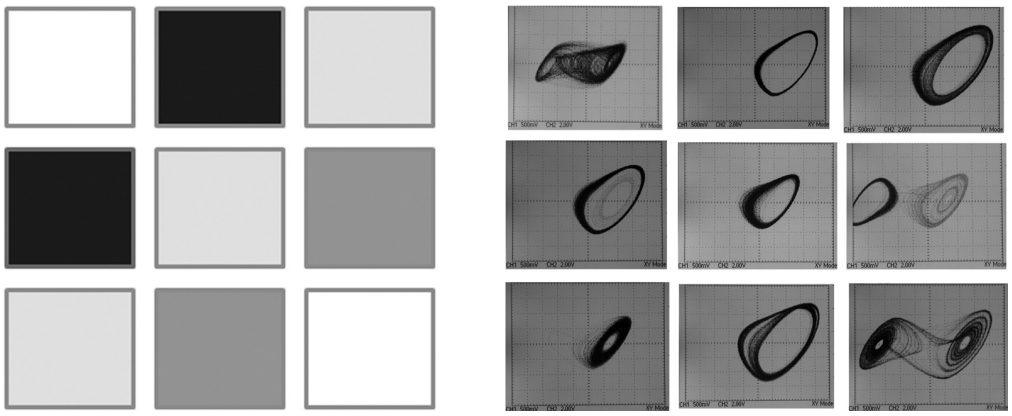

Figure 4.16: Connecting $3x3$ Chua's circuits and using the scaled coupling values of a simulated network [22], the very same oscillation pattern was observed. On the left picture, an oscillation pattern can be seen. Cells synchronized together are marked with the same grayscale level. On the right there are snapshots of each cell's actual state.

DOI:10.15774/PPKE.ITK.2012.003

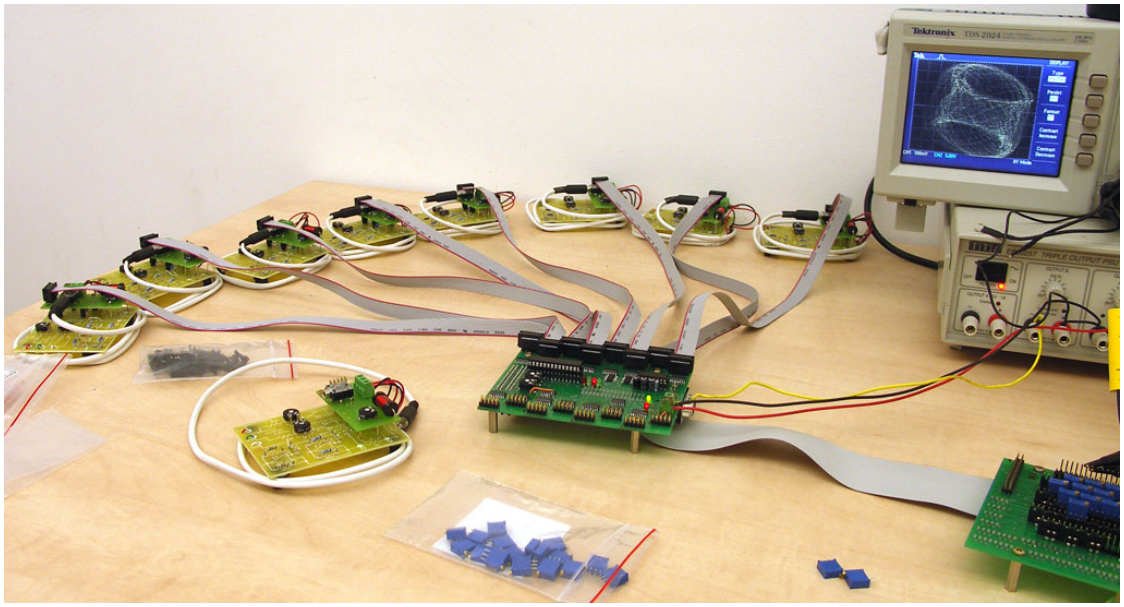

Figure 4.17: A picture of the experimental setup where eight Chua's circuits were connected and on the oscilloscope an interesting correlation form can be seen.

DOI:10.15774/PPKE.ITK.2012.003

4.7 Discussion

Synchronization of oscillatory and chaotic networks have sprung as a completely new field of nonlinear dynamics. Whereas several studies have been done on the same field, it lacked a single platform to test several similar or different autonomous networks connected. The present chapter provides the information about the test bed that was created to address such need. As a test bed, it was also demonstrated to observe different interesting phenomena among several interconnected Chua's chaotic circuits.

Note that the aim of the research was to develop a hardware test bed which can connect different kind of oscillators. It was aimed at studying synchronization phenomena in coupled systems and was in no way aimed at exploring any new results, though some interesting phenomena were observed. These and many similar observations are subject for a separate study.

Other than the fact that hardware implementation provides an easy-to-use topology, it is the inherent design of the Chua's circuit kit that helps to have different parameters for different chaotic cells. This further enhances the flexibility to study cases having cells with different parameters.

DOI:10.15774/PPKE.ITK.2012.003

4.8 Conclusion

The architecture of a test bed to study several interconnected chaotic Chua's circuits is presented. The architecture is based on CNN with four neighbor connectivity. A robust Chua's circuit kit was also designed, which acts as a cell to the CNN architecture. Several topologies of resistively coupled CNN were studied and laboratory results were found to yield several interesting phenomena.

As conclusion the following thesis points can be stated:

Thesis III.:

Design and implementation of an architecture for interconnecting single cell chaotic oscillators with any active or passive two pole components.

A: I have designed a modular hardware architecture for connecting any kind of (even chaotic) oscillator in different kinds of topology (practically limited to 4x4xn) with any active or passive two pole component. I have observed a new phase lag synchronization phenomenon in weakly coupled chaotic oscillators during the transition from de-synchronization to synchronization in case of 1D, 2D and 3D CNN like topology.

Published in: [2], [6]

DOI:10.15774/PPKE.ITK.2012.003

Chapter 5

Summary

5.1 Main findings and results

- I have created a proximity sensor array to create single view 3D back projection images of the objects. It showed promising results in object outline surface trace and landmark detection. Test cases also presented in case of localization and object detection simulating a bipedal robot motion.

- A 3D complaint tactile sensor design is detailed and tested with different force measurements where the sensor showed high force dynamic range from measuring the pulse shape up to a impact of a hammer.

- I have created a hardware test bed to studying several interconnected oscillators where a new phase lag phenomena was observed among several interconnected Chua's chaotic circuits.

5.2 New scientific results

Object outline and surface trace detection using 3D imaging based a low resolution proximity array containing infra LEDs - photodiodes.

- *I have designed and implemented a low resolution infra LED - photodiode based proximity array. Using several photodiodes to detect the reflected light from each infra LED, an iterative method was developed to calculate the angle of incidence in case of flat objects with known α_i parameters, for achieving more precise distance measurement.*

DOI:10.15774/PPKE.ITK.2012.003

- *A new method has been given to decrease the smoothing effect at object edges during the sensor array motion.*
- *I have demonstrated in mobile robot experiments that the sensor array is capable of detecting on road localization landmarks and obstacles before crossing.*

Design of a low cost 3D optical compliant tactile sensor that is capable of measuring three-axial directional force components and the location of the contact point.

- *I have designed a robust layered structured elastic cover, which supports the realization of small sized sensors (<1cm).*
- *I have designed a calibration process to measure the sensor characteristics. I have shown a method to measure the location point position on the sensor surface.*

Design and implementation of an architecture for interconnecting single cell chaotic oscillators with any active or passive two pole components.

- *I have designed a modular hardware architecture for connecting any kind of (even chaotic) oscillator in different kind of topology (practically limited to 4x4xn) with any active or passive two pole component. I have observed a new phase lag synchronization phenomenon in weakly coupled chaotic oscillators during the transition from de-synchronization to synchronization in case of 1D, 2D and 3D CNN like topology.*

5.3 Application of the results

During my work, all the algorithms and hardware realizations I made give a possible solution for real and up to date problems.

The first results of the thesis group will hopefully offer a solution for creating obstacle detection, avoidance and SLAM using low cost sensors. For example, for vacuum cleaner robots where without a global map the successful and optimal work hardly can be guaranteed but using the described sensor array (by extending to 2D) a map can be created based on the floor pattern.

DOI:10.15774/PPKE.ITK.2012.003

In the second thesis group, a new type of sensor is presented that could be used even in the industry due to its high force measurement range, dynamics and robustness. It has already shown promising results in the medical field to measure blood pressure and pulse shape in a non-invasive way. The presented sensor also could be used as high precision tactile sensor in many fields of robotics as it can detect forces from firmly stroke up to a hammer impact.

The results of the third thesis group could be used as an experimental hardware kit, where the results of the software simulation could be validated or new phenomenons could be observed in real time.

DOI:10.15774/PPKE.ITK.2012.003

5. SUMMARY

DOI:10.15774/PPKE.ITK.2012.003

Journal Publications of the Author

Publications

[1] **Á. Tar** and Gy. Cserey, "Object Outline and Surface-Trace Detection Using Infrared Proximity Array," *Sensors Journal, IEEE*, no. 99, pp. 1–1, 2011.

[2] **Á. Tar**, G. Gandhi, and Gy. Cserey, "Hardware implementation of CNN architecture-based test bed for studying synchronization phenomenon in oscillatory and chaotic networks," *International Journal of Circuit Theory and Applications*, vol. 37, no. 4, pp. 529–542, 2009.

Conference Publications of the Author

Publications

[3] **Á. Tar**, J. Veres, and Gy. Cserey, "Design and Realization of a Biped Robot Using Stepper Motor Driven Joints," in *International Conference on Mechatronics (ICM)*, pp. 493–498, IEEE, 2006.

[4] **Á. Tar**, M. Koller, and Gy. Cserey, "3D geometry reconstruction using Large Infrared Proximity Array for robotic applications," in *International Conference on Mechatronics (ICM)*, pp. 1 – 6, IEEE, 2009.

[5] **Á. Tar** and Gy. Cserey, "Development of a Low Cost 3D Optical Compliant Tactile Force Sensor," in *International Conference on Advanced Intelligent Mechatronics (AIM)*, IEEE, 2011.

[6] **Á. Tar**, G. Gandhi, Gy. Cserey, and T. Roska, "3D modular CNN grid using Chua's circuit kits," in *The 10th Experimental Chaos Conference (ECC10)*, pp. 1 – 6, IEEE, 2008.

[7] N. Sárkány, Gy. Cserey, **Á. Tar**, and J. Veres, " Design of a biomechatronic hand actuated by the flexor-extensor mechanism," in *International Conference on Advanced Intelligent Mechatronics (AIM)*, IEEE, 2011.

DOI:10.15774/PPKE.ITK.2012.003

DOI:10.15774/PPKE.ITK.2012.003

Bibliography

[8] K. Hirai, M. Hirose, Y. Haikawa, and T. Takenaka, "The development of honda humanoid robot," in *International Conference on Robotics and Automation*, vol. 2, pp. 1321–1326, IEEE, 1998. 1, 2

[9] F. Plestan, J. Grizzle, E. Westervelt, and G. Abba, "Stable walking of a 7-dof biped robot," *Transactions on Robotics and Automation*, vol. 19, no. 4, pp. 653–668, 2003. 1

[10] M. Morisawa, K. Harada, S. Kajita, S. Nakaoka, K. Fujiwara, F. Kanehiro, K. Kaneko, and H. Hirukawa, "Experimentation of humanoid walking allowing immediate modification of foot place based on analytical solution," in *International Conference on Robotics and Automation*, pp. 3989–3994, IEEE, 2007. 1

[11] J. Yamaguchi, E. Soga, S. Inoue, and A. Takanishi, "Development of a bipedal humanoid robot-control method of whole body cooperative dynamic biped walking," in *International Conference on Robotics and Automation*, vol. 1, pp. 368–374, IEEE, 1999. 1

[12] S. Collins and A. Ruina, "A bipedal walking robot with efficient and human-like gait," in *International Conference on Robotics and Automation (ICRA)*, pp. 1983–1988, IEEE, 2005. 1

[13] J. Pratt and G. Pratt, "Exploiting natural dynamics in the control of a planar bipedal walking robot," in *Annual Allerton Conference on Communications, Control and Computing*, vol. 36, pp. 739–748, Citeseer, 1998. 1

[14] M. Lee, "Tactile sensing: new directions, new challenges," *The International Journal of Robotics Research*, vol. 19, no. 7, p. 636, 2000. 2, 29

DOI:10.15774/PPKE.ITK.2012.003

[15] J. Seara, K. Strobl, and G. Schmidt, "Path-dependent gaze control for obstacle avoidance in vision guided humanoid walking," in *International Conference on Robotics and Automation (ICRA)*, vol. 1, pp. 887–892, IEEE, 2003. 2

[16] P. Michel, J. Chestnutt, J. Kuffner, and T. Kanade, "Vision-guided humanoid footstep planning for dynamic environments," in *The 5th International Conference on Humanoid Robots (RAS)*, pp. 13–18, IEEE, 2005. 2

[17] Y. Guan, E. Neo, K. Yokoi, and K. Tanie, "Stepping over obstacles with humanoid robots," *Transactions on Robotics*, vol. 22, no. 5, pp. 958–973, 2006. 2

[18] Q. Huang and Y. Nakamura, "Sensory reflex control for humanoid walking," *Transactions on Robotics*, vol. 21, no. 5, pp. 977–984, 2005. 2

[19] M. Barahona and L. M. Pecora, "Synchronization in small-world systems," *Phys. Rev. Lett.*, vol. 89, p. 054101, Jul 2002. 2, 55

[20] L. Chen and K. Aihara, "Strange attractors in chaotic neural networks," *Transactions on Circuits and Systems I: Fundamental Theory and Applications*, vol. 47, no. 10, pp. 1455–1468, 2000. 2, 55

[21] E. Bilotta, P. Pantano, and F. Stranges, "A gallery of chua attractors: Part II," *International Journal of Bifurcation and Chaos*, vol. 17, no. 2, pp. 293–380, 2007. 2, 55

[22] D. Hillier, S. Gunel, J. Suykens, and J. Vandewalle, "Partial synchronization in oscillator arrays with asymmetric coupling," *International Journal of Bifurcation and chaos*, vol. 17, no. 11, pp. 4177–4185, 2007. 2, 69, 71

[23] W. Pritchard and D. Duke, "Measuring chaos in the brain-a tutorial review of eeg dimension estimation," *Brain and Cognition*, vol. 27, no. 3, pp. 353–397, 1995. 2

[24] H. Korn and P. Faure, "Is there chaos in the brain? ii. experimental evidence and related models," *Comptes rendus biologies*, vol. 326, no. 9, pp. 787–840, 2003. 2

[25] S. Schiff, K. Jerger, D. Duong, T. Chang, M. Spano, and W. Ditto, "Controlling chaos in the brain," *Nature*, vol. 370, no. 6491, pp. 615–620, 1994. 2

DOI:10.15774/PPKE.ITK.2012.003

[26] J. Skinner, A. Goldberger, G. Mayer-Kress, and R. Ideker, "Chaos in the heart: implications for clinical cardiology," *Nature Biotechnology*, vol. 8, no. 11, pp. 1018–1024, 1990. 3

[27] O. Faugeras and G. Toscani, "Camera calibration for 3d computer vision," in *International Workshop on Machine Vision and Machine Intelligence*, pp. 240–247, 1987. 5

[28] W. Niem and J. Wingbermuhle, "Automatic reconstruction of 3d objects using a mobile monoscopic camera," in *3-D Digital Imaging and Modeling, 1997. Proceedings., International Conference on Recent Advances in*, pp. 173–180, IEEE, 1999. 5

[29] H. Surmann, K. Lingemann, A. N
"uchter, and J. Hertzberg, "A 3d laser range finder for autonomous mobile robots," in *Proceedings of the 32nd ISR (International Symposium on Robotics)*, vol. 19, pp. 153–158, Citeseer, 2001. 5

[30] Y. Omura, A. Goto, and N. Shidara, "Surface-Trace Feasibility for IR-Based Position-Sensing Devices," *IEEE Sensors Journal*, vol. 9, no. 10, 2009. 5, 6

[31] M. Baba, K. Ohtani, and S. Komatsu, "3D shape recognition system by ultrasonic sensor array and genetic algorithms," in *The 21st Instrumentation and Measurement Technology Conference (IMTC)*, vol. 3, IEEE, 2004. 5

[32] H. Park, S. Lee, and W. Chung, "Obstacle Detection and Feature Extraction using 2.5 D Range Sensor System," in *International Joint Conference of SICE-ICASE,*, pp. 2000–2004, 2006. 6

[33] H. Park, S. Baek, and S. Lee, "IR sensor array for a mobile robot," in *International Conference on Advanced Intelligent Mechatronics (ASME)*, pp. 928–933, IEEE, 2005. 6

[34] S. Lee and W. Chung, "Rotating IR Sensor System for 2.5 D Sensing," in *International Conference on Intelligent Robots and Systems (RSJ)*, pp. 814–819, IEEE, 2006. 6

[35] P. Vaz, R. Ferreira, V. Grossmann, M. Ribeiro, I. Norte, and A. Pais, "Docking of a mobile platform based on infrared sensors," in *International Symposium on Industrial Electronics, Guimaraes, Portugal*, IEEE, 1997. 6

DOI:10.15774/PPKE.ITK.2012.003

[36] G. Benet, F. Blanes, J. Simo, and P. Perez, "Using infrared sensors for distance measurement in mobile robots," *Robotics and autonomous systems*, vol. 40, no. 4, pp. 255–266, 2002. 7, 14

[37] Y. Shan, J. Speich, and K. Leang, "Low-Cost IR Reflective Sensors for Submicrolevel Position Measurement and Control," *Transaction on Mechatronics (ASME)*, vol. 13, no. 6, 2008. 7

[38] P. Novotny and N. Ferrier, "Using infrared sensors and the Phong illumination model to measure distances," in *International Conference on Robotics and Automation*, pp. 1644–1649, IEEE, 1999. 7

[39] C. Yuzbasioglu and B. Barshan, "Improved range estimation using simple infrared sensors," *Measurement Science and Technology*, vol. 16, pp. 1395–1409, 2005. 7

[40] Yuzbasioglu, C. and Barshan, B., "A new method for range estimation using simple infrared sensors," in *International Conference on Intelligent Robots and Systems,(IROS)*, pp. 1066–1071, IEEE, 2005. 7

[41] T. Aytaç and B. Barshan, "Differentiation and localization of target primitives using infrared sensors," in *International Conference on Intelligent Robots and Systems (RSJ)*, pp. 105–110, IEEE, 2002. 7

[42] F. Gines Benet, J. Sinto, and P. Perez, "Map building using infrared sensors in mobile robots," *New Developments in Robotics Research*, p. 73, 2005. 7

[43] D. Navarro, G. Benet, and F. Blanes, "Line-based incremental map building using infrared sensor ring," in *International Conference on Emerging Technologies and Factory Automation (ETFA)*, pp. 833–838, IEEE, 2008. 7

[44] M. Garcia and A. Solanas, "Estimation of distance to planar surfaces and type of material with infrared sensors," in *The 17th International Conference on Pattern Recognition*, vol. 1, pp. 745–748, 2004. 7

[45] S. Railhet, J. Wolf, A. Adra, R. Kabbara, S. Deshmukh, M. Garghouti, G. Nash, T. Belpaeme, P. Culverhouse, P. Robinson, *et al.*, "Sensor systems in a compliant geometry robot: ButlerBot.," 2008. 7

DOI:10.15774/PPKE.ITK.2012.003

[46] L. Marques, D. Castro, U. Nunes, and A. De Almeida, "Optoelectronic proximity sensor for robotics applications," in *Melecon Mediterranean Electrotechnical Conference*, pp. 1351–1354, 1996. 7

[47] V. Pavlov, H. Ruser, and M. Horn, "Feature extraction from an infrared sensor array for localization and surface recognition of moving cylindrical objects," in *Instrumentation and Measurement Technology Conference Proceedings (IMTC)*, pp. 1–6, IEEE, 2007. 7

[48] "http://www.mobilerobots.com," 11

[49] A. Flynn, "Combining sonar and infrared sensors for mobile robot navigation," *The International Journal of Robotics Research*, vol. 7, no. 6, p. 5, 1988. 14

[50] R. Russell, *Robot tactile sensing*. Prentice-Hall, Inc. Upper Saddle River, NJ, USA, 1990. 29

[51] T. Inoue and S. Hirai, "Modeling of soft fingertip for object manipulation using tactile sensing," in *International Conference on Intelligent Robots and Systems (IROS)*, vol. 3, pp. 2654–2659, IEEE, 2003. 29

[52] B. Choi, H. Choi, and S. Kang, "Development of tactile sensor for detecting contact force and slip," in *International Conference on Intelligent Robots and Systems (IROS)*, pp. 2638–2643, IEEE, 2005. 30

[53] G. Hellard and R. Russell, "A robust, sensitive and economical tactile sensor for a robotic manipulator," in *Australasian Conference on Robotics and Automation, Auckland*, pp. 100–104, Citeseer, 2002. 30

[54] K. Yamada, Y. Nakajima, N. Koshida, K. Goto, and H. Shinoda, "Wire-free tactile sensing element based on optical connection," in *Technical Digest of the Sensor Symposium*, vol. 19, pp. 433–436, 2002. 30

[55] P. Lang, "Design and prototyping of a fiber optic tactile array," in *Canadian Conference on Electrical and Computer Engineering (CCECE)*, pp. 000373–000376, IEEE, 2008. 30

[56] K. Kamiyama, H. Kajimoto, N. Kawakami, and S. Tachi, "Evaluation of a vision-based tactile sensor," in *International Conference on Robotics and Automation*, vol. 2, pp. 1542–1547, IEEE, 2004. 30

DOI:10.15774/PPKE.ITK.2012.003

[57] M. Carrozza, S. Micera, B. Massa, M. Zecca, R. Lazzarini, N. Canelli, and P. Dario, "The development of a novel biomechatronic hand-ongoing research and preliminary results," in *International Conference on Advanced Intelligent Mechatronics (ASME)*, vol. 1, pp. 249–254, IEEE, 2002. 30

[58] J. Butterfass, M. Grebenstein, H. Liu, and G. Hirzinger, "DLR-Hand II: Next generation of a dextrous robot hand," in *International Conference on Robotics and Automation (ICRA)*, vol. 1, pp. 109–114, IEEE, 2001. 30

[59] J. Salisbury Jr, "Interpretation of contact geometries from force measurements," in *International Conference on Robotics and Automation*, vol. 1, pp. 240–247, IEEE, 1984. 30

[60] G. Vasarhelyi, M. Adam, E. Vazsonyi, Z. Vizvary, A. Kis, I. Barsony, and C. Ducso, "Characterization of an integrable single-crystalline 3-d tactile sensor," *Sensors Journal*, vol. 6, no. 4, pp. 928–934, 2006. 30

[61] A. Kis, F. Kovács, and P. Szolgay, "3D tactile sensor array processed by CNN-UM: a fast method for detecting and identifying slippage and twisting motion," *International Journal of Circuit Theory and Applications*, vol. 34, no. 4, pp. 517–531, 2006. 30

[62] T. L. Carroll and L. M. Pecora, "Synchronizing chaotic circuits," *Transactions on Circuits and Systems*, vol. 38, no. 4, pp. 453–456, 1991. 55

[63] G. D. VanWiggeren and R. Rajarshi, "Communication with chaotic lasers," *Science*, vol. 279, no. 5354, pp. 1198–1200, 1998. 55

[64] H. F. Chen and J. M. Liu, "Open-loop chaotic synchronization of injection-locked semiconductorlasers with gigahertz range modulation," *Journal of Quantum Electronics*, vol. 36, no. 1, pp. 27–34, 2000. 55

[65] Z. Duan, J. Wang, and L. Huang, "Multi-input and multi-output nonlinear systems: Interconnected chua's circuits," *International Journal of Bifurcation and Chaos*, vol. 14, no. 9, pp. 3065–3082, 2004. 55

[66] M. J. Ogorzalek, A. Dabrowski, and W. Dabrowski, "Hyperchaos, clustering and cooperative phenomena in CNN arrayscomposed of chaotic circuits," in *Cellular Neural Networks and their Applications, 1994. CNNA-94., Proceedings of the Third IEEE International Workshop on*, (Rome, Italy), pp. 315–320, 1994. 55

DOI:10.15774/PPKE.ITK.2012.003

[67] J. Y. Chen, K. W. Wong, H. Y. Zheng, and J. W. Shuai, "Intermittent phase synchronization of coupled spatiotemporal chaotic systems," *Phys. Rev. E*, vol. 64, p. 016212, Jun 2001. 56

[68] H. Huijberts, H. Nijmeijer, and R. Willems, "System identification in communication with chaotic systems," *Transactions on Circuits and Systems I: Fundamental Theory and Applications*, vol. 47, pp. 800–808, June 2000. 56

[69] M. J. Ogorzalek, Z. Galias, A. M. Dabrowski, and W. R. Dabrowski, "Chaotic waves and spatio-temporal patterns in large arrays ofdoubly-coupled chua's circuits," *Transactions on Circuits and Systems I: Fundamental Theory and Applications*, vol. 42, no. 10, pp. 706–714, 1995. 56

[70] D. Hillier, S. Günel, J. A. K. Suykens, and J. Vandewalle, "Partial synchronization in oscillator arrays with asymmetric coupling," *International Journal of Bifurcation and Chaos*, 2007. 56

[71] L. O. Chua and T. Roska, *Cellular neural networks and visual computing, Foundations and applications*. Cambridge University Press, 2002. 56

[72] L. O. Chua and L. Yang, "Cellular Neural Networks: Theory and applications," *Transactions on Circuits and Systems*, vol. 35, pp. 1257–1290, 1988. 56

[73] L. O. Chua and T. Roska, "The CNN paradigm," *Transactions on Circuits and Systems*, vol. 40, pp. 147–156, 1993. 56

[74] G. Gandhi, Gy. Cserey, J. Zbrozek, and T. Roska, "Anyone can build Chua's circuit: Hands-on-experience with chaos theory for high school students," *International Journal of Bifurcation and Chaos*, 2008. 56, 59, 60

[75] L. Chua, M. Komuro, and T. Matsumoto, "The double scroll family," *Circuits and Systems, IEEE Transactions on*, vol. 33, no. 11, pp. 1072–1118, 1986. 56

[76] K. Murali, M. Lakshmanan, and L. Chua, "The simplest dissipative nonautonomous chaotic circuit," *Transactions on Circuits and Systems I: Fundamental Theory and Applications*, vol. 41, no. 6, pp. 462–463, 1994. 56

[77] S. Wolfram, *A new kind of science*. Champaign, Ilinois, US, United States: Wolfram Media Inc., 2002. 58

DOI:10.15774/PPKE.ITK.2012.003

[78] T. Matsumoto, "A chaotic attractor from chua's circuit," *Transactions on Circuits and Systems*, vol. 31, no. 12, pp. 1055–1058, 2000. 58

[79] M. P. Kennedy, "Robust OP amp realization of chua's circuit," *Frequenz*, vol. 46, pp. 66–80, 1992. 58

[80] P. Arena, S. Baglio, L. Fortuna, and G. Manganaro, "Chua's circuit can be generated by cnn cells," *Transaction on Circuits and Systems - Part I*, pp. 123–125, 1995. 58